CHAVEZ

Direct Absorption Receiver

Final Technical Report

Mark S. Bohn
Meir Carasso

SΞRI

Direct Absorption Receiver

Final Technical Report

Mark S. Bohn
Meir Carasso

December 1989

NOTICE

PREFACE

The research and development described in this document was conducted within the U.S. Department of Energy's (DOE) Solar Thermal Technology Program. The goal of this program is to advance the engineering and scientific understanding of solar thermal technology and to establish the technology base from which private industry can develop solar thermal power production options for introduction into the competitive energy market.

Solar thermal technology concentrates the solar flux, using tracking mirrors or lenses, onto a receiver where the solar energy is absorbed as heat and converted into electricity or incorporated into products as process heat. The two primary solar thermal technologies, central receivers and distributed receivers, employ various point and line-focus optics to concentrate sunlight. Current central receiver systems use fields of heliostats (two-axis tracking mirrors) to focus the sun's radiant energy onto a single, tower-mounted receiver. Point-focus concentrators up to 17 meters in diameter track the sun in two axes and use parabolic dish mirrors or Fresnel lenses to focus radiant energy onto a receiver. Troughs and bowls are line-focus tracking reflectors that concentrate sunlight onto receiver tubes along their focal lines. Concentrating collector modules can be used alone or in a multimodule system. The concentrated radiant energy absorbed by the solar thermal receiver is transported to the conversion process by a circulating working fluid. Receiver temperatures range from 100°C in low-temperature troughs to over 1500°C in dish and central receiver systems.

The Solar Thermal Technology Program is directing efforts to advance and improve each system concept through solar thermal materials, components, and subsystems research and development and by testing and evaluation. These efforts are carried out with the technical direction of DOE and its network of field laboratories that works with private industry. Together they have established a comprehensive, goal-directed program to improve performance and provide technically proven options for eventual incorporation into the Nation's energy supply.

To successfully contribute to an adequate energy supply at reasonable cost, solar thermal energy must be economically competitive with a variety of other energy sources. The Solar Thermal Technology Program has developed components and system-level performance targets as quantitative program goals. These targets are used in planning research and development activities, measuring progress, assessing alternative technology options, and developing optimal components. These targets will be pursued vigorously to ensure a successful program.
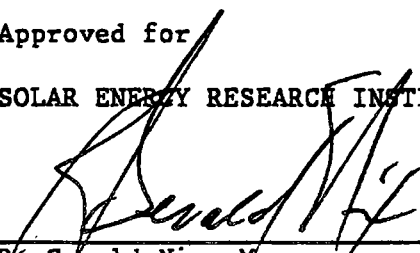
This report describes research during calendar year 1988 at SERI. During this period, the research focused on three technical issues critical to the successful application of the DAR concept: the stability of the long, liquid film, especially the ejection of

liquid droplets; the convective and radiative heat-transfer mechanisms within the film and between the film and the support surface; and the stability of the liquid film with respect to thermocapillary breakdown in the presence of high flux and temperature gradients.

Approved for

SOLAR ENERGY RESEARCH INSTITUTE

R. Gerald Nix, Manager
Thermal Systems Research Branch

B. P. Gupta, Leader
Solar Thermal Program

L. M. Murphy, Director
Solar Heat Research Division

SUMMARY

Objective

To investigate technical issues that could affect commercialization of the molten-salt direct absorption receiver (DAR) concept. In particular, our goal was to study the behavior of a salt film regarding the growth of roll waves and the ejection of droplets from these waves; to determine if the falling salt film will break down in the presence of high solar flux; to determine the optical and thermal efficiency of the falling film; and to determine whether the receiver support surface will survive.

Discussion

We developed experimental techniques that allowed us to accurately measure the characteristics of water and molten salt films at high Reynolds numbers and for flow lengths long enough to cause waves to develop. These characteristics include wave velocity, mean film thickness, substrate thickness, substrate exposure time, wave peak height, and wave frequency. We measured the rate of droplet ejection from a long salt film and identified mechanisms most likely responsible for droplet ejection. We also investigated the thermocapillary breakdown of vertical falling films of water and glycerol/water mixtures and compared the measurements of breakdown flux with a dimensionless scaling law. This law allowed us to compare the measured breakdown flux of different fluids and to extrapolate the behavior of a molten salt film. The convective heat transfer at the interface between a falling salt film and its support surface was measured to determine the validity of existing heat-transfer correlations. We also developed a detailed mathematical model of the heat-transfer mechanisms in a doped salt film exposed to concentrated solar flux.

Conclusions and Recommendations

We found that as the Reynolds number of a falling liquid film increases, the substrate thickness increases substantially and the exposure time of the substrate to the high flux decreases substantially. These two trends reduce the likelihood of thermocapillary breakdown. Measurements of the instantaneous film thickness in water and in molten-salt films showed that the behavior of the two liquids is quite similar, allowing significantly simpler experiments on water films as an analogy to molten-salt films.

Our data suggest that very small droplets originate from the bursting of turbulent eddies on the liquid surface, and ejection of larger droplets begins where the wave growth starts. Also, the rate of ejection increases exponentially along the flow length. We found that the droplet ejection, especially in the wavy regime, was extremely sensitive to perturbations in the support surface, indicating the need to maintain a very flat support surface.

Our convective heat-transfer tests showed that nitrate salt (both doped and undoped) operates in the turbulent regime and produces very high convective heat-transfer coefficients consistent with existing heat-transfer correlations. Calculations showed that adding a dopant to protect the support surface may not be needed to keep the support surface from overheating; however, the dopant will increase the receiver efficiency about 4% by reducing reflective losses. Thus, the tradeoff between added system complexity due to the

dopant and this increase in efficiency can be considered without regard to support surface protection.

Further research is needed in several areas before the DAR can be recommended for commercialization. The droplet ejection problem is a serious issue that must be addressed. Continued testing of long molten-salt films is needed to determine the efficiency of several methods for droplet containment. Full-scale, full-flow testing of salt inlet distributors is needed. Films without a dopant need to be tested on a large scale with high solar flux to confirm that a dopant is not needed to protect the support surface. System studies are needed to quantify the tradeoff between the expected ~4% gain in receiver efficiency resulting from using a dopant and the increased system complexity. Measurements of breakdown flux in molten salt films at high Reynolds numbers are needed. Fundamental studies are needed to improve our ability to predict the behavior of wavy liquid films at high Reynolds numbers, especially with regard to wave growth, droplet ejection, and convective heat transfer.

TABLE OF CONTENTS

TABLE OF CONTENTS (Concluded)

LIST OF FIGURES

LIST OF FIGURES (Concluded)

LIST OF TABLES

NOMENCLATURE

a_n	coefficients in the expansion of phase function
C	functions defined in Eq. F-6
C_p	specific heat at constant pressure (Ws/kg °C)
c, c_s	salt specific heat (Ws/kg °C)
D	diameter of the particles (m)
f	incident intensity distribution (W/m^2 sr)
g	acceleration of gravity (m/s^2)
g	incident integrated-intensity distribution (W/m^2 r)
h	film thickness (m)
h	salt/support surface heat-transfer coefficient (W/m^2 °C)
I	intensity (W/m^2 sr)
J	integrated intensity (W/m^2 r)
k	index of absorption
k	thermal conductivity (W/m °C)
L	distance from the weir (m)
L	length of the one-dimensional medium (m)
L	total length of irradiated film (m)
m	complex refractive index, n + ik (Appendix E only)
$\hat{m}$	salt flow rate (kg/s)
$\hat{m}_s$	salt flow rate (kg/s)
M	half of the order of quadrature
N	complex refractive index
N	degree of scattering anisotropy
n	index of refraction
p	film thickness probability density function
P_n	Legendre function
Pr	Prandtl number
Q	radiative efficiency
Q	volumetric flow rate (m^3/s)
q	heat flux (W/m^2)
q"(x)	local absorbed solar flux (W/m^2)
q_i"(x)	local incident solar flux (W/m^2)
Re	film Reynolds number, $4\Gamma/\mu$
T	temperature (°C)

NOMENCLATURE (Continued)

ΔT	salt/support surface temperature difference (°C)
T_i	salt inlet temperature (°C)
T_o	salt outlet temperature (°C)
$T_p(x)$	support surface temperature (°C)
$T_s(x)$	local bulk salt temperature (°C)
U_o	mean downward film velocity (m/s)
u	velocity in x-direction (m/s)
V_m	mean lateral film velocity (m/s)
W	flow width (m)
w	weights for numerical quadrature
x	distance in film flow direction from top of active zone (m)

Greek

α	bulk absorptivity of metal
α	size parameter, $\pi D/\lambda$
$\bar{\delta}$	mean film thickness (m)
ε	emissivity
γ	gradient of surface tension with temperature (N/m K)
ζ	integrated scattering phase function
θ	polar angle
λ	wavelength of incident radiation
μ	coefficient of viscosity
μ	direction cosine with respect to y-direction, $\cos\theta$
ρ	density (kg/m^3)
ρ	reflectivity
σ	radiative coefficients, $\sigma_e = \sigma_a + \sigma_s$ (m^{-1})
σ	surface tension (N/m)
δ	azimuthal angle
Φ	scattering phase function
Γ	mass flow per unit width = $\hat{m}/W$ (kg/ms)
μ	absolute viscosity (kg/ms)
ν	salt kinematic viscosity (m^2/s)

NOMENCLATURE (Concluded)

Subscripts

a	absorption
B	breakdown
b	blackbody
e	extinction
in	inlet
L	length of medium
r	radiative
s	substrate
w	wall
∞	ambient
λ	spectral

Superscripts

d	diffuse
s	specular
−	mean
~	dimensionless

1.0 INTRODUCTION

The direct absorption receiver (DAR) is a solar thermal central receiver design that directly exposes a flow of the working fluid to concentrated solar flux. Recent research indicates that using molten salts as the working fluid is technically feasible and economically beneficial (Bohn 1987; Anderson et al. 1987). The molten salt flows down a near-vertical support surface, Figure 1-1, and is exposed to the direct solar flux concentrated by a field of heliostats.

Direct absorption has several potential advantages over a conventional system where the working fluid flows through tubes. First, there is no temperature drop like that associated with an intervening tube wall, and the working fluid itself is at the highest temperature in the system. Second, the DAR is simpler and operates at ambient pressure and, therefore, should be less expensive and more reliable than current tubular receivers. Finally, the DAR can tolerate higher flux levels because the flux does not need to be transferred across a tube wall. This allows the receiver to be smaller for the same thermal capacity, which further decreases the cost and reduces reradiation losses.

As presently envisioned, an optimized commercial DAR delivering 200 MW_{th} would be configured as a right circular cylinder approximately 13 m in height and 8 m in diameter (Anderson et al. 1987). The heliostat aiming strategy would produce a peak flux of about 1400 kW/m^2 near the midheight of the flow path with an average flux of 730 kW/m^2. For a salt inlet temperature of 270°C and
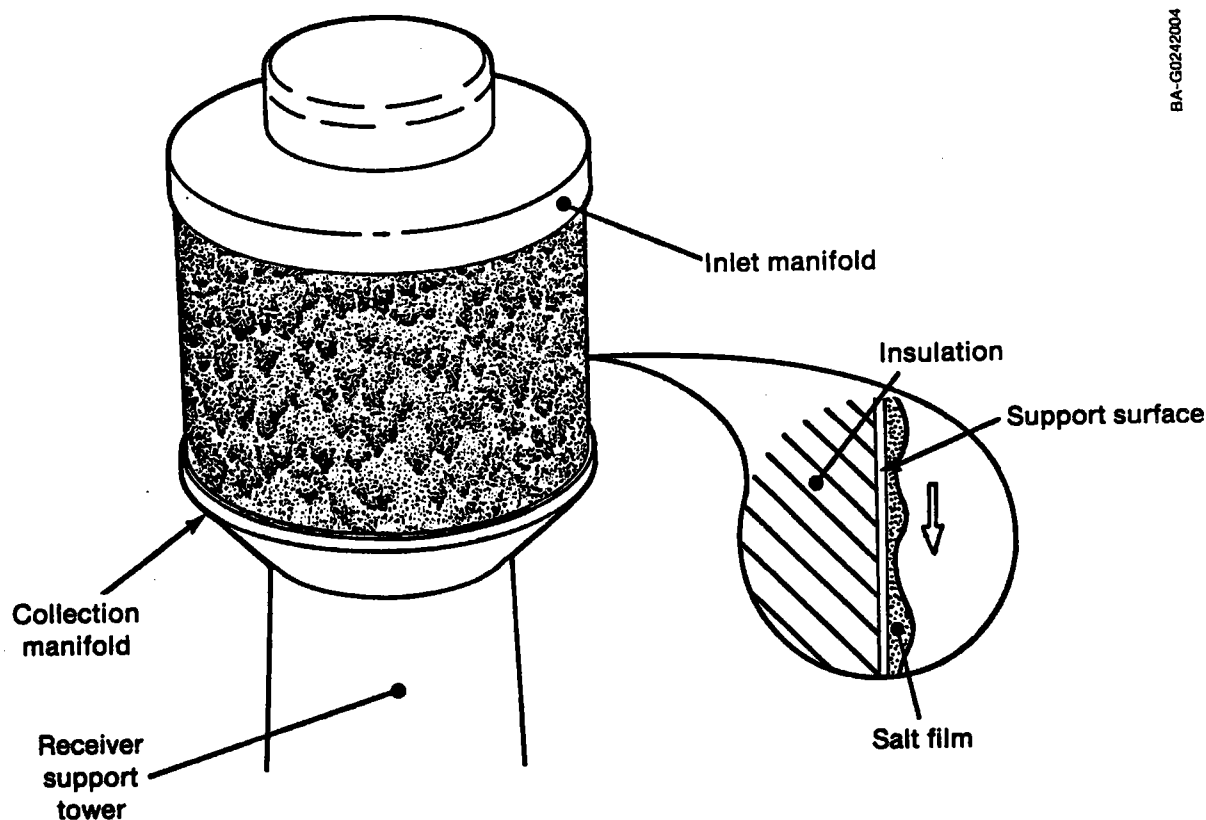
Figure 1-1. Direct absorption receiver

a salt outlet temperature of 570°C, the film Reynolds number (the key parameter that controls film behavior) increases from 23,000 at the inlet to 78,000 at the outlet.

The working fluid currently being considered is a 60/40 wt % mixture of sodium nitrate and potassium nitrate that has a working temperature range of about 250° to 600°C. Above this range the salt decomposes and can become quite corrosive to containment materials. Because this salt is virtually transparent, research is under way to evaluate the addition of cobalt oxide particles to enhance absorption of the solar flux.

The DAR concept was first discussed by Brumleve (1974). He notes the potential advantages of direct absorption, develops preliminary cost estimates for a system using a DAR, and discusses some of the research needs. Brumleve (1978) presented data that showed that salt doped with 0.1 wt % cobalt oxide could tolerate very high flux. He found that for a 2-mm film exposed to 6 MW/m^2 flux, the support surface temperature exceeded the salt temperature by less than 3°C. Drotning (1976) focused on the optical and thermal performance of dopants.

Wang and Copeland (1984) and Webb and Viskanta (1985) developed a model for the heat transfer to study the mechanisms in a falling liquid film exposed to incident flux. Abrams (1975,1976) developed a theoretical model of the solar absorptance and temperature distribution of a flowing salt film. The issue of salt film stability was treated by Newell, Wang, and Copeland (1986) in which they discussed stability at very low flow rates, stability at high flow rates, dryout due to high flux, and interaction with air flow.

We tested the DAR design with solar flux on a 152-mm wide by 610-mm long support surface with carbonate salts (Bohn et al. 1986; Bohn 1987). Data on the convective heat transfer, thermal efficiency, and film breakdown were presented.

Although a considerable amount of work was done on various technical issues related to the DAR, several issues have yet to be considered in sufficient detail such that the DAR concept can be successfully implemented on a commercial scale. First, the behavior of the salt film, especially with regards to the growth of roll waves, must be investigated and the stability of the salt film in terms of ejection of droplets from the crests of the growing roll waves must be proven. Second, it must be shown that the falling salt film will not break down in the presence of high solar flux. Finally, high optical and thermal efficiency of the falling film and the survivability of the receiver support surface must be proven.

This report describes research performed during calendar year 1988 at the Solar Energy Research Institute (SERI) on these three technical issues related to the DAR. The following sections discuss the hydrodynamic behavior of the liquid films with special attention to the growth of waves in the film, droplet ejection from the surface of the film, thermocapillary breakdown of falling liquid films exposed to high flux, and convective and radiative heat transfer in doped and undoped salt films exposed to high flux. In some cases, the research has progressed to the point where large-scale testing (currently planned for mid-FY 1990 at Sandia National Laboratories, Albuquerque) is the next logical step. In other cases, remaining experimental or analytical

research is needed before large-scale testing is justified. The final section of this report draws conclusions based on the research completed to date and recommends follow-on research and development.

2.0 MEASUREMENT OF WAVY FILM CHARACTERISTICS

2.1 Background

A liquid film falling under the influence of gravity develops what are known as roll waves after about 1 to 2 m of flow length. These waves propagate down the film and have a peak height significantly greater than the mean film thickness. Figure 2-1 shows a falling water film at a Reynolds number of approximately 20,000 on a vertical support surface 1 m wide and 8 m high (Chavez et al. 1989). The view is from the bottom of the support surface looking up. A coloring dye was added to the water to improve visibility. Each roll wave is clearly delineated by its leading edge, which propagates down the support surface at approximately 3 m/s. The roll waves are separated by a region of very thin liquid film known as the substrate. The waves are nominally two-dimensional for the first 3-4 m of flow length. For flow lengths greater than about 5 m, the waves become strongly three-dimensional and take on a noticeable V-shape as seen near the bottom of Figure 2-1. At high Reynolds numbers typical of DAR operation, the flow in both the roll waves and in the substrate will be turbulent. Although the substrate film is not well understood, it will probably become turbulent at film Reynolds numbers beyond about 10,000.

Wavy film flow affects the behavior of the DAR in three important ways. First, development and growth of the roll waves could cause salt to be ejected from the wave peaks. Second, the very thin liquid layer (substrate) between the roll waves provides an enhanced opportunity for thermocapillary breakdown with high flux. Finally, low liquid velocities in the substrate reduce convective heat transfer between the support surface and the salt film. For a doped salt, the thin substrate with its reduced optical path length will expose the support surface to higher flux, increasing the risk of support surface overheating. In addition, waves may increase mixing in the film, leading to higher rates of convective heat transfer and reduced susceptibility to thermocapillary breakdown.

Since the DAR is sensitive to this wavy film behavior, it is clear that we need to understand this phenomenon to successfully implement the DAR concept. Although a great deal of literature is available on the general subject of falling liquid films, very little work exists on long films at high Reynolds numbers—two unique characteristics of the DAR falling film. To provide this improved understanding of falling liquid films, we undertook an experimental program aimed at developing a predictive capability for the important parameters of wavy films at high Reynolds numbers. This section describes these measurements of falling liquid films with the objective of providing a better basis for understanding droplet ejection, thermocapillary breakdown, and heat transfer, which are discussed in subsequent sections.

2.2 Experimental Method and Results

2.2.1 Water

This portion of the research effort was focused on determining the instantaneous film thickness in water and salt films at a given location in the flow path. The apparatus used to measure water film thickness is shown schematically in Figure 2-2 and consists of a 5-m long vertical 7.62-cm (outside diameter) Lucite™ tube with a flow distribution manifold at the top. (We chose the 5-m flow length based on the maximum available laboratory ceiling height. Based on our results and flow observations on vertical water films of more
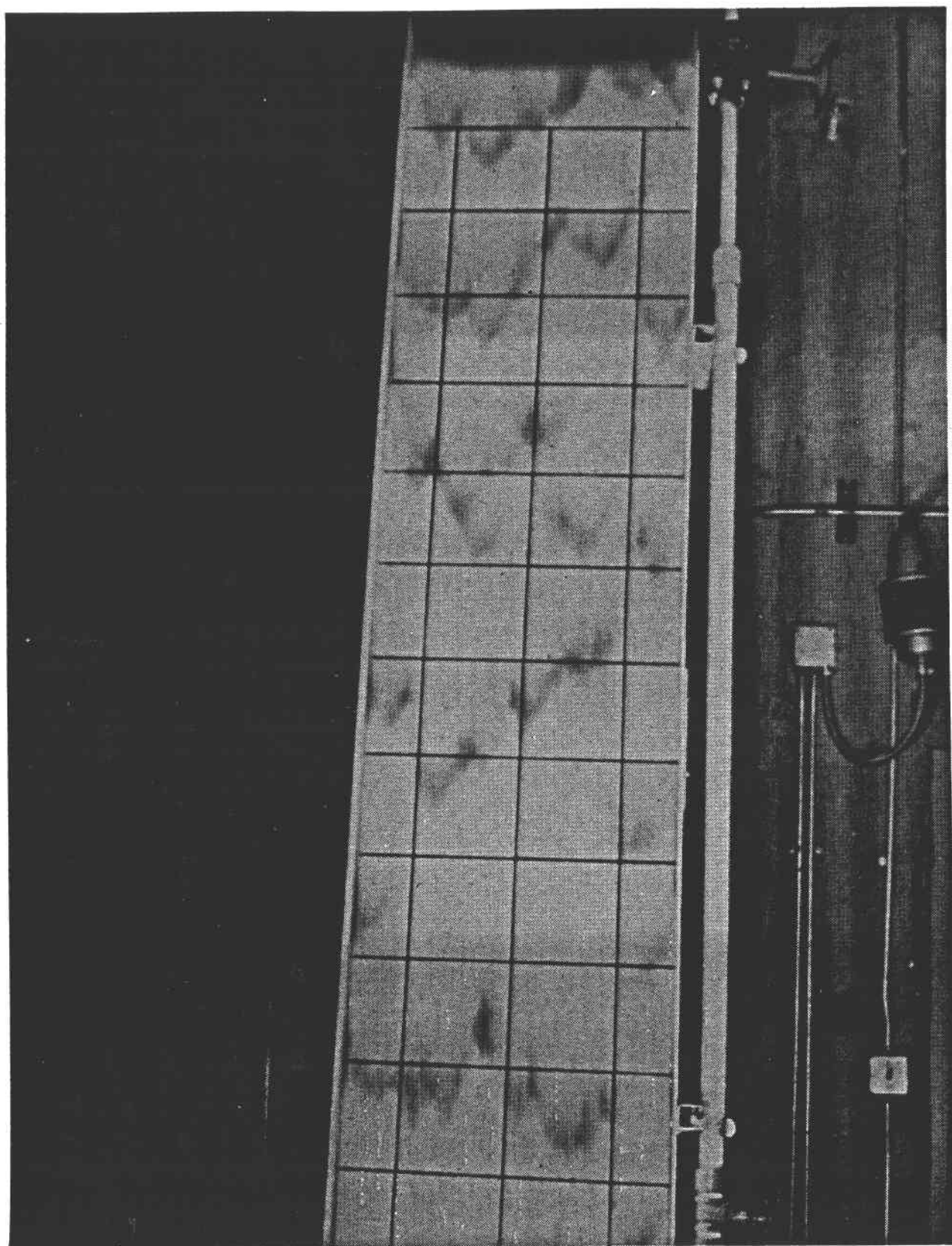
Figure 2-1. Falling water film on a 1 × 8 m support surface at a Reynolds
number of approximately 20,000. (Each square is 1 ft^2.)
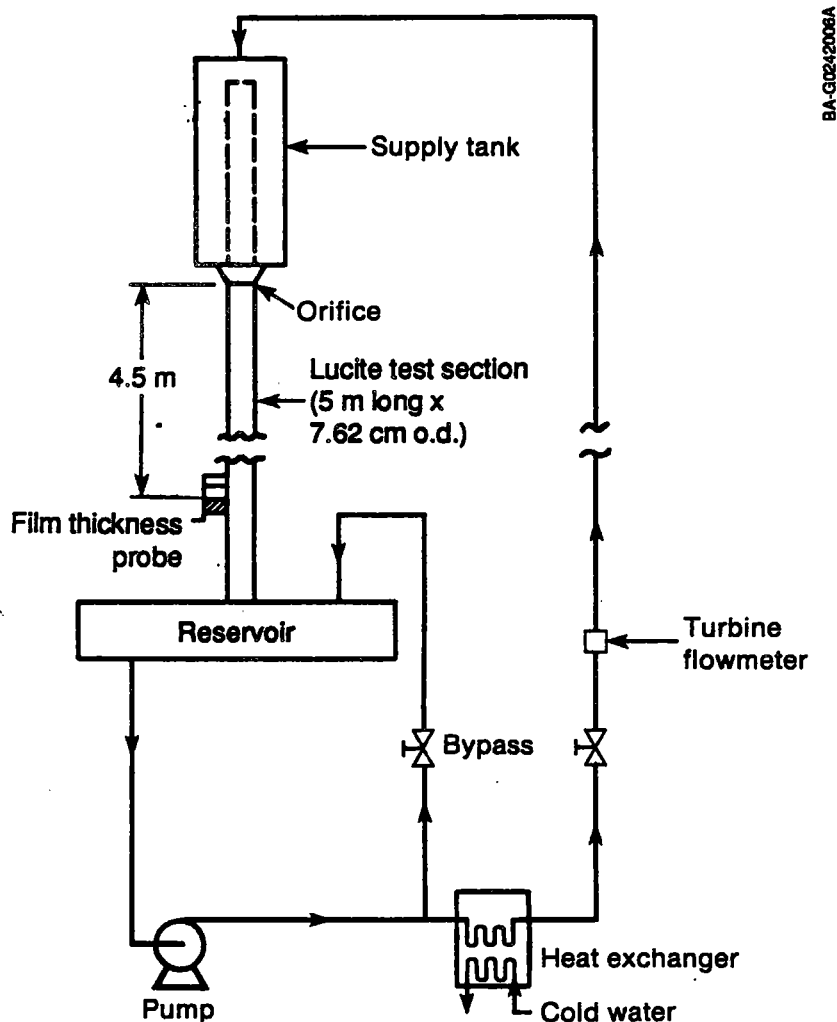
Figure 2-2. Experimental apparatus for measuring water film thickness

than 5-m length, it is now clear that the film changes significantly after 5 m.) The manifold supplied a constant water head to an orifice concentric with the tube. Replaceable orifices sized according to the desired flow rate ensured uniform water distribution around the Lucite™ tube. After flowing off the bottom of the Lucite™ tube into the reservoir, the water was pumped through a heat exchanger and then back to the distributor. The heat exchanger maintained a constant water temperature in the distributor. This arrangement made a range of Reynolds numbers from 3500 to 30,000 possible. (Recall from Section 1.0 that a commercial DAR is expected to operate in the range 23,000 < Re < 78,000.)

We determined the instantaneous film thickness in water using the conductivity probe method described in detail by Zabaras (1985). Referring to Figure 2-3, the probe consisted of an isolated pair of 0.127-mm-diameter platinum/rhodium wires implanted in the tube and spaced 2 mm apart (a second pair of wires located 52 mm downstream of the first pair allowed the measurement of wave velocity). The probe was located 4.5 m from the orifice. As the film flowed down the Lucite™ tube, the electrical resistance between these two wires

SΞRI

Lucite test section

Upstream
probe wires

Downstream
probe wires

Film flow
direction

Terminal block →

Support plate

BA-G0242005
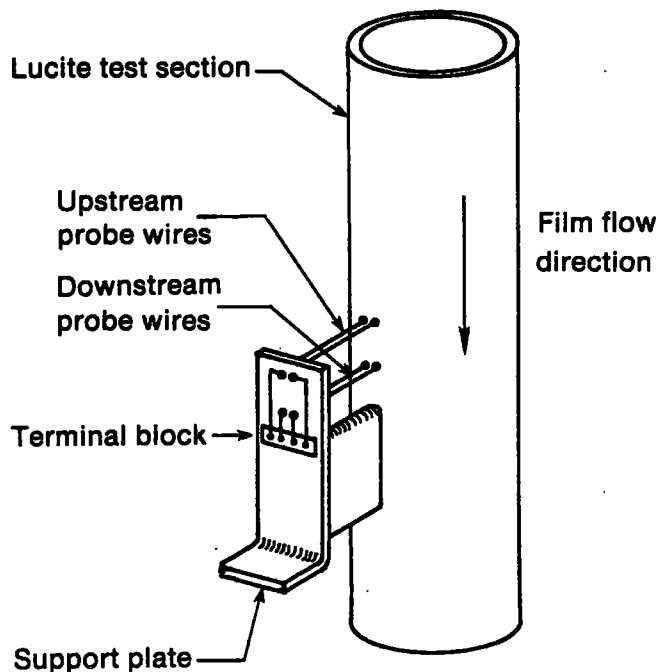
Figure 2-3. Detail of conductivity probe for
measuring instantaneous film
thickness and wave velocity

varied inversely with the instantaneous film thickness at the probe location.
An electronic circuit measured the electrical resistance between the two wires
and put out a voltage inversely proportional to this resistance. (The circui-
try is shown in Appendix A.) This voltage, which was proportional to the film
thickness, was sampled at 1 kHz. The instrument frequency response was suffi-
cient to resolve a rise time in the film thickness of about 10 mm/ms, which
was at least an order of magnitude greater than required.

We calibrated the film thickness probes by placing the Lucite™ tube horizon-
tally and building a dam around the wires to form a calibration cell. A water
level was established in the cell; its height determined accurately using a
height gauge. We correlated the resulting voltage output against the water
level and used this calibration curve to infer film thickness from the voltage
output during an actual run. We found that it was important to maintain the
calibration cell temperature at the temperature planned for testing because
the water electrical conductivity is a strong function of temperature. Fre-
quent calibrations eliminated the influence of water impurities on the water
conductivity. A typical calibration curve is shown in Figure 2-4.

Mean film thickness, determined by averaging the conductivity probe output for
given flow conditions, agreed within ±5% of that value predicted by a correla-
tion developed by Takahama and Kato (1980) from data at Reynolds numbers
<8000:

$$\bar{\delta} = 0.228(v^2/g)^{1/3} Re^{0.526} \quad . \tag{2-1}$$

Because the conductivity probe had excellent linearity and the measured mean
film thickness agreed with previous data at lower Re, we anticipated that the
uncertainty in our measured instantaneous film thickness would be less than
±5%.

7
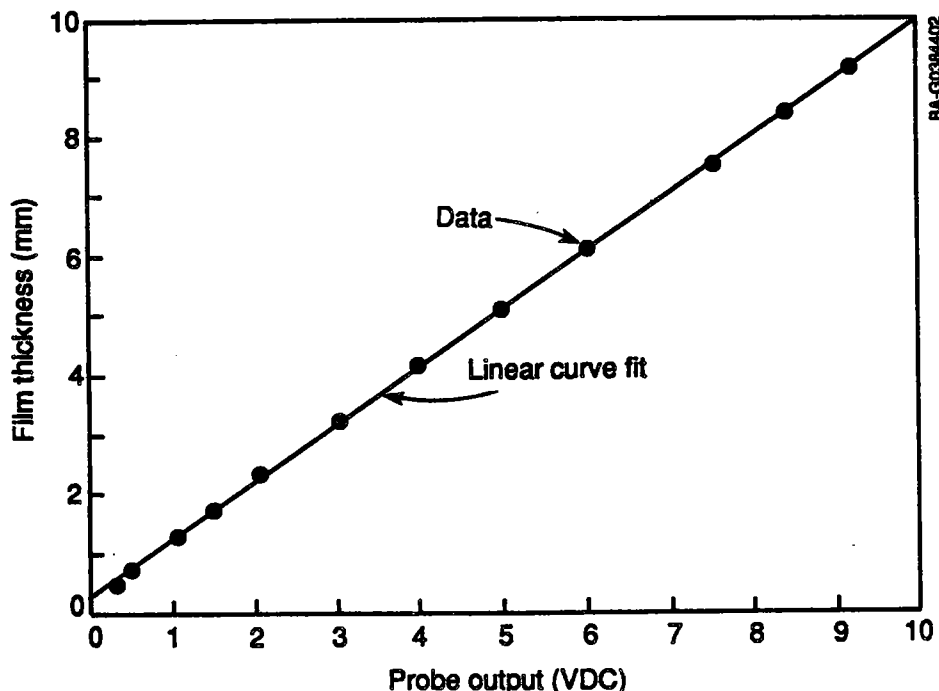
Figure 2-4. Typical conductivity probe calibration curve

A representative sample of the conductivity probe output for three values of Re is shown in Figure 2-5. This figure clearly shows the peak heights, spacing, and substrate thickness and lengths for the Re range measured. Note that the view in the time domain as seen in Figure 2-5 appears compressed compared with the view in the space domain as seen in Figure 2-1. This is because of the relatively high speed of the roll waves. Generally, we see the following trends in Figure 2-5: as the Reynolds number was increased, more peaks formed in the one-second sample. In fact, at Re = 35,425, the waves are spaced very close to each other, nearly eliminating the substrate. The peak heights became larger, and the substrate thickness increased. In addition, the surface of the film took on a more irregular, fine-grained texture.

To quantify these observations, data records at Re ≅ 6000, 12,000, and 18,000 were reduced and analyzed in detail using the following procedures. A continuous record of 7 s was taken either from one probe at 1 kHz sampling frequency or from both probes at 2-kHz sampling frequency with a Hewlett-Packard 3437 high-speed digital voltmeter controlled by a Hewlett-Packard Vectra personal computer with an IEEE interface. A total of 30 such records was taken, 10 with 1 probe and 20 with both probes. We used the single-probe data to give amplitude-related information. We used the two-probe data only to give wave speeds by determining the elapsed time for the wave peak to pass between the two probes. Thus, 210,000 data points were used for each flow condition (Reynolds number) to produce information on mean film thickness, mean wave peak height, mean substrate thickness, mean substrate exposure time, and wave frequency.

The mean film thickness $\bar{h}_s$ was determined by averaging all film thickness data points for the run. A wave peak is defined as the largest film thickness in a continuous string of film thickness measurements that exceeded the mean film
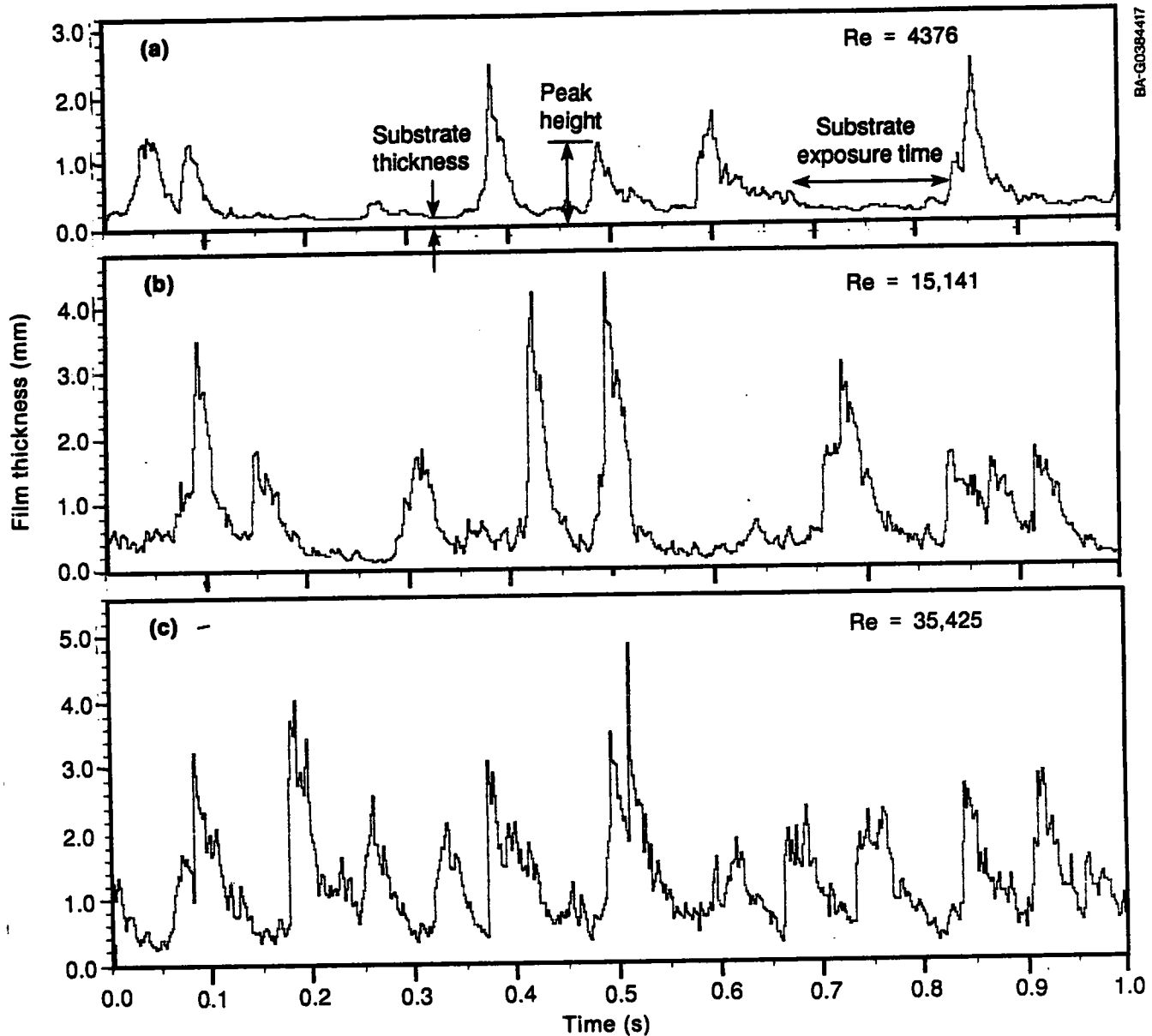
Figure 2-5. Conductivity probe signal for (a) Re = 4376; (b) Re = 15,141; and (c) Re = 35,425, showing important characteristics of the wavy film 4.5 m from the distribution

thickness by at least 20% for at least 10 ms. This criterion eliminated spurious peaks caused by droplets hitting the probe wires. The mean wave peak height $\bar{h}_p$ is the average of all such peaks found in the data.

The mean substrate thickness $\bar{h}_s$ is calculated from the area under the probability density curve from zero film thickness to the film thickness at which the maximum in the probability density results; i.e.

$$\bar{h}_s = \int_0^{P_{max}} p(h) \, dh \quad . \tag{2-2}$$

The probability density p(h) was determined first by sorting all film thickness measurements into bins of discrete ranges of film thickness such that each bin contained the number of film thickness measurements in that range and second by subsequently scaling the values of each bin so that

$$\sum_{\text{bins}} p(h)\, \Delta h = 1 \qquad\qquad (2\text{-}3)$$

This definition of mean substrate thickness (Eq. 2-2) is somewhat arbitrary. By comparing several probability density curves with their associated film thickness records, such as in Figure 2-5, it became clear that the maximum probability density occurred near the film thickness that appeared most representative of the substrate thickness, as seen in a plot of film thickness versus time.

The substrate exposure time τ_s was defined as the length of time from when the film thickness fell below 1.2 times the mean film thickness to the next time that it rose above 1.2 times the mean and for which the preceding and following wave peaks lasted at least 10 ms. An average of all such durations gives the mean substrate exposure time.

The wave velocity was determined from the peak in the cross correlation of the signals from the two conductivity probes (which were separated by a known distance). Wave frequency was determined as the number of peaks from the first probe divided by the total run time. Overall wavelength λ_L was determined as the wave velocity divided by this wave frequency. Appendix B is the computer program used to reduce the film thickness data as just described.

Data for three values of Re, approximately 6000, 12,000, and 18,000, with the probe located 4.5 m downstream from the water inlet are depicted in Figure 2-6. Although this Re range falls below the expected Re range for a commercial receiver, it is possible to determine important trends with Re and to conjecture as to the behavior in the commercial receiver Re range.
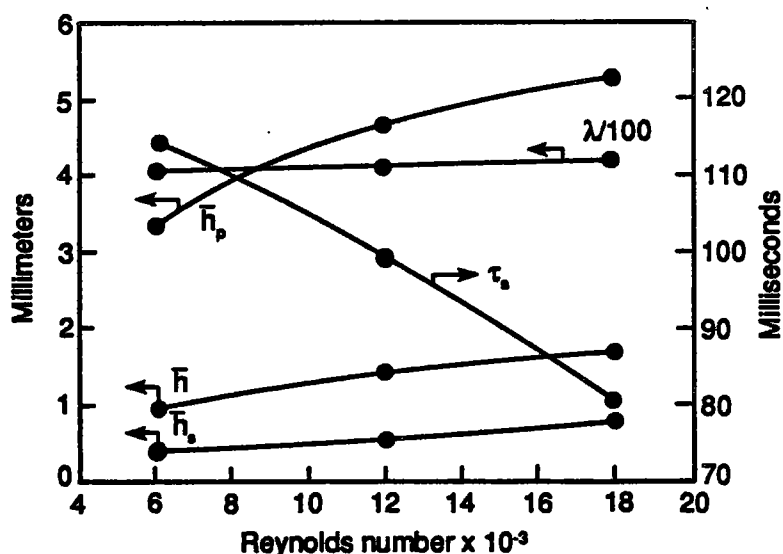
Figure 2-6. Characteristics of falling water films as a function of Reynolds number

The overall wavelength was essentially constant at 410 mm, but the substrate exposure time decreased significantly by about 27%. In addition, the substrate thickness increased substantially, about 100%, as Re increased. The significance of this is that the substrate had a reduced susceptibility to thermocapillary breakdown as Re increased because the substrate became thicker and was exposed for a shorter period of time. Note, however, the rapid growth in peak wave height as Re increased, which implies increased susceptibility to wave breaking and droplet ejection for high Reynolds number flows. Statistical analysis of the data revealed that the peak height, the substrate exposure time, and wave velocity were all random. At Re = 17,700, we observed some peaks up to 10 mm in height, the maximum height that the conductivity probe could measure.

2.2.2 Molten Salt

Film thickness measurements in molten salt films were made in a flow loop that provided a continuous flow of molten nitrate salt. The loop, shown in Figure 2-7a, consisted of a trace-heated, Inconel molten salt tank with a cantilever pump immersed below the salt level. A variable speed pump delivered salt at flow rates up to 170 L/min to an inlet manifold at the top of a 5-m-long flow support surface. The manifold distributed the salt uniformly over the 0.27-m width of the support surface via a weir. A bubbler was used to sense the level of liquid over the weir; this was then translated into salt flow rate. Figure 2-7b shows a cross-section diagram of the flow support surface fabricated from a 3.2-mm stainless steel sheet. The 5-cm rolled-up edges of the support surface were necessary to contain the salt film within the confines of the 0.27-m width. Typically, a small quantity of salt flowed down the inside surface of these edges. Heaters behind the support surface maintained the salt and the salt riser in a hot state ready for testing. Heaters on the support surface edges minimized thermal distortions in the support surface. Salt draining off the bottom of the support surface flowed into a sump where it was returned to the salt tank. The entire support surface assembly could be tilted to angles from vertical to a 15-deg back tilt. Data at Re up to 30,000 were taken with this apparatus.

The width of the support surface was a compromise. Larger widths would be desirable but would lead to lower maximum Reynolds numbers with the available salt pump. Smaller widths would allow testing at Reynolds numbers closer to commercial operation but would increase edge effects. At 0.27-m width, the only noticeable edge effects were near the weir in the form of diagonal waves. These disappeared as soon as the roll waves formed.

Adapting the conductivity probe to molten salt film thickness measurements was difficult due to high temperatures, salt corrosion, etc. Therefore, a contact probe was used to measure the wave height for the salt film. The probe was attached to a micrometer that could be used to position the probe point a specified distance normal to the support surface. This assembly was attached to the support surface framework (but isolated electrically) at various distances downstream from the inlet manifold. The micrometer was zeroed against the support surface with salt flowing then backed out to a specified distance called the measurement height. Electrical contact between the probe and the salt film indicated that the salt film present was at least as thick as the distance set between the support surface and the probe. This signal was converted to a percent-on signal using a Hewlett-Packard 3437 high-speed
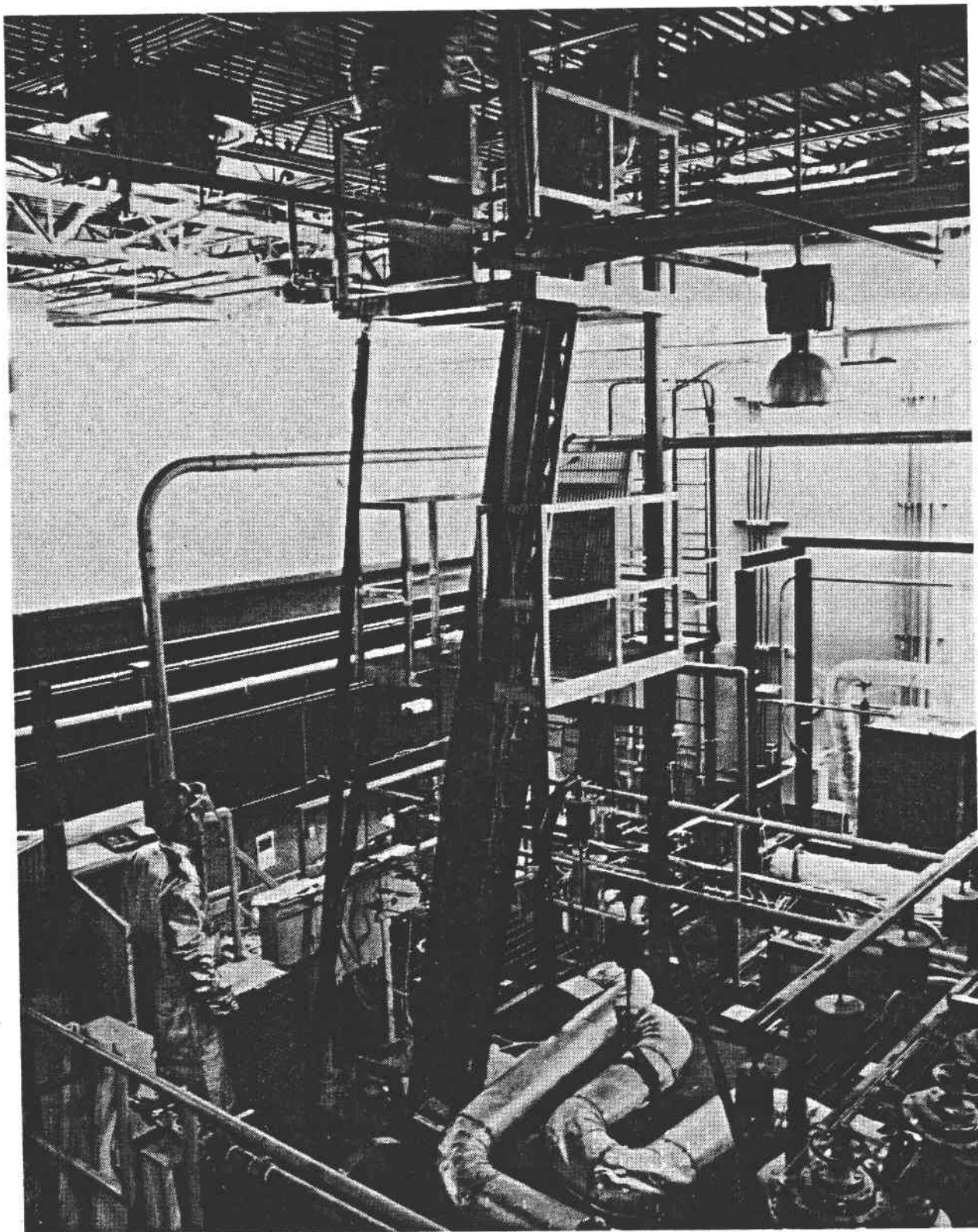
Figure 2-7a. Test loop used for measuring film thickness of molten salt
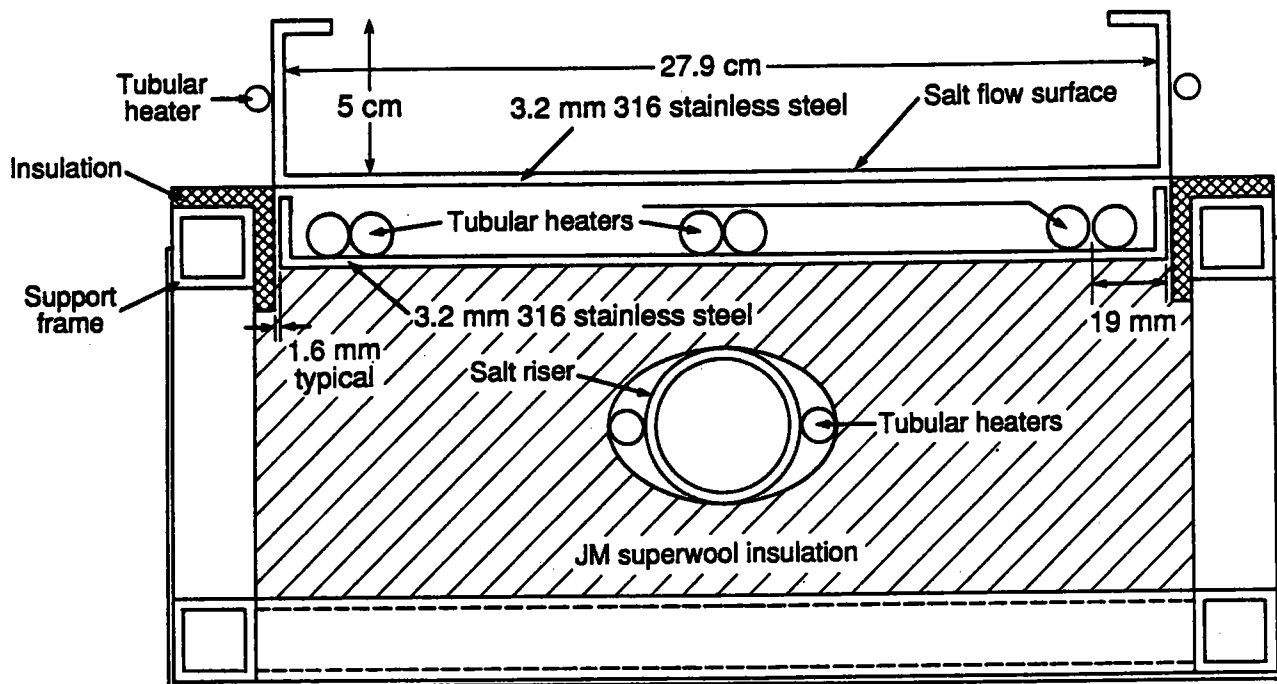
Figure 2-7b. Cross-section of 5-m support surface used for salt film thickness measurements

digital voltmeter that sampled the probe signal for 10 s at a 1000-Hz sample rate and determined the percentage of time that electrical continuity was detected. This was equivalent to the percentage of time that the salt film was thicker than the measurement height.

Figures 2-8 and 2-9 show the film thickness profile at two temperatures, 350° and 400°C, 2.5 m from the weir. In Figure 2-8, the Reynolds number was held at 20,000 by adjusting the flow rate between the two temperatures. In Figure 2-9, the flow rate was held approximately constant for the two temperatures. The purpose of these tests was to determine if there was any particular advantage to using a Reynolds number as an independent parameter as opposed to simply using flow rate. Looking at these two figures, we can see that the wave profiles are not solely dependent on Reynolds numbers, or the profiles for the two temperatures in Figure 2-8 would be in agreement. In fact, it appears that in holding the flow rate constant, the profile in Figure 2-9 produced slightly better agreement. Therefore, we chose to use flow rate as the independent parameter and to acknowledge that temperature has a small influence on wave profile.

Figure 2-10 shows how the salt film thickness profile varies with distance down the support surface at a fixed flow rate of 75 L/min for the salt at 15 deg from vertical. Near the inlet the film is smooth as evidenced by the steep slope of the percent in curve near 0.5-mm film thickness at 1 m from the weir. Further down the support surface, we see that the waviness began as the slope of the curve decreased. We also see that the wave peaks increased in height. The figure supports the contention that the waves were essentially developed after 3 m, as the film profiles are quite similar for 2.5, 3.5, and 4.5 m from the weir. The differences between the 2.5-m data and the 3.5-m or 4.5-m data may signify that the waves were not fully developed until 3.5 m.
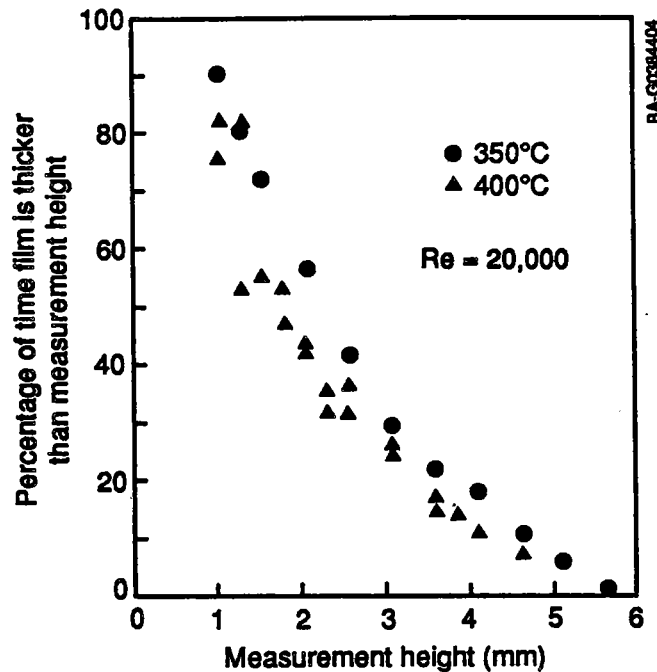
Figure 2-8. Salt film thickness profile at two temperatures, fixed Re, and 2.5 m from weir. Tilted angle is 15 deg from vertical.
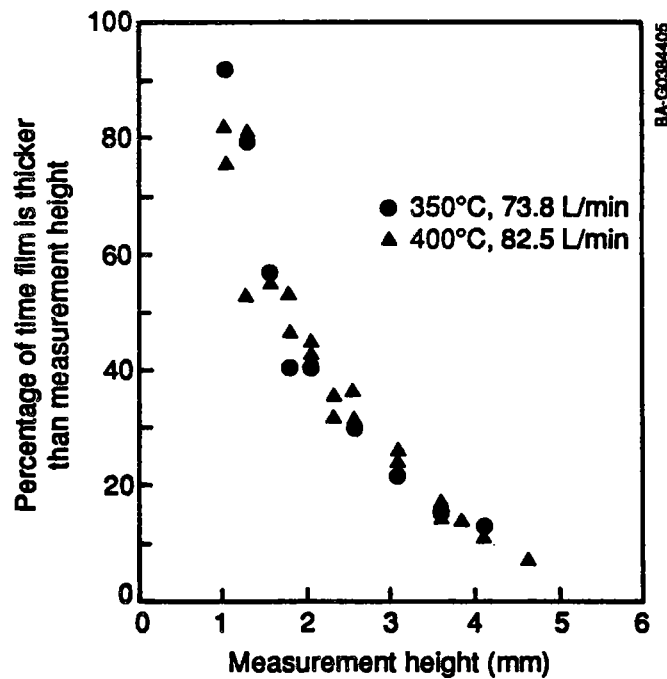
Figure 2-9. Salt film thickness profile at two temperatures, approximately fixed flow rate, and 2.5 m from weir. Tilted angle is 15 deg from vertical
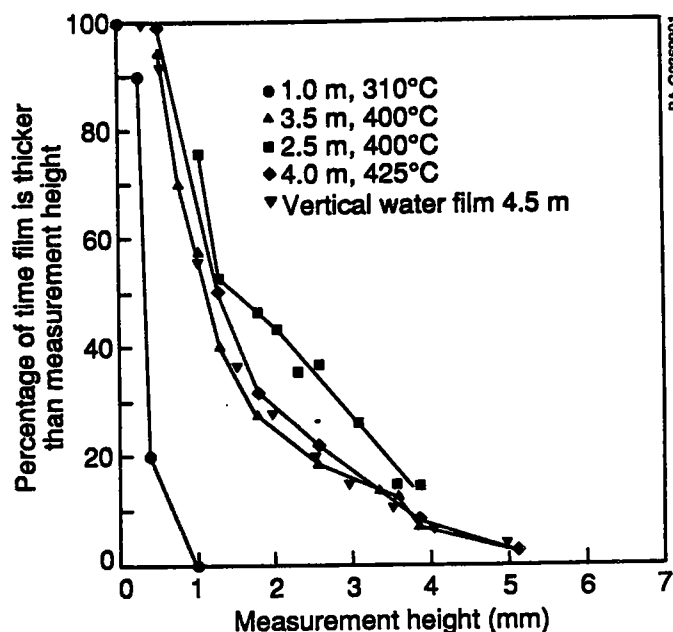
Figure 2-10. Salt film profile at various distances from the weir at 75 L/min for salt and a water film profile at equal Reynolds numbers (17,700)

Figure 2-10 also compares wave profiles in water with those in salt at approximately equal Reynolds numbers. Data taken with the conductivity probe in the vertical water film were converted to an equivalent percent on-time to allow direct comparison with the salt data. Table 2-1 compares test conditions for both fluids.

The water data for a 4.5-m flow length compare very favorably with the salt data at a 3.5- and 4.0-m flow length, indicating the similarity in wave development between the two fluids. Experiments performed in water, which are much more easily carried out, can reliably give information regarding wave peak height and substrate thickness for molten salt films.

Figure 2-11 gives the median salt film thickness (the thickness that results in a 50% on-time) as a function of flow rate and distance from the weir. At a given distance from the weir, the increase in median film thickness with flow rate is clearly seen. Interestingly, the median film thickness at a given flow actually decreased slightly after the waves were well developed, e.g., after about 2.5 m from the weir. For reference, the Re range in Figure 2-11 is 15,000 to 29,500.

Table 2-1. Test Conditions for Water and Salt for Figure 2-10

Fluid	Orientation	Re	Flow Length	Plot Symbol
Water	90 deg	17,700	4.5 m	▼
Salt	75 deg	19,100	4.0 m	◆
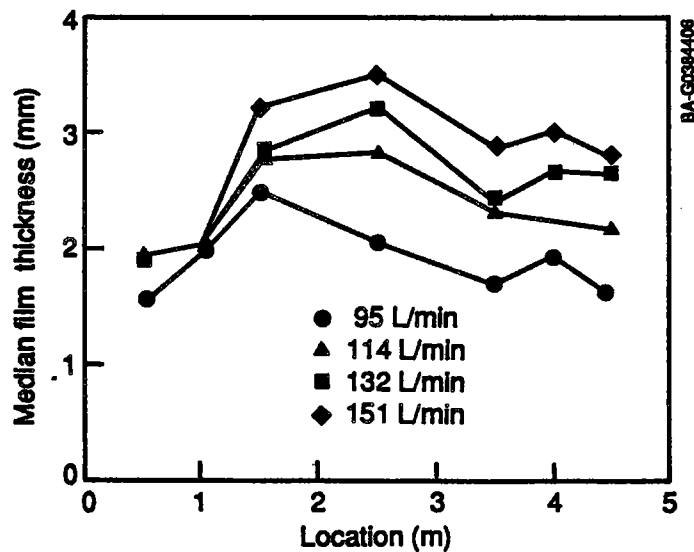
Figure 2-11. Median salt film thickness
at various flow rates and
distances from weir

Wave profile dependence on salt flow rate is shown in Figure 2-12. Here the wave profile in the wavy flow regime at L = 2.5 m is shown for a wide range of flow rates, 76 to 170 L/min. In Section 3.0 we show that for this range of flow rates, the mass ejection approximately doubled. From Figure 2-12 we see that the peak wave height (10% on-time) increased monotonically by about 50% over this flow rate range and the median wave height (50% on-time) approximately doubled. Thus, the close tie between wave growth and droplet ejection was demonstrated.
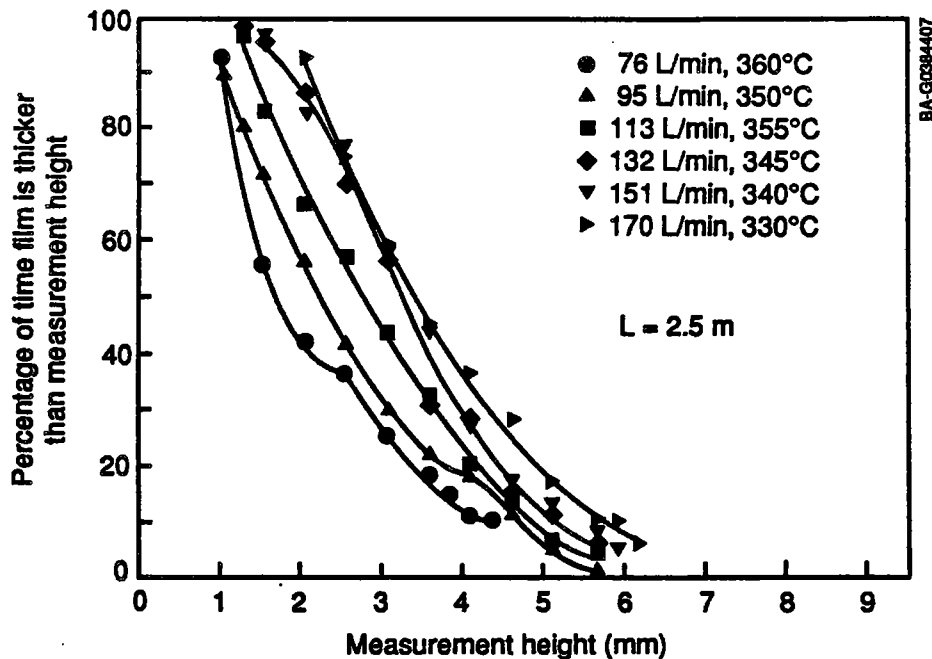
Figure 2-12. Salt film thickness profile as a function
of salt flow rate 2.5 m from weir

2.3 Summary

Data presented in this section demonstrate several features of falling liquid films that affect the technical feasibility of a commercial direct absorption receiver. Film thickness measurements in water demonstrated the wavy nature of falling films that are longer than about 1-2 meters. After this flow length, roll waves developed in the film. These waves moved down the film at about 3 m/s and were separated by a thin, slow moving liquid film called the substrate. The nature of the substrate could affect its survivability in the high flux environment expected for a DAR. However, as the Reynolds number was increased, the substrate appeared to become more robust as it thickened and its exposure time shortened. The wave peaks, however, grew significantly as the Reynolds number was increased, which could lead to wave breaking and droplet ejection. Film thickness measurements in salt showed that the waves became well developed between 2.5- and 3.5-m flow lengths for Reynolds numbers of approximately 18,000. Film thickness measurements in water agreed very well with the measurements made in the salt film. The increase of wave height with Reynolds numbers found in water was also found in salt--an increase in Re from 15,100 to 29,500 almost doubled the median film thickness. The tendency for wave breakage and droplet ejection in salt was therefore demonstrated. Presenting data with a Reynolds number as an independent parameter does not seem advantageous; using flow rate as the independent parameter is at least as good, if not better, in suppressing the explicit effect of temperature.

3.0 DROPLET EJECTION

3.1 Background

The general characteristics of falling wavy films discussed in Section 2.0
included the potential for ejection of salt droplets from crests of growing
roll waves. Loss of molten salt from a DAR falling film in this manner is
undesirable for several reasons:

- It would represent a loss of salt inventory, therefore, increasing plant
  operating cost.

- At least some of the salt would find its way to the heliostat reflective
  surfaces. Although one would expect the droplets to freeze before reaching
  groundlevel, any that adhere to the heliostat reflective surface would
  reduce the optical efficiency of the heliostats. This would reduce the
  plant efficiency or require more frequent heliostat washing.

- Salt ejected from the receiver could pose a potential safety hazard for
  plant personnel.

- Transport of fine salt droplets to areas surrounding the plant could raise
  environmental concerns.

Figure 3-1 shows ejection of water from a vertical film on the outside of a
75-mm diameter pipe, 4.5 m from an orifice-type distributor at a Reynolds num-
ber of 40,000. The crest of a roll wave is clearly visible near the top left
of the figure; and just below the
wave, a finger of liquid can be
seen. The droplet at the end of
this finger has torn off and has
been ejected into the air. Analysis
of a series of video tapes showed
that approximately 15% of all such
water waves will eject droplets in
this manner.

Our flow visualization studies, es-
pecially those for flow lengths and
Reynolds numbers beyond those typi-
cally reported in the literature,
prove enlightening and suggest sev-
eral possible mechanism for droplet
ejection. Figure 2-1 shows some im-
portant features. As the roll waves
first appear, they are essentially
two-dimensional; e.g., their wave-
fronts are essentially horizontal.
After traveling 3-4-m, they begin to
take on a three-dimensional V-shape,
as noted in Ganchev, Kozlov, and
Nikitin (1975). Close inspection of
these V-shaped waves reveals that
liquid collects at the bottom of the
V producing a hanging droplet of
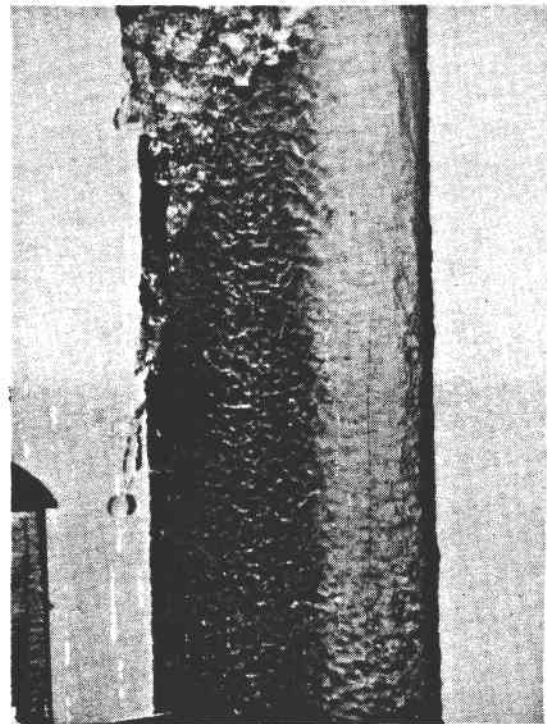
**Figure 3-1.   Droplet ejection from a
vertical water film**

about 5 mm diameter. Eventually, as shown on the bottom left portion of Figure 3-1, the droplet is pulled away from the film, probably by aerodynamic forces. That is, as the droplet builds up, the force of the adjacent air can undercut the droplet and can pull it away from the main body of the film. This undercutting could also pertain to the early quasi-two-dimensional waves and could contribute to droplet ejection at shorter flow lengths.

Observations of water films longer than 5 m (Chavez et al., 1989) showed that once a V-shaped wave collected sufficient water at the bottom of the V to begin shedding droplets, a continuous dripping began at that point of the wave for the remainder of the wave's lifetime. If it is windy, which is almost certain for a receiver located at the top of a 100+ m tall tower, these droplets will be carried away from the film.

Since the waves did not all move at the same velocity, occasionally a wave would overtake other waves. Our observation showed that this overtaking often causes liquid ejection. The wave being overtaken acted as a ramp and provided momentum normal to the mean film surface for the faster overtaking wave and caused the overtaking wave to eject liquid. This overtaking did not appear until after about 4 m.

The corrugations appearing on the wave surface just behind the wave crest in Figure 3-1 were a result of turbulence that could cause droplet ejection when the turbulent eddies burst at the surface. Based on the relatively small scale of the eddies evident in the figure, we expect that the resulting droplets would· be much smaller than the ones originating from the bottom of the V.

Several important parameters control droplet ejection from a falling liquid film. The most obvious is liquid flow rate, or more specifically, liquid flow rate per unit width. The tilt angle of the support surface plays a role through the effect of gravity. Finally, droplet ejection should depend on flow length and fluid properties.

Although a significant amount of qualitative work has been completed regarding the droplet ejection problem, we now need quantitative data. If we take preventative measures to reduce the magnitude of droplet ejection, we must have baseline data for comparison purposes, e.g., to see if the preventative measures provide any improvement. In addition, based on the difficulties caused by liquid ejection in a DAR as previously discussed, a quantitative measure of the problem is required to determine how severe these difficulties really are. Finally, any efforts to model or correlate the phenomenon will require experimental data for validation.

This section presents experimental data in which droplet ejection was measured along a 5-m support surface with a flowing salt film for a range of flow rates and salt temperatures. These data quantify the magnitude of the droplet ejection problem for DAR, demonstrate the influence of the controlling parameters, and provide evidence as to whether it may be feasible to reduce the magnitude of the problem.

3.2 Experimental Method and Results

The flow loop that provided a continuous flow of molten nitrate salt is described in Section 2.2.2. We determined the liquid mass ejection rate by

collecting droplets ejected from the film at various distances downstream from
the weir. For each test, a measurement at a single distance was used. Typi-
cally, a half hour passed for the apparatus to equilibrate with salt flowing
before we began collecting salt droplets. A collection plate formed from alu-
minum foil was placed at a specified distance from the weir for a specified
period of time, typically 30 or 60 min. The weight of the foil tray before
and after the test, determined using a digital balance, gave the mass ejected
at that height, generally expressed as grams per hour with a resolution of
0.005 g/h. The tray width was the same as that of the support surface, and it
was approximately square. The tray was placed so it touched the rolled edges
of the support surface, as seen in Figure 2-7. The ejected droplets therefore
were collected 5 cm from the salt support surface and represent the total mass
of salt ejected from the film (but not recaptured by the film) between the
weir and that downstream location. It is to be expected that some droplets
fell outside the width of the collection tray, although this uncertainty was
not estimated. Most tests were run at a fixed volumetric salt flow rate. All
tests were run with the support surface tilted back from vertical by 15 deg.
Heat loss from the salt film to ambient resulted in a decrease in the salt
temperature delivered to the weir during the run. Thus, droplet ejection data
were expressed as a function of salt flow rate with the range of salt tempera-
ture given as a parameter.

3.2.1 Flow Observations

At comparable Reynolds numbers the behavior of the molten salt film was simi-
lar to that of a vertical water film with the exception of the behavior at the
inlet region, which depended on the method of liquid introduction. Using a
weir distributor for the molten salt produced a slightly different behavior
for the first 0.5 m of the flow compared with the water film described in Sec-
tion 2.0. Whereas the water film was glassy smooth just after the orifice,
the salt film exhibited waves with their axes in the direction of flow, much
like fingers reaching over the weir in the flow direction. These waves per-
sisted for some distance downstream, approximately 0.5 m, and tended to move
about laterally to some extent. Other than the longitudinal waves, the sur-
face of the film was quite smooth.

At about 0.25 m downstream of the weir, random spots of turbulence appeared
and disappeared. These spots, best characterized by the rough surface seen in
Figure 3-1, tended to exist in regions shaped like an inverted V and gradually
increased in spatial extent and lifetime over the next 0.2 m until the entire
film was covered with the rough texture. The longitudinal waves that origi-
nated at the weir seemed to persist to some extent through this region. It
appeared then that the film was laminar up to 0.25 m, transitioned to turbu-
lent flow up to 0.45 m, and was fully turbulent after 0.45 m from the weir.

Consistent with data presented in Figure 2-10, the roll waves developed over
the next meter; and after about 2 m total distance from the weir, the roll
waves were clearly present. By the third meter, the waves were fairly well
developed and distinct. For example, with a salt inlet temperature of 310°C
and a flow rate of 114 L/min, we observed well-defined roll waves 2.5 m below
the weir. The behavior over the last half of the support surface appeared
more or less developed, that is, the character of the flow did not change much
over this region, which was also consistent with that shown in Figure 2-10.
Although the waves were not strictly two-dimensional, they did not attain the

pronounced V-shape observed in water film flows longer than 5 m, as discussed previously. For distances of less than 4 m, the waves did begin taking on the V-shape, but it was not very exaggerated at that point.

3.2.2 Wave Speed

We measured the wave speed for the salt film at a tilt angle of 15 deg using a shuttered video camera focused on the 3-4-m flow length range and then analyzing the video tape at a reduced speed. In Figure 3-2, the data are compared with wave speed for the vertical water film measured using the technique described in Section 2.2.1. Data for the salt are about 25% lower than those for the water. This difference is probably attributable to the different tilt angles and different properties of the fluids for the two tests. Nonetheless, the data demonstrate that the differences are not great and that in salt, we can expect wave speeds of 3-4 m/s. These data are significant because if the adjacent air undercutting the liquid wave is an important mechanism, then the wave velocity is the controlling parameter. In addition, as pointed out later in this section, a concave support surface may reduce wave growth by adding a centrifugal force to the mass of liquid in the wave. Wave velocity is obviously an important consideration here.

3.2.3 Droplet Ejection

Since the quantity of salt ejected from the film is the main interest in this section, most of our attention was directed there. First, we determined the flow parameter that controls droplet ejection. We found that temperature affects droplet ejection very little; and since temperature mainly affects viscosity, we concluded that a parameter independent of viscosity was more appropriate than the film Reynolds number, for example. We found that the best dimensional parameter is flow rate (mass or volume) per unit flow width. Since we always tested with a support surface width of 0.279 m, we chose to use the feed salt flow rate, expressed as liters per minute, as the controlling parameter.
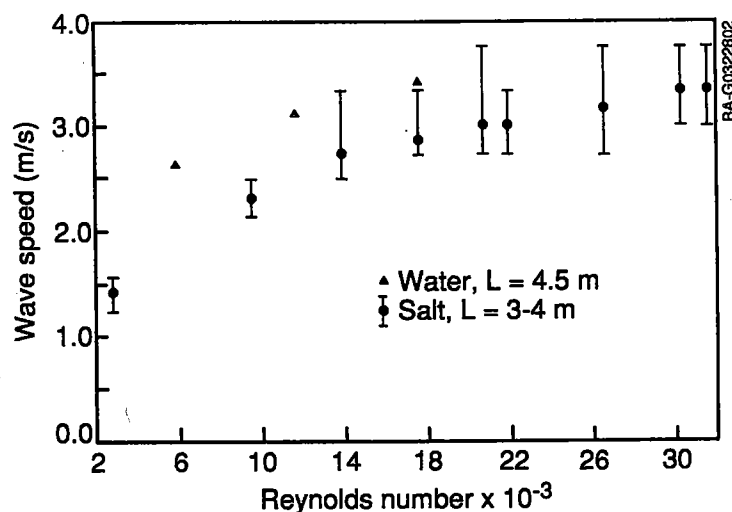
Figure 3-2. Wave speed in water and salt

Measurements near the weir proved to be quite sensitive to perturbations in the support surface. We found that it was necessary to carefully inspect the surface and remove rough weld beads and other perturbations before collecting data. The presence of these imperfections caused large local liquid ejection, as evidenced by the presence of localized areas on the collection tray rather than a nearly uniform distribution. This sensitivity suggests that in a commercial receiver, care must be taken to provide as smooth a flow surface as possible. This subject is covered in more detail later in this section.

In the process of collecting samples of ejected salt, it became clear that ejection generally occurred in the form of droplets of 0.5 to 2 mm in diameter accompanied by a mist with droplet diameters of 0.1 mm diameter and smaller. This mist uniformly covered the collection tray, but the droplets were more closely congregated near the salt film-side edge of the tray. Quantifying the mist ejection rate was not possible due to the extremely small quantity collected. Although the mass of droplets increased as the tray was moved to progressively lower locations, the mist was more or less consistent for all locations. The mist contributes very little to the total mass ejected but could be carried great distances by prevailing winds. Although upward natural convection currents could cause the mist droplets to be carried away from the collection tray, we did not see evidence of this on the underside of the tray.

We attempted to determine the source of the mist by measuring droplet ejection at locations close to the weir but found no significant quantities until the film became turbulent. Figure 3-3 shows mass collected as a function of flow length at a fixed flow rate of 113 L/min near the weir with the location of turbulence initiation given as a reference. Recall from the discussion of flow observations that the film was laminar for the first 0.25 m, it changed to a turbulent flow at 0.45 m, was fully turbulent after 0.45 m, and did not exhibit roll waves until a 2-3 m flow length. These ranges correspond well with the data seen in Figure 3-3. The quantity of mass ejected was very
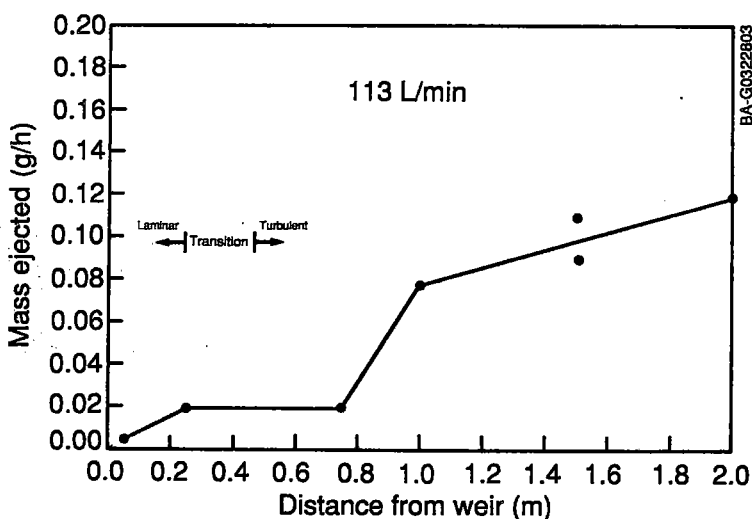
Figure 3-3. Droplet ejection near the weir, 113 L/min

small in the laminar range and increased after the 0.25 m point, where the film began to exhibit turbulent spots. It then showed large increases in the regime when the film was fully turbulent but did not yet exhibit roll waves. Note that droplets were also present in all samples, but they were very small and sparse for the samples at L ≤ 1 m. It appears, then, that the bursting of turbulent eddies at the salt surface, as described previously, is a likely explanation for the mist. If this is the case, operating a DAR salt film in the turbulent regime, desirable for increased heat transfer (discussed in Section 5.0), will result in mist generation along nearly the entire film.

Figure 3-4 shows droplet ejection as a function of flow length with salt flow rate and temperature as parameters. For reference, a commercial receiver will operate with a maximum flow rate of approximately 200 to 225 L/min (per unit width equal to the test support surface width), which is 30% higher than the highest flow we could achieve. Except for the high flow rate point at 0.75 m, the data exhibited a linear trend on the semilogarithmic plot. That is, the mass ejected increased exponentially with flow distance. If this curve is extrapolated for a 13-m-high receiver, it becomes clear that a substantial loss of salt resulted.

High flow rates produced exceptionally high ejection near the weir; note the 170 L/min point at 0.75 m and the 155 L/min point at 0.5 m. The reason for this behavior is that the longitudinal waves that originated at the weir, as discussed earlier, became large and unstable at high flow rates and threw liquid off the film near the weir. We found that very large droplets, 5 to 10 mm in diameter, were produced by these waves as close to the weir as 0.75 m. This high flow rate behavior did not persist past the point where the longitudinal waves disappeared (see the 170 L/min point at 4 m). Although a commercial DAR inlet manifold will differ significantly from a weir (Chavez, Tyner, and Couch 1988), it is not clear whether the same longitudinal waves will result from operating such a manifold at the required high flow rates.
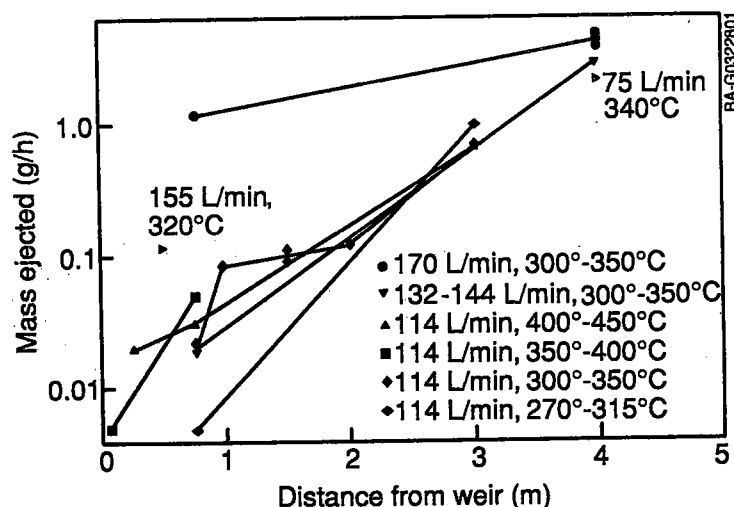
Figure 3-4. Droplet ejection as a function
             of distance from weir, flow
             rate, and temperature

Low temperature seemed to significantly reduce droplet ejection near the weir, note the 114 L/min point at 0.75 m, which was at 270°C salt temperature. This low temperature effect also became negligible when the roll waves became predominant; note the 114 L/min point at 3 m (315°C). Most likely, the effect was one of high viscosity and the viscosity's effect on delaying the initiation of turbulent flow. As stated before, overall, temperature seemed to play a minor role in droplet ejection.

During a majority of the tests described in this section, the support surface was essentially flat. However, toward the end of the test program, we found that the support surface began taking on a convex shape with respect to the salt side of the support surface. The curvature depended on salt temperature, becoming less noticeable for higher temperature salt. Figure 3-5 shows the extent of the support surface curvature, expressed as deflection from the plane of the supporting framework as a function of distance from the weir and salt temperature. At the lowest salt temperature (265°C), the maximum deflection was about 30 mm; and at the highest temperature (486°C), the maximum deflection was 16 mm. This behavior was repeatable.

Although these support surface deflections appeared to be quite small, especially when the full length of the support surface was considered (resulting support surface slopes were small); they appeared to have a major effect on salt ejection (see Figure 3-6). In this figure, the rate of mass ejection at various distances from the weir (measured concurrently with data in Figure 3-6) is plotted with salt temperature as a parameter at a fixed flow
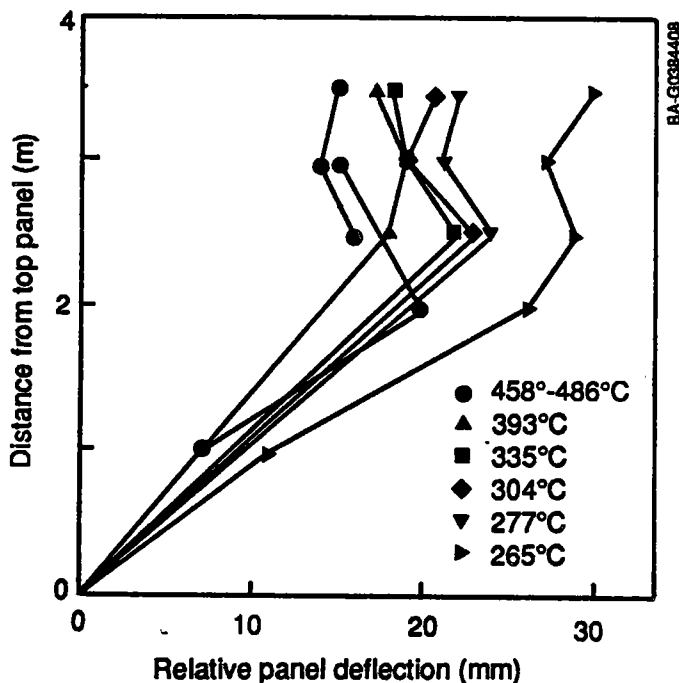
Figure 3-5. Support surface distortion as a function of salt temperature
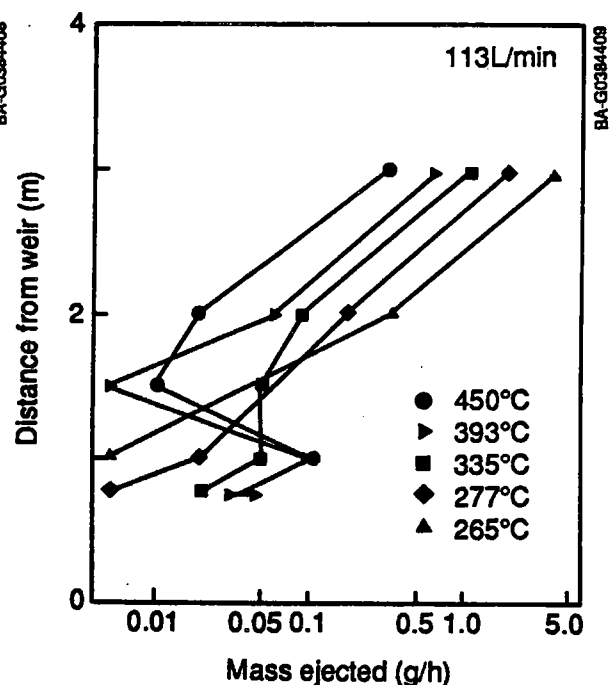
Figure 3-6. Droplet ejection variation with support surface curvature

rate of 113 L/ min. The behavior near the weir was as expected; e.g., increasing salt temperature increased mass ejection rate. Most likely, this was because the less viscous salt at higher temperatures could be ejected from the film more easily. Around 1.5 m from the weir, this relationship inverted; and for 2 and 3 m from the weir, cooler salt exhibited greater ejection rates. Increasing the salt temperature from 265° to 450°C reduced the salt ejection rate by a factor of ten. This behavior can only be explained by the support surface deflection as shown in Figure 3-5 because the salt properties did not change enough to cause an order of magnitude change in ejection rate. For distances less than 1.5 m from the weir, the support surface remained flat or slightly concave. Beyond 1.5 m, the support surface became convex; and in this region the salt ejection increased radically as the convexity increased. These results demonstrate that salt ejection is extremely sensitive to distortions in the support surface and that in a commercial receiver every precaution must be taken to keep the support surface as flat as possible.

3.3 Summary

In this section, we presented measurements of droplet ejection rates from a falling salt film. These data may be summarized as follows:

- A significant quantity of droplets (0.1 g/h for the test support surface width) was ejected from as far as 2 m from the liquid inlet. These increased in size and quantity below this point; and since this was where the waves were developing, we concluded that the droplets were caused by waves and wave growth. The mass of liquid ejected increased exponentially with support surface length to about 1 g/h at 4 m from the weir. Coalescence, overtaking, and the V-shaping phenomenon were more predominant below the 5-m flow length. We expect that these mechanisms will further accelerate droplet ejection below 5 m.

- A very fine mist was emitted from the entire film except just below the liquid inlet. Since film turbulence started about 0.30 m below the liquid inlet and persisted along the entire film length, we concluded that the mist was caused by bursting of turbulent eddies on the film surface. Increased salt viscosity may reduce this tendency.

- Small perturbations in the support surface, e.g., weld beads, can eject significant quantities of salt. On a commercial receiver support surface, these perturbations will need to be ground smooth. Droplet ejection, especially in the wavy regime, is extremely sensitive to perturbations in the support surface. A commercial receiver must be designed to keep the support surface as flat as possible.

- A weir-type salt distributor produced pronounced longitudinal waves that at commercial flow rates ejected large quantities of salt near the weir. It is possible that the salt distributor proposed for a commercial DAR (Chavez, Tyner, and Couch 1988) could also cause such waves. Testing this proposed distribution of high flow rates (800 L/min) is necessary to confirm its performance under realistic conditions.

- Several methods are available for reducing or containing the quantity of droplets ejected including

- using intermediate manifolds at intervals down the support surface to collect and redistribute the salt film, thus preventing wave growth beyond the 3 or 4 m flow length range

- using cavity-type receivers to provide wind shielding and to contain ejected droplets

- using an air curtain to provide cocurrent air flow next to the salt film, thus retarding the growth of waves and containing ejected droplets

- tilting the panel or curving it inward to provide inward force on the waves and to recapture droplets

- adding roughness or film trips to the support surface to retard wave growth.

4.0 FILM BREAKDOWN

4.1 Background

The DAR concept raises new questions regarding the stability of falling liquid films in the presence of high solar flux. The main concern is whether or not the salt film will dry out in the presence of the high solar flux expected in a commercial DAR. This problem, as it relates to the DAR, was first considered by Newell, Wang, and Copeland (1986). They pointed out that since salt surface tension decreases with increasing temperature, a local hot spot on the film would tend to produce a surface shear away from the hot spot. The flow that results from this shear tends to thin the film and causes it to dry out. In addition, if the film temperature at the air/salt interface is less than that at the salt/support surface interface (the situation that results when an undoped liquid film is heated by the surface over which it flowed), Marangoni instability is possible. This instability brings warmer liquid from the support surface to the salt/air interface and reinforces the hot spot.

The literature discusses these phenomena (Davis 1987, for example), but application to operating regimes typical of the DAR is not straightforward. High Reynolds numbers and long flow lengths introduce more complexity, including the presence of well developed roll waves and turbulence in the film. To better understand this film breakdown phenomenon, we undertook experimental research with cooperation from S. Davis at Northwestern University, who modeled the breakdown phenomenon in two phases. In the first phase, he considered the thinning of a horizontal quiescent molten salt film caused by a flux gradient. The results showed that the film would thin about 30% in the presence of the flux gradients expected in a DAR. A second phase considered film breakdown under flow conditions. The objective of the second phase was to determine whether the thinning observed in the quiescent salt film would continue as the film flowed down a support surface and whether it ultimately would lead to film breakdown. Equations developed in the second phase of the work that describe the evolution of the substrate during exposure to flux are presented in Appendix C.

4.2 Experimental Method

To study the film breakdown phenomenon experimentally, we modified the apparatus used to measure film thickness in vertical falling water films (see Section 2.0). Again, safety issues and the simplicity of testing in water led us to begin work with water. The need for testing breakdown of salt films is discussed in Section 4.5. We replaced the Lucite™ tube with a 25.4-mm (outside diameter) stainless steel tube 2.5 m long. We heated the steel tube by passing direct current through it. Current up to 2500 amps produced heat fluxes up to 500 kW/m^2. We controlled the liquid inlet temperature and used deionized water and a mixture of 30% glycerol and water as the test liquids. These two fluids were selected because their physical properties vary significantly (see Table 4-1). In Section 4.3, we show that film breakdown was most sensitive to viscosity, and therefore the 3:1 ratio between the viscosity of these two fluids provided an excellent test. Note also that the viscosity of nitrate salt falls between the extremes of the two test fluids. We determined the liquid flow rate using a turbine flow meter calibrated by the bucket-and-stopwatch method. In determining fluid properties, we used the properties of pure water and the glycerol-water mixture taken at the appropriate temperature (Miner and Dalton 1953). We estimated a total uncertainty in the reported Reynolds numbers of ±2.5%.

Table 4-1. Comparison of Properties of Water and 30% Glycerol/Water (G/W) at Two Temperatures

	Viscosity (cp)	Density (kg/m^3)	Specific Heat (J/kg K)	$d\sigma/dT \times 10^3$ (N/m K)
Water (5°C)	1.4	1003	4178	0.16
30% G/W (5°C)	4.3	1077	3635	0.13
Water (15°C)	1.2	1001	4178	0.16
30% G/W (15°C)	3.5	1075	3635	0.13
Nitrate Salt (420°C)	1.7	1823	1570	0.063

The test procedure involved establishing a fixed inlet flow and temperature and increasing the heat flux slowly in steps until we observed film breakdown. We denoted this flux as the breakdown flux. Repeatability of the breakdown flux was within ±5% of the flux level at a given inlet condition.

We were able to closely observe the actual breakdown of a vertical falling water film by focusing a shuttered video camera at the location of incipient breakdown. The photographs shown in Figure 4-1 depict a typical film breakdown sequence. These photographs were taken of a falling water film at an inlet Reynolds number of 2500 on a 25.4-mm-diameter stainless steel vertical tube. Near the end of the 2.5 m length, each frame shows approximately a 75-mm vertical extent of the tube; the frames are separated by 1/30th of a second and represent an exposure of 1/1000 of a second.

Frame 1 shows several small pockets arranged in a vertical line. These are the sites at which breakdown will begin. Frame 2 shows that the pockets, especially the highest and lowest ones, are more pronounced. The highest pocket in frame 2 appears to have broken and formed dry spots. Frame 3 seems to show less pronounced pockets, especially the highest one. Most likely this was because a roll wave had washed over the substrate and a new substrate had formed. At this Reynolds number, the wave speed was about 2.5 m/s (see Figure 2-6), so the wave would cross the 75-mm vertical distance shown in each frame in about 30 ms or about 1 frame. The substrate exposure time was about 130 ms (see Figure 2-6), so a wave should pass through every 4 or 5 frames. Beginning with frame 4 the pockets begin to become more pronounced, and by frame 6 they have clearly broken and formed dry spots. In frame 7 the spots seem to have agglomerated into three larger dry spots with the top and bottom spots most pronounced. In frames 8 and 9 the liquid between the dry spots appears to thin out, and by frame 15 all the dry spots have agglomerated into one large spot occupying about 3/4 of the vertical extent of the frame.

A roll wave should have passed through the field of view sometime after frame 3 and before frame 15, yet the effect of such a roll wave cannot be clearly seen in the sequence. It seems that once the breakdown has progressed to the stage of pronounced dry spots, such as in frame 4 or 5, the effect of a roll wave is minimal. That is, the dry spots reappear almost immediately after the wave has passed. In frame 15, the effect of a roll wave can be seen as the bow waves on the right side of the dry spots. These waves represent the deflection of liquid in the roll wave around the dry spots.
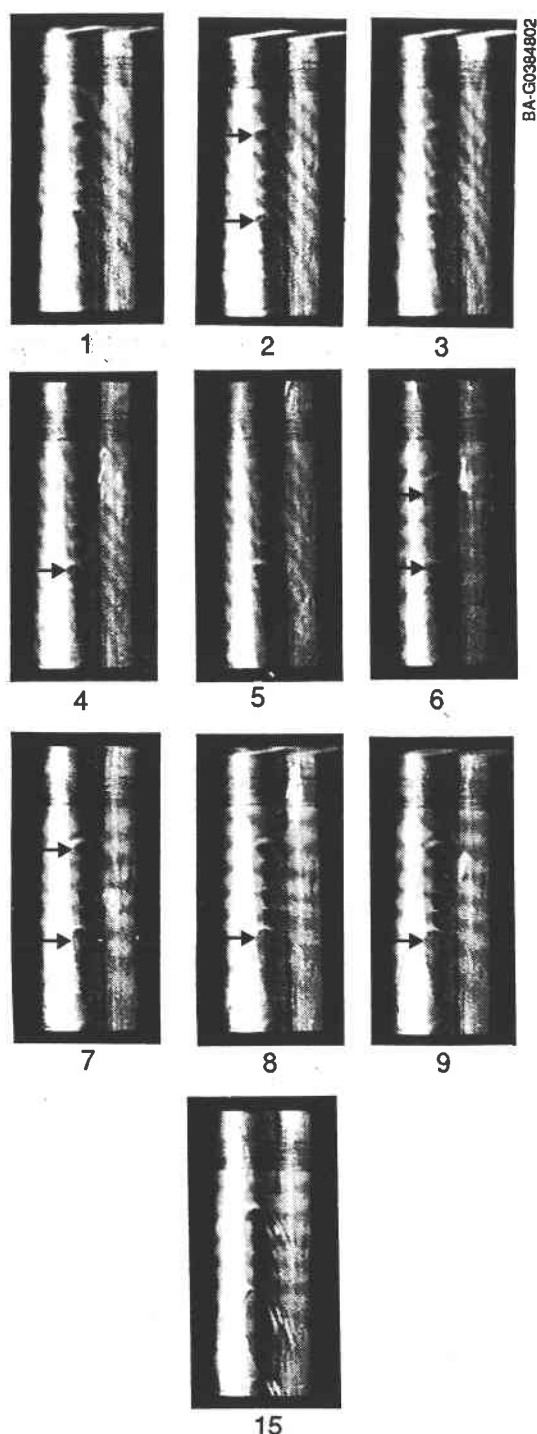
Figure 4-1. **Typical vertical water film breakdown sequence** (arrows point to pockets or dry spots in the film as discussed in the text)

4.3 Development of a Scaling Law for Thermocapillary Breakdown of Falling Liquid Films

To provide guidance to the experiments described in Section 4.2, provide a method for comparing breakdown data with different liquids, and provide a means for predicting the behavior of salt films, we developed a scaling law of thermocapillary breakdown. This law was based on our observations of the breakdown process and what we believe to be the important phenomena involved. After a roll wave passed, a substrate region was suddenly exposed to flux. The mean flow in the substrate was laminar (controlled by a balance between shear stress and gravity) until the Reynolds number of the main film flow exceeded some value (Maron, Brauner, and Dukler 1985). Since the substrate was not perfectly uniform in thickness (see Figure 4-1, frame 1), heat transfer through the substrate produced temperature gradients on the surface. Lateral components of these temperature gradients resulted in a lateral shear stress on the surface because of gradients in surface tension. This shear stress induced a lateral flow that locally thinned the substrate until it broke. Details of the derivation are given in Appendix D.

The results may be summarized by the correlation equation

$$\tilde{q}_B = q_B \ \frac{\gamma}{c} \ \left(\mu^5 \rho g^2\right)^{-1/3} = f(Re) \ ,$$

$$(4\text{-}1)$$

where all properties and the flux are to be evaluated locally.

Equation 4-1 states that if the flux q_B multiplied by the property grouping $(\gamma/c)(\mu^5 \rho g^2)^{-1/3}$ is greater than

a function of the film Reynolds number, breakdown will result. The function f(Re) must be determined experimentally.

Based on Eq. 4-1, we can make the following observations:

- Because $q_B \propto \mu^{5/3}$, a more viscous liquid requires a higher flux to dry out. Because the properties in Eq. 4-1 are to be evaluated at local conditions, we expect that breakdown should first occur at the end of the flow because here the liquid temperature is highest and its viscosity is lowest.

- Because $q_B \propto \rho^{1/3}$, a more dense liquid requires a higher wall flux to produce dryout.

- Because $q_B \propto 1/\gamma$, liquids with a larger surface tension gradient dry out more easily, e.g., with lower wall flux.

We anticipate that Eq. 4-1 should be valid as long as the substrate flow is laminar. When the Reynolds number of the main film flow becomes sufficiently high, it is reasonable to expect that flow in the substrate will become turbulent, as discussed previously. In addition, the substrate may thicken beyond that for the laminar regime. At this point, we would expect that a significantly greater flux than that predicted by Eq. 4-1 would be needed to cause breakdown because turbulent mixing in the substrate will inhibit the organized lateral flow induced by the thermocapillary forces.

This scaling law does not account for interaction between the surface and the liquid, which probably determines the final stage of film rupture and certainly affects rewetting of a dry area of the supporting surface by a roll wave. For example, if the surface of the supporting material is not easily wet by the liquid, then the film will probably break at a lower flux, and the resulting dry area will probably be more resistant to rewetting.

4.4 Results and Discussion

Tests were performed with water and a 30% glycerol and water mixture. To produce high Reynolds numbers, it was necessary to operate with a high liquid flow rate at high inlet temperature. However, these conditions led to breakdown resulting from nucleate boiling rather than thermocapillary forces. They therefore established the upper limit to an achievable Reynolds number of about 7000 with water. The maximum Reynolds number for the glycerol-water mixture was even lower, about 3000.

Results are presented in Figure 4-2. The data for both liquids follow the correlation line:

$$\tilde{q}_B = 1.04 \times 10^{-4} \, Re^{1.34} \tag{4-2}$$

for the range of data $1000 < Re < 7000$.

Bohn et al. (1986) discuss film breakdown for a molten carbonate salt film exposed to concentrated solar flux. The tests described there were not intended to develop quantitative breakdown data. However, it is interesting to cast those data in the dimensionless form of Eq. 4-1 and to compare these with the correlation line, Eq. 4-2. The comparison, shown in Figure 4-2, is surprisingly good considering the conditions under which the carbonate salt data were taken. The carbonate salt data are at low Reynolds numbers so they are not especially useful in determining the validity of Eq. 4-2 for typical DAR operating conditions.
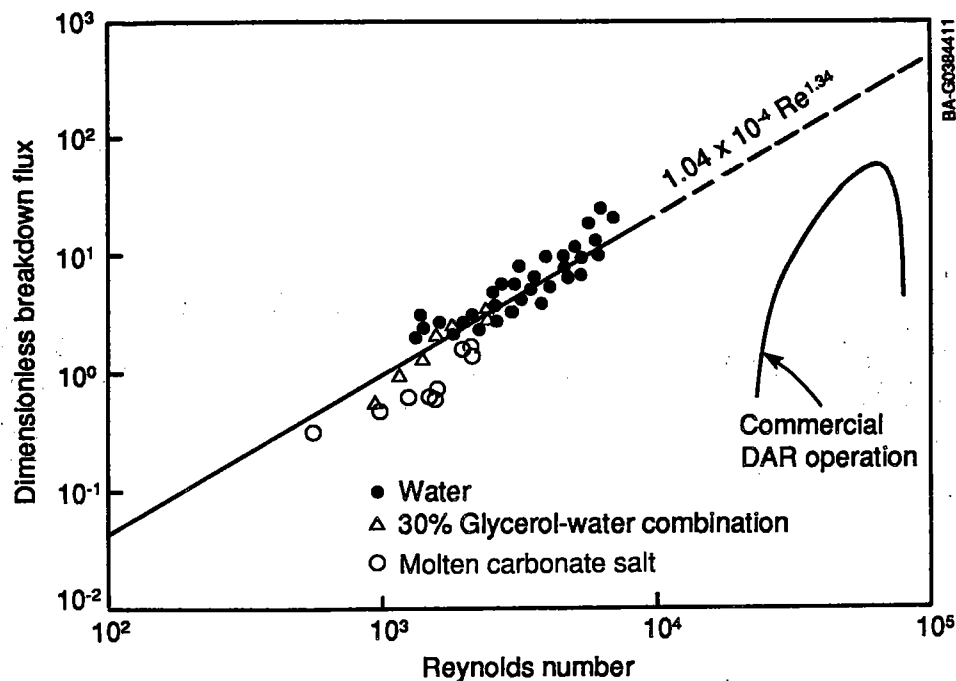
Figure 4-2. Dimensionless correlation of film breakdown
data for water and glycerol/water mixture

Also shown on the graph is the expected operational range of a commercial DAR.
Important operating characteristics of this external, right-circular cylinder
receiver are a salt temperature range of 288° to 566°C, a single-point aiming
strategy producing a peak flux of 1400 kW/m^2 halfway down the flow path, and a
mean flux of about 700 kW/m^2. To produce the curve shown on the right side of
Figure 4-2, the local salt temperatures were predicted from the inlet salt
temperature and the flux distribution. Local salt properties were then deter-
mined. Given the local flux and properties, Eq. 4-1 was used to calculate the
dimensionless flux, and this was plotted against the local Reynolds number
determined from the local properties and the salt flow rate. The receiver
flux expressed in this dimensionless form is low at the salt inlet (receiver
top) because the flux is low and the salt is cool and therefore viscous. As
the salt flows down the support surface, its temperature increases as does the
local flux, causing the dimensionless flux to increase rapidly. After the
receiver flux peak is passed, the dimensionless flux droplets rapidly,
although it stays higher than at the inlet because the viscosity is much
lower.

As long as the expected dimensionless flux of the DAR stays below the correla-
tion line expressed by Eq. 4-2, breakdown should not occur. This appears to
be the case in Figure 4-2, because the largest dimensionless flux expected for
the DAR is about a factor of 5 below the correlation line. However, note that
the data in Figure 4-2 were extrapolated over one order of magnitude in Re
(from 10^4 to 10^5), and therefore predicting behavior at Re = 70,000 from data
taken with Re < 7000 is somewhat tenuous. Further testing at higher Re is
needed. On the other hand, we anticipate that at some Re beyond 7000 the sub-
strate will become turbulent and thicker and the slope on the correlation will
increase, implying an even larger factor safety for the commercial DAR.

4.5 Summary

The heat flux required to cause thermocapillary breakdown of falling, vertical water and water/glycerol films was measured over a range of film Reynolds numbers. A dimensionless scaling law was developed and used to compare the breakdown flux for the two liquids and also for a commercial DAR. Based on an extrapolation of the experimental data into the operating regime for the commercial DAR, it appears that the DAR should be safe from thermocapillary breakdown under normal operating conditions. If the film substrate becomes turbulent at Reynolds numbers less than the DAR operating regime, as expected, the receiver would be even safer. However, the extrapolation of experimental data needs to be confirmed with further experimental data closer to the regime of DAR operation.

5.0 HEAT TRANSFER

5.1 Background

Because the DAR is expected to operate in a high-flux environment, the incident solar radiation in the salt film must be absorbed efficiently to ensure that the support surface is not overheated. Essentially, this means either that the salt must be doped with sufficient darkener to ensure nearly complete absorption of the radiation within the salt film, or if the salt is not doped, that a sufficiently high convective heat-transfer rate exists between the salt and the support surface.

To quantify these requirements, we assume that the peak flux to be absorbed in the salt film is 1400 kW/m^2, that the salt film is 1 mm thick (typical of the substrate region as described in Section 2.0), and that the support surface is to operate at no more than 100°C above the local salt temperature. This means that if the salt is not doped, then a convective heat-transfer coefficient of at least 14,000 W/m^2 °C is needed. If the salt is doped so that 90% of the flux is absorbed directly in the salt film (10% of the flux is absorbed on the support surface), then a convective heat-transfer coefficient of only 140 W/m^2 °C is needed. According to the experimental work of Drotning (1976), adding approximately 0.15 wt % cobalt oxide particles to the salt film would yield this 90% absorption.

Based on operational considerations for a DAR-based central receiver plant, it is clearly preferable to operate it without adding dopant to the salt. However, it is also clear that adding dopant will protect the support surface. This section describes experimental and analytical research aimed at determining how these two heat-transfer mechanisms will perform in practice and aimed at providing information that could be used to decide whether adding dopant to the salt is required.

Previous work on the heat transfer between the molten salt film and the support surface was limited to Reynolds numbers of about 5000 and exhibited heat-transfer behavior typical of a laminar falling liquid film (Bohn 1987). Figure 5-1 depicts these data as solid squares. The figure compares our experimental data for carbonate salts with a laminar model of Seban and Faghri (1976) and with the turbulent correlations of Wilke (1962) and McAdams, Drew, and Bays (1940). Wilke's correlations are based on experimental data for heat transfer to vertical, nonboiling falling water, and water/glycol films, 2.4 m long:

$$\frac{h}{k} \left(\frac{\nu^2}{g}\right)^{1/3} = 0.0068 \, Re^{0.433} \, Pr^{0.344} \tag{5-1}$$

$$Re > 3{,}200 \qquad 5 < Pr < 210 \, .$$
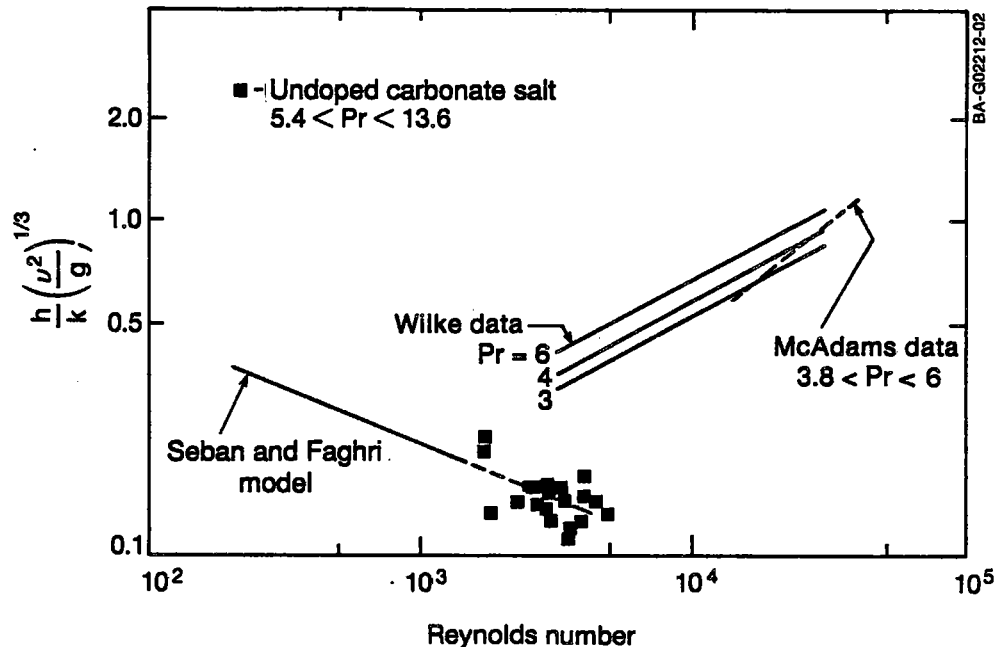
Figure 5-1. Laminar heat-transfer data and models

McAdams' data are for water flow on the inside of a 1.9-m vertical tube. We developed the following correlation from McAdams's dimensional data:

$$\frac{h}{k} \left(\frac{\nu^2}{g}\right)^{1/3} = 0.0092 \ Re^{0.675} \tag{5-2}$$

$$14,000 < Re < 40,000 \qquad 3.8 < Pr < 6.0 \ .$$

Note that even though the carbonate-salt data were for Reynolds numbers well into the turbulent regime, the behavior followed an extrapolation of the laminar correlations shown in the figure. The reason for this is that the support surface used in the tests with the carbonate salt was short enough so that the turbulent film flow could not become fully developed with the relatively viscous carbonate salt.

As a result of the laminar behavior, the heat-transfer coefficients are relatively low, and the support surface operates at excessive temperature for the flux levels described earlier. At the time these experiments were performed, we conjectured that a longer support surface or higher Reynolds number flow would likely result in turbulent behavior with significantly higher heat transfer. In lieu of experimental data verifying that hypothesis, it seemed prudent to assume that the support surface would require protection by doping the molten salt with small particles that were effective absorbers in the solar spectrum.

Our recent testing emphasized the nitrate salts, as discussed in Section 1.0. Major differences between nitrate and carbonate salts are the melting point and the viscosity. The nitrate salt melts at 222°C, and the carbonate salt melts at 397°C. At 500°C the viscosity of the nitrate salt is 1.31 cp (Mar

et al. 1982), and the viscosity of the carbonate salt at the same temperature is 18.0 cp (Ejima et al. 1987). Because the nitrate salt has a much lower viscosity, we did the test at much higher Reynolds numbers, up to 21,000. This greatly increased Reynolds number range provided new insight into the heat-transfer behavior of falling films for the DAR concept.

In this section we present measurements of the heat transfer between a falling nitrate salt film and the support surface at Reynolds numbers between 5400 and 21,000 with varying degrees of doping added to darken the salt. We first describe the experimental apparatus and methods then present the results and compare them with our previous work and work of others. Finally, we draw comparisons and present conclusions about the behavior of the proposed commercial DAR systems.

5.2 Experimental Method

5.2.1 Apparatus

The support surface used in these experiments was 153 mm wide and 803 mm in total length and was fabricated from 41-mm-thick Inconel 600 (see Figure 5-2). The support surface was installed at a slope of 5 deg from vertical. A weir, also 153 mm wide, at the top of the support surface distributed the flow. An inlet manifold behind the weir contained a bed of metal rings that provided an evenly distributed flow across the width of the weir. The support surface was installed in a molten-salt flow loop described in detail in Section 2.0.

Eight sheathed thermocouples were installed in the support surface to measure its temperature. These thermocouples were inserted into holes in the back of the support surface to within 3 mm of the front surface. The support surface was insulated with a 150-mm blanket of mineral wool on the back and sides. Sheathed thermocouples were also placed directly in the flowing salt in both the inlet and outlet manifolds of the support surface to measure salt inlet and outlet temperatures. Cartridge heaters imbedded in the support surface were used to preheat the surface for experiments. These heaters were turned off while data were being taken.

An array of 42 quartz halogen lamps supplied radiant energy to the support surface. The lamps, rated at 6-kW input power each, were mounted on a water-cooled plate that measured 254 mm by 914 mm. A 3-mm-thick quartz plate in front of the lamps provided a plenum for cooling the air around the lamps. Four water-cooled polished aluminum reflector panels were mounted on the array to create a 152-mm by 610-mm aperture for the radiant energy. During experiments, this aperture was positioned directly in front of the salt film to illuminate the full width of the support surface and a length of 610 mm, which we call the active zone. The lamp array could produce fluxes up to 600 kW/m^2 incident on the salt film. The top of the active zone, x=0, was located approximately 0.2 m below the salt inlet point (the weir).

One of the potential deficiencies of using an array of lamps to simulate sunlight is that a substantial fraction of energy produced is in the infrared wavelengths. Sunlight has an effective blackbody temperature of 5300 K, but the lamps used in the lamp array operate with a filament temperature of 2300 K at full power. The lowest power level used during the experiments was one-third of full power, which gives an estimated filament temperature of 1750 K. At 1750 K the maximum blackbody monochromatic emissive power occurs at 1.66 μm
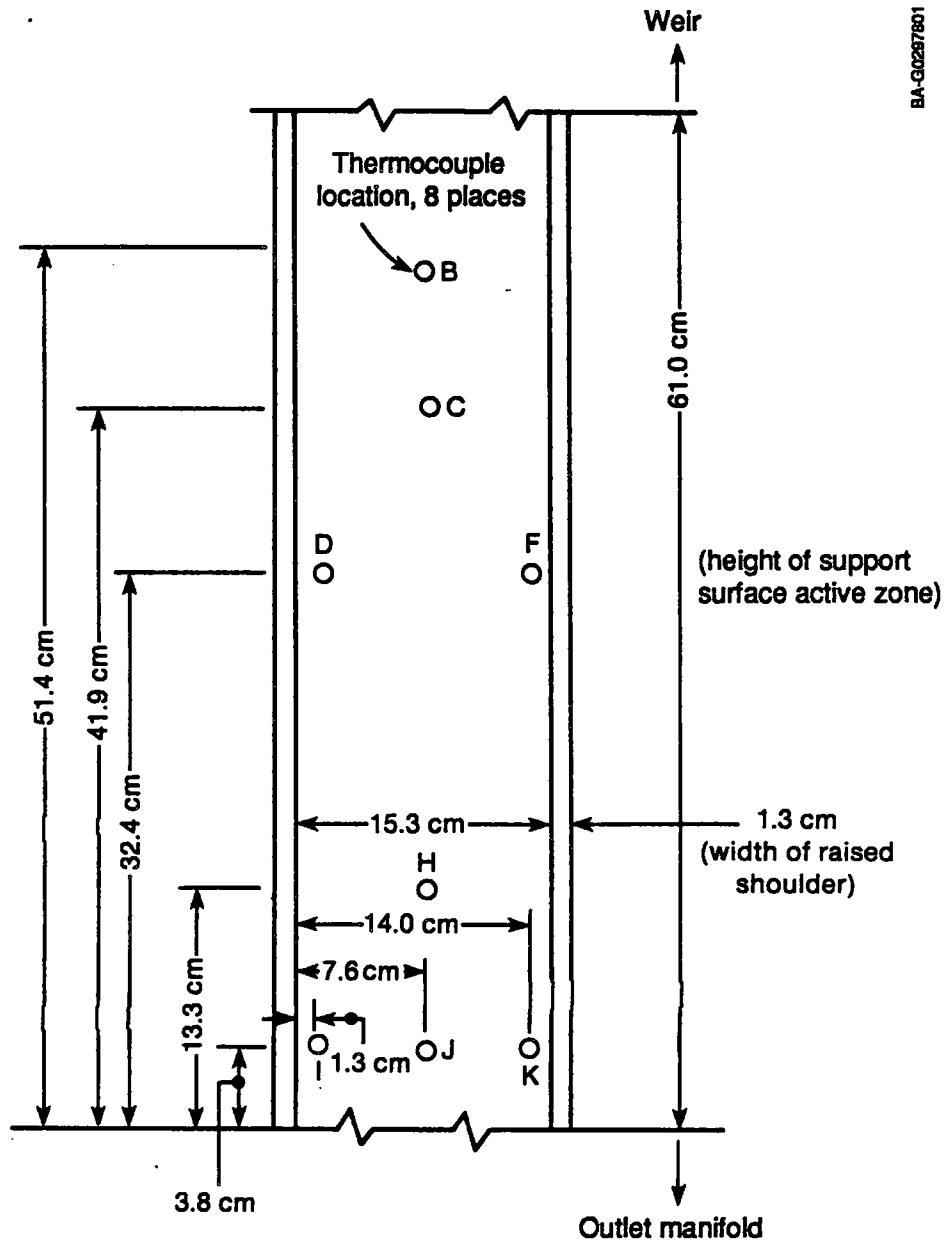
Figure 5-2. Support surface active zone and thermocouple locations

compared with 0.55 µm for 5300 K for sunlight. However, standard infrared spectra for both sodium nitrate and potassium nitrate indicate an absorption band near 7.3 µm with very little additional absorption down to 2.5 µm (Stadtler 1965). In addition, these salts have no absorption bands in the visible wavelengths or the near infrared wavelengths up to 2.5 µm. For the lamp filament at 1750 K, 94% of the blackbody radiation is at wavelengths less than 6.5 µm. At 2300 K 97% of the energy is at wavelengths less than 6.5 µm. In addition, the quartz halogen lamps and the quartz plate in front of the lamps have limited transmissivity beyond 5 µm. Thus, the nitrate salts are transparent to essentially all of the energy incident from the radiant heater.

The result is that the response of the undoped molten salt to radiation from the lamp array is the same as to solar wavelengths. However, we expect that the doped salt will absorb less of the artificial flux than of the solar flux. This is based on the data of Drotning (1976), who measured the monochromatic hemispherical transmission of a specular beam through a 6.9-mm-thick nitrate salt film doped with 0.03% cobalt oxide. (Drotning reported dopant concentration as wt % of cobalt nitrate added to the salt to form cobalt oxide particles. The percentage of 0.03% cobalt oxide was calculated from Drotning's reported values of cobalt nitrate concentration). Drotning's data show that the film transmission is much greater at 1.66 µm (the typical peak wavelength of our quartz-halogen lamps) than in solar wavelengths. He found approximately 50% hemispherical transmission at 1.66 µm and 5% at 0.6 µm. Therefore, we anticipate that any increase in absorption as a result of doping, indicated by data taken with our quartz-halogen lamps, will be significantly smaller than what one would expect with solar wavelengths.

5.2.2 Flux Calibration

We permanently mounted a flux transducer manufactured and calibrated by Hy-Cal Engineering in one of the water-cooled reflector panels of the lamp array. The output of this transducer was calibrated against the lamp array total flux at the array aperture. The calibration was done with an array of six additional flux transducers mounted in a separate movable water-cooled panel. We sized this calibration panel exactly like the molten salt support surface with the six transducers mounted in a horizontal line flush with where the support surface would ordinarily be located. The lamp array aperture was positioned directly in front of this calibration panel and was raised and lowered as needed to map the flux over the entire aperture.

Calibration data were obtained at 11 locations at 51-mm intervals along the height of the aperture. A weighted mean flux at each height was calculated with the weighting determined by the relative horizontal spacing of the six transducers. A fourth-order polynomial curve was used to give a best fit of the mean flux as a function of height. This fit was done at constant lamp array power, i.e., a constant reading from the reflector-mounted transducer. Other power levels were predicted to vary in proportion to the reading from the reflector-mounted transducer. This prediction was in good agreement with data at other power levels. Finally, the expression for mean flux as a function of height was integrated over the aperture area to obtain cumulative energy as a function of height and total energy passing through the aperture. These two quantities were needed to determine the local bulk salt temperature on the support surface.

The lamp array flux was calibrated twice, before and after the heat-transfer data were obtained. The polynomial expression for mean flux as a function of height was obtained from the first calibration data set. The data from the second calibration fell within the scatter of the first calibration. Figure 5-3 shows typical data at a fixed power level from both calibrations along with the derived curve.
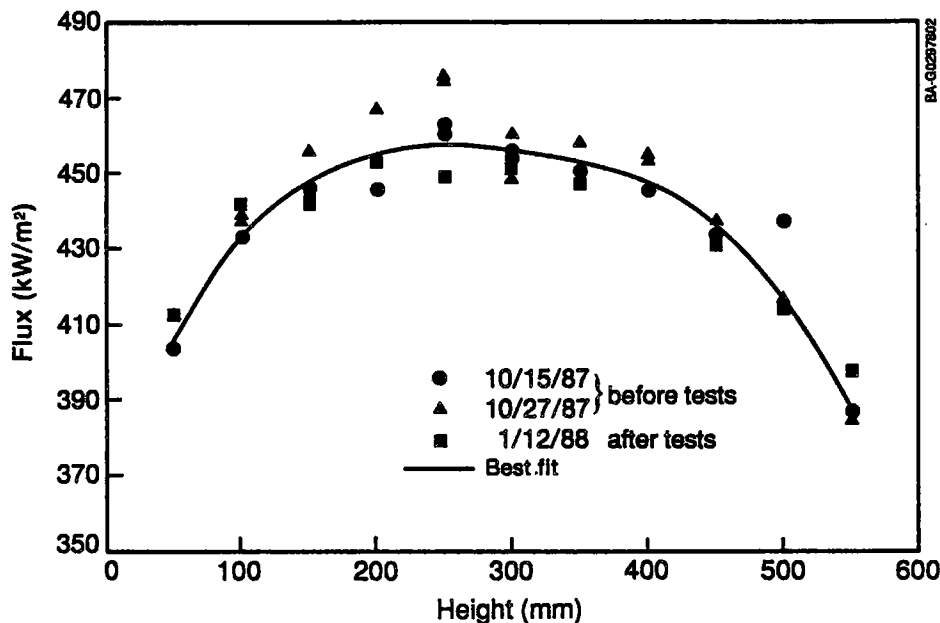
Figure 5-3. Typical flux profile from lamp array

5.2.3 Dopant

Powdered cobalt oxide was used to dope the salt to increase its absorption of radiant energy. The oxide was obtained from Hall Chemical Co. and had a specification of 70%-71% cobalt (nominally Co_3O_4). Particle size ranged from 15 to 100 μm with 78% of the particles by mass falling between 25 and 44 μm. To add the cobalt oxide to the salt, we poured it into a vent on the top of the salt storage tank. Note that much smaller particles would be used for a commercial receiver to minimize scattering and to maximize absorption of radiant energy (see Section 6.0). Typically, the particles would be prepared in a manner similar to that described by Drotning (1976).

Salt samples were obtained directly from the support surface during experiments and allowed to freeze. The samples were later ground up and remixed to avoid errors caused by the cobalt oxide settling during sample solidification. An atomic absorption technique was used to analyze the samples for total wt % cobalt. From these results, the concentration of dopant was derived for each sample as the wt % of cobalt oxide in the molten salt. These concentrations ranged from near zero to 0.257%.

We found that the dopant tended to settle out on the bottom of the tank within minutes. The mixing action of the pump and the liquid return to the tank would keep no more than about 5% of the cobalt oxide in suspension. Passing air through a tube inserted into the tank was effective in resuspending additional dopant. However, this technique was restricted by the tank design, which allowed only limited access to the bottom of the tank. Typically, the dopant suspended in the salt during experiments was only 5%-20% of the total quantity of dopant added, although we did obtain one data point with 47% of the added dopant in suspension. This rapid settling is undoubtedly related to the relatively large particle size. However, even for much smaller particles and for a commercial system with very large storage tanks and long storage tank residence times, similar problems with dopant settling may occur.

5.2.4 Data Acquisition and Analysis

The data recorded during experiments included the molten salt flow rate, lamp array flux at the reflector-mounted transducer, the inlet and outlet salt temperatures, and the support surface temperatures.

The molten salt flow rate was recorded as a volumetric flow rate Q from which the film mass flow rate per unit width Γ was determined:

$$\Gamma = \rho Q / W \ . \tag{5-3}$$

The Reynolds number was then calculated based on inlet salt temperature:

$$Re = 4\Gamma/\mu \ . \tag{5-4}$$

Measurements of the inlet and outlet salt temperatures and of the lamp array flux were used to infer salt temperature as a function of distance down the support surface. The lamp array flux was determined from the measured flux at the reflector-mounted transducer by the calibration procedure described previously. The inlet and outlet salt temperatures were assumed to be the salt temperatures at the top and bottom of the active zone, that portion of the support surface illuminated by the lamp array. The intermediate salt temperatures in the active zone were assumed to be proportional to the cumulative fraction of the total radiant energy absorbed at each height:

$$T_s(x) = \left(\int_0^x q'' \, dx \Big/ \int_0^L q'' \, dx\right)(T_0 - T_i) + T_i \ , \tag{5-5}$$

where x is the position on the support surface; x = 0 at the top of the active zone and x = L = 0.61 m at the bottom of the active zone. ·

The absorbed flux $q''(x)$ was determined from the measured incident flux $q_i''(x)$ by multiplying $q_i''(x)$ by 0.94 to account for reflection and reradiation losses from the salt and support surface. This fraction, 0.94, represents a typical value given a transparent salt with an index of refraction equal to 1.4 and a support surface hemispherical reflectance of 0.1. A more detailed discussion of this loss is presented in Section 5.3. Note from Eq. 5-5 that $T_s(x)$ is actually not sensitive to this estimate of reflective losses, which are accounted for in our measurement of $T_0 - T_i$.

We measured the support surface temperatures at several heights in the active zone, as described previously. A salt temperature was calculated at each of those heights, and the salt/support surface temperature difference ΔT was found for each location. The absorbed flux q" at that location was also determined from the flux curve fit and the fixed flux transducer. We then determined a local heat-transfer coefficient h:

$$h = q''/\Delta T \ . \tag{5-6}$$

The heat-transfer coefficient increased from the top of the active zone to about x = 0.2 m and then decreased slowly over the remainder of the support surface. This implied that the salt film was thermally developed near the end of the support surface length. This developed value of h was used in

subsequent data presentation as being representative of an average value of h along a full length (commercial) support surface.

Data were obtained with both clear and doped salt. The effect of dopant was to reduce the flux transmitted through the salt and absorbed on the support surface. This, in turn, reduced the measured salt/support surface temperature difference ΔT. The measured flux was not influenced by the presence of dopant in the salt since the film reflectance does not change when dopant is added. The net effect was to increase the calculated salt/support surface heat-transfer coefficient h. This is an <u>apparent</u> heat-transfer coefficient because the mechanism is direct absorption in the film as well as convection at the salt/support surface interface. However, this apparent heat-transfer coefficient is still useful for estimating the salt/support surface temperature difference and for comparing it with that of undoped salt.

5.2.5 Uncertainty Analysis

We estimated the uncertainties in our data and the derived quantities using the methods recommended by Abernathy et al. (1980). Where fluid properties are used in the data analysis, we used a 10% uncertainty for thermal conductivity, a 1% uncertainty for density, and a 3% uncertainty for viscosity per Janz et al. (1979).

The uncertainty in the molten salt volumetric flow rate was ±7% at a nominal 27-L/min flow rate. Nominal flow rates varied from 17 to 34 L/min. The resulting uncertainty in the Reynolds Number is ±8%. We considered several potential sources of error when calibrating the lamp array flux. These sources contributed to an ±8% error in the measured mean flux. The dimensionless heat-transfer coefficient has an estimated uncertainty of ±26%, which accounts for the factory calibration and anticipated drift of the flux transducers and variation between thermocouples used to measure temperature differences. The uncertainty in stated wt % of dopant is estimated to be ±0.005%.

5.3 Results and Discussion

Although local heat transfer was not studied in depth, it is worthwhile discussing typical results of local heat-transfer measurements. Figure 5-4 shows the local heat-transfer coefficient for undoped salt plotted as a function of distance from the top of the radiant heater at an inlet Reynolds number of 21,000. Starting near the top, the heat-transfer coefficients increase slightly to a weak maximum, then decrease slightly, and level off at about 0.6 m from the top of the lamp array. The reason for this behavior can be explained with the help of the sketch on the bottom part of Figure 5-4, which shows the results of flow visualization experiments at this Reynolds number. As described in Section 3.2.1, random transient spots of turbulence appear about 0.18 m below the weir, which nearly coincides with the top of the radiant heater. At approximately 0.2 m below the top of the radiant heater, or 0.38 m from the weir, the turbulent spots are fairly pervasive over the entire film. The increase in local heat transfer seen in Figure 5-4 near the top of the heater is most likely because turbulent flow developed in the range of 0 to 0.38 m from the top of the radiant heater. As the turbulent flow begins to develop, the thermal boundary layer becomes thicker and the local heat transfer decreases slightly to the value seen on the right side of Figure 5-4. We took this value as the developed heat-transfer coefficient and use it to compare with previous measurements.
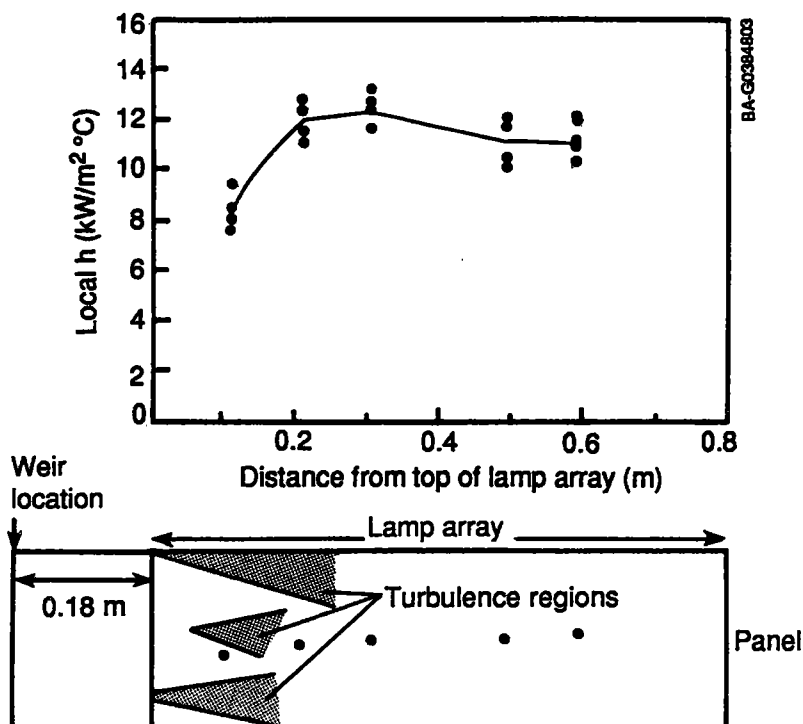
Figure 5-4. Local heat-transfer coefficient

Figure 5-5 shows the most likely behavior of local heat transfer if the heat input to the film started at the liquid distributor. Referring to the three zones depicted in the figure, zone A is the region of developing laminar flow. The liquid is distributed at uniform temperature onto the support surface, and so the thermal boundary layer is essentially of zero thickness. As a result, the local heat-transfer coefficient is very high. As the thermal boundary layer thickens, the local heat-transfer coefficient decreases, zone A, until turbulent spots begin to appear at the start of zone B. Moving downstream in zone B, the turbulent spots are longer lived and act to increase local heat transfer by turbulent mixing. By the start of zone C, the support surface is fully covered all the time with turbulent spots, and the turbulent boundary
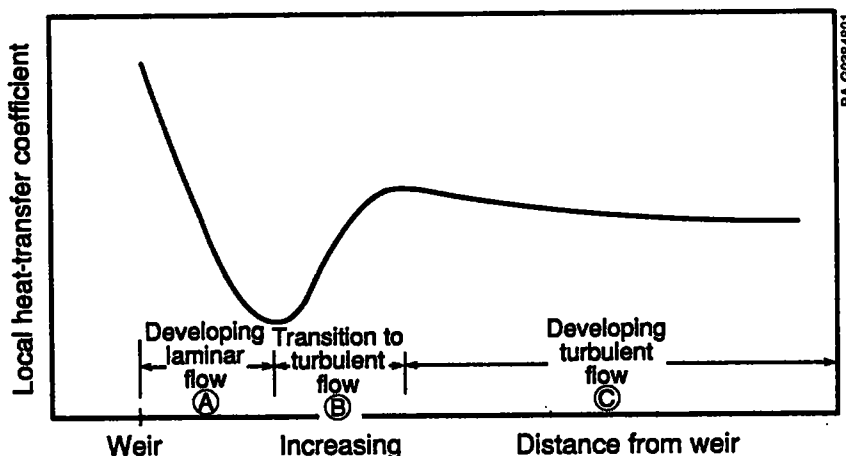
Figure 5-5.   Heat-transfer behavior of a DAR near
             the salt distribution

layer begins to develop, causing the local heat transfer to decrease slightly throughout zone C.

If the liquid distributor for a commercial DAR is to be placed in a region of substantial flux, then the preceding ideas could be used to determine if thermal stresses will be a problem near the distributor. If the gradient of local heat transfer is too large near the weir, then the support surface temperature gradient will be too large, and excessive thermal stresses may result and damage the support surface. If this is the case, then dopant may need to be added to minimize dependence on convective heat transfer.

Data for the nitrate salt tests are presented in Figure 5-6. The range of parameters tested includes Reynolds numbers from 5000 to 21,500 and dopant levels from zero to 0.257 wt % cobalt oxide. The Prandtl number varied from 3.2 to 4.9 during the tests, although it was not varied as an independent parameter. As Figure 5-6 demonstrates, the average heat-transfer coefficient data for no dopant (<0.005% by weight) follow very closely the data correlation of Wilke (1962) for Prandtl numbers in the 3-6 range. For the 24 data points with no dopant, the standard deviation from Wilke's correlation is 8.4%. Agreement with McAdams, Drew, and Bays (1940) data is also quite good; the standard deviation is 5% over the applicable range of that correlation. The two data points at a Reynolds number of about 5400 appear to fall in the transition region between the laminar data for the carbonate salt and the turbulent correlations. The substantial reduction in heat transfer as the film becomes laminar corresponds to a turndown of about 4:1 for a commercial plant. It is possible that a commercial plant may operate at such a turndown, e.g., under low-insolation conditions, and therefore caution would be needed to prevent support surface burnout.
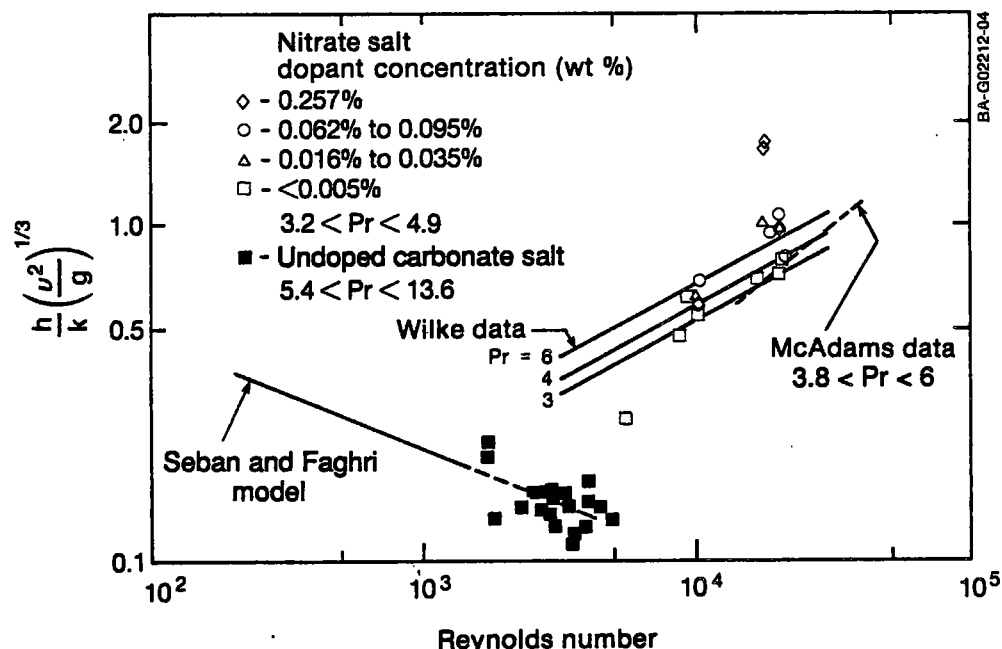
Figure 5-6. Heat-transfer data for doped and undoped molten salts

The presence of the roll waves could affect salt-to-support surface heat transfer. However, since Wilke's data were for a 2.4-m-long film and McAdams data were for a film nearly as long and were for high Reynolds numbers, we expect that their correlations are representative of wavy films. It is possible that the behavior observed in Figure 2-5, in which the substrate becomes very short, occurs only for flow lengths beyond those tested by Wilke or McAdams. If so, it is possible that this phenomenon could further increase heat transfer for long, high Reynolds number films beyond that predicted by Wilke's data or McAdam's data. If this is the case, then it appears that we can use the turbulent film correlations to conservatively predict molten nitrate salt DAR film heat transfer over the entire flow length, except perhaps for the first 0.5 m.

As the dopant level is increased (see Figure 5-6), the apparent heat-transfer coefficient increases, although only at 0.25 wt % is the increase significant. At this doping level, the apparent heat-transfer coefficient is increased by about 2.4 times the undoped values. The turbulent film thickness correlation of Takahama and Kato (1980)

$$\bar{\delta} = 0.228 \ (\frac{\nu^2}{g})^{1/3} \ \text{Re}^{0.526} \tag{5-7}$$

(verified for water films at high Reynolds numbers [see Section 2.2.1]) yields a mean film thickness of 1.4 mm at Re = 17,700 and a 475°C salt temperature. From the apparent increase in heat-transfer coefficient, we find that the optical extinction coefficient of 631 m^{-1} results from the addition of dopant. Drotning's (1976) data suggest that an optical extinction of 5000 m^{-1} should result with smaller particles and shorter wavelengths, which would be typical of a commercial receiver. Thus, we expect that with a commercial receiver the absorption would be increased significantly.

Because the heat-transfer coefficients with the undoped salt in the turbulent regime are much higher than our previous data in the laminar regime, we chose to determine how a commercial DAR would behave thermally if the salt were not doped and turbulent flow were maintained. In particular, we were interested in determining the local salt and support surface temperatures as a function of distance down the support surface. Based on the excellent agreement of the undoped nitrate salt heat-transfer data with published turbulent film heat-transfer correlations, we used those correlations to predict heat transfer for a commercial DAR. To accomplish this, details of the optimized commercial DAR, as described in Section 5.1, were coupled with the Wilke turbulent film heat-transfer correlation (Eq. 5-1). The two equations expressing the salt temperature profile and the support surface temperature profile as a function of distance down the support surface are:

$$\hat{m}_s C_s \ [T_s(x) - T_s(o)] = W \int_o^x q_i''(x) \ dx \tag{5-8}$$

$$h[T_p(x) - T_s(x)] = q_i''(x) \ . \tag{5-9}$$

This simplified model neglects reflective or reradiative losses from the film and therefore will conservatively predict the salt and support surface temperatures. The use of Wilke's model over the entire flow range neglects the hydrodynamic and thermal entry regions over which the heat-transfer coefficient may be smaller than that predicted from Eq. 5-1. This approximation is acceptable because (1) the salt inlet temperature is well below the maximum allowable, and therefore lower heat-transfer coefficients can be tolerated; (2) the hydrodynamic entry regions are quite short—about 0.5 m is required to fully develop turbulent film flow at Re = 20,000 and it is likely that this region would not be exposed to high flux in a commercial receiver design; and (3) the thermal entry region is only about 0.2 m at Re = 20,000 based on our local heat-transfer data. Finally, we assume that the correlation for average heat transfer can be used to calculate the local heat transfer in this model. Based on the rather large change in property values, this assumption needs to be experimentally verified.

For a given flow length and terminal salt temperatures, we can determine the inlet Reynolds number. Given the flux distribution $q_i''(x)$ specified by Anderson et al. (1987) for this receiver, Eqs. 5-8 and 5-9 were integrated numerically and the results are shown in Figure 5-7. The average flux is 726 kW/m^2, and the peak flux is 1380 kW/m^2. These conditions occur along a vertical line on the north side of the receiver. For a salt inlet temperature of 270°C and an outlet temperature of 570°C, the inlet Reynolds number is 23,000 and the outlet Reynolds number is 78,000. The peak support surface temperature occurs near the flux peak and is 585°C. At the salt outlet the support surface temperature is 573°C. This analysis shows that the entire system, salt and support surface, would operate well below the maximum salt operating temperature. It appears that operating in the turbulent regime produces heat-transfer coefficients high enough that adding a dopant to increase volumetric absorption in the salt film is probably not needed to protect the support surface from overheating.
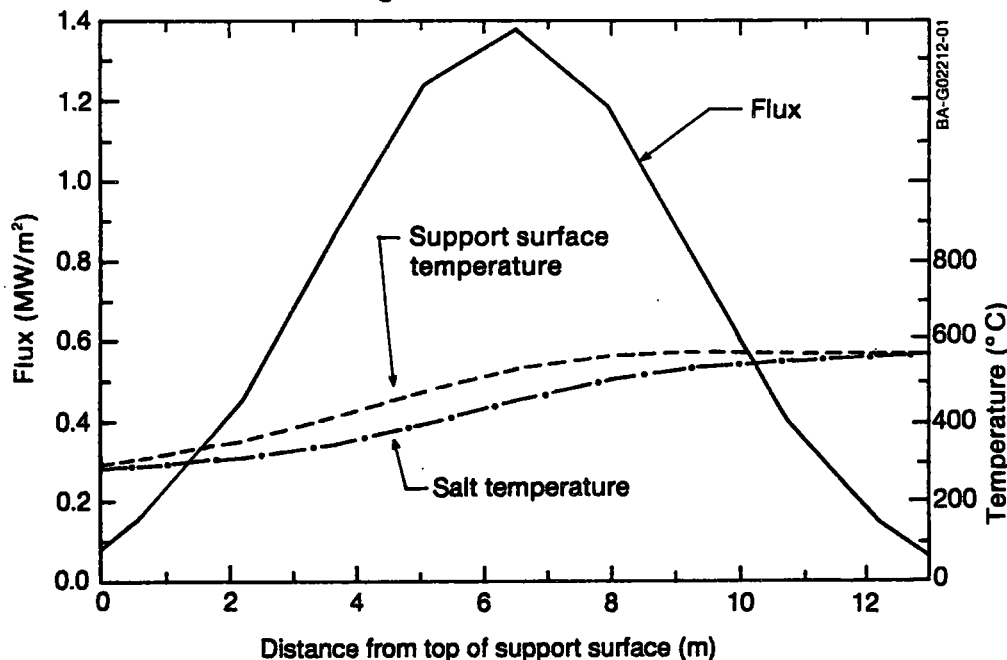
Figure 5-7. Prediction of salt and support surface temperatures for a commercial DAR

If a commercial DAR were to be operated with undoped salt, then we would need to consider how the receiver's optical efficiency is affected. In the case of the doped salt, any solar flux reflected from the support surface would be absorbed, at least partially, in the doped salt film. If the salt film is nominally transparent to the solar flux, additional heat could be lost if flux is reflected from the support surface. In other words, the undoped DAR will be more sensitive to support surface reflectance. Salt-oxidized stainless steel 316 has a hemispherical solar reflectance of 0.10 (Webb 1988). Given this support surface reflectance, we then performed a detailed analysis to quantify this loss mechanism.

The analysis considered an incident specular beam at angles up to 45 deg from the normal. Reflection at the air/salt interface was calculated from the Fresnel equation using an index of refraction of 1.403 for the molten nitrate salt at 420°C (Bloom and Rhodes 1956). This incident specular beam was then allowed to reflect diffusely from the salt/support surface interface with a given hemispherical reflectance of the support surface. We calculated this flux transmission back through the salt/air interface using the Fresnel equation and integrating over the hemisphere centered at the point on the support surface where the solar beam was incident. We determined how much of the incident beam was absorbed given the path length of the beam in the salt film and a specified optical extinction coefficient.

The results indicated that this loss is less sensitive to support surface hemispherical reflectance than might be expected. The reason is that for reflection from the support surface at angles greater than the critical angle (about 45 deg for nitrate salt), total internal reflection will not allow any transmission back out through the salt/air interface. In practice, more than half of the flux reflected from the support surface is trapped in the salt film this way, yielding overall solar reflectance of the salt film/support surface of 0.073 if the support surface hemispherical reflectance is 0.1 and if the salt is totally transparent. This result was quite insensitive to the angle of incident flux: at an incident beam angle of 45 deg, this loss increases to 0.082. Based on the data of Drotning (1976), an optical extinction coefficient of 833 m^{-1} should result from adding 0.042 wt % Co_3O_4 to the salt. This optical extinction coefficient, coupled with a film thickness of 2.4 mm (from Eq. 5-7 at Re = 45,000 and a salt temperature of 450°C), yields an overall film reflectance of 0.029 at normal incidence and 0.037 at 45 deg incidence. These values indicate that the salt is essentially fully dark at 0.042 wt % because these overall reflectances are essentially equal to the reflectance at the air/salt interface.

Based on the cost of cobalt oxide, we estimated that adding this quantity of dopant to the salt would increase the cost of delivered energy by less than 0.2%; and the decrease in overall reflectance would only decrease the cost by 4.4% (0.073-0.029 = 0.044). This relatively small reduction in cost may not justify the added complexity or perceived risks (dopant agglomeration, erosion to salt loop components, etc.) associated with using dopant.

Also note that this analysis of salt film reflection assumes that the waviness of the salt film does not produce large film surface slopes. Film thickness measurements described in Section 2.2.1 for a vertical water film, 4.5 m long at a Reynolds number of 35,000 indicated that the typical peak slope is about 4 deg. The largest slope found in a data set consisting of about 150 roll

waves was 14 deg. Thus, it appears that the assumption of small film slope is justified.

5.4 Summary

Measurements of the heat-transfer coefficient between a falling salt film and the supporting surface indicate that the data are very well represented by turbulent correlations such as those of Wilke (1962) and McAdams, Drew, and Bays (1940). These correlations, in turn, indicate maximum support surface temperatures of 585°C for a typical commercial DAR that heats nitrate salt from 270°C to 570°C. These support surface temperatures are much less than were predicted on the basis of previous laminar heat-transfer data. Although further analyses are needed, it appears that doping the salt to increase its solar absorptance may not be necessary to protect the support surface from overheating. Moreover, adding dopant will only increase receiver efficiency by about 4.4%; therefore, using dopant may not be economically justified either. The data on the doped salt show that if further protection is desired, a relatively low mass loading of cobalt oxide particles, coupled with the high turbulent heat-transfer coefficients, will probably suffice.

6.0 RADIATIVE TRANSFER

6.1 Background

Radiative transfer mechanisms are significant in the operation of a DAR when the salt film is doped. As discussed in Section 5.0, the incident solar flux has to be either absorbed directly within the salt film or onto the oxidized metallic support surface and transferred via convection to the salt film. The following two phenomena contribute to losses and reduce overall DAR efficiency:

• Reflection from the salt-air surface or from the support surface transmitted out through the salt film

• Emission from within the salt film or the back plate transmitted through the film outwards.

If the choice is made to dope the salt film per the trade-offs discussed in Section 5.0, then it is necessary to understand radiative transfer in absorbing, scattering, and emitting media, important characteristics of the doped salt.

6.2 Description of the Radiative Transfer Problem in a DAR

Because the incident solar flux interacts with the dopant particles, the radiative transfer properties of a single particle are important. Also important may be the radiative transfer properties of a cloud of particles since, under some circumstances, a neighboring particle will influence the apparent properties of the single particle (Cartigny 1986). The method of evaluating these properties and the form into which they are cast often depend on each other and on the solution methods selected. We can begin with experimental values for the complex refractive index N, where $N = n + ik$ is a spectral quantity, and calculate radiative coefficients, such as absorption and scattering (e.g., using the Mie theory) as well as transmission and extinction, or we can begin with measuring these radiative coefficients more or less directly. Both approaches have been used and are described here.

Radiative transfer problems in absorbing, scattering, and emitting media are inherently complex. Several factors make up this overall complexity. As already mentioned, particle properties are spectral, requiring, in attempts at somewhat rigorous solutions, keeping track of the spectral distribution of the radiative intensity.

In distinct contrast with radiative transfer among surfaces, which is often the case in many engineering problems, the radiative exchange case discussed here involves absorption, scattering, and emission throughout the bulk of the film as well as absorption, reflection, and emission at the salt-solid interface. Since all of these are directional, this implies that the mathematical formulation of the problem has to consider the directional (spatial) distribution of the radiative intensity.

Emissive power is a strong function of temperature. The solution of the radiative transfer problem typically results in specifying radiation intensity. Temperatures are obtained from simultaneously solving the energy equation.

The emission term in the radiative transfer equation and the radiation term in the energy equation force a strong coupling between these equations.

Also, the receiver geometry and the boundary conditions have to be considered and accounted for. Fortunately, the liquid film in a DAR is thin compared with its length and width. This enables us to greatly simplify the problem just outlined and its solution. Finally, the directional properties of the incoming flux have to be considered.

6.3 Radiative Properties of a Single Cobalt Oxide Particle

Radiative properties relevant here are the absorptivity of the particle and its scattering properties. Scattering is significant because of its directional quality. A particle that exhibits high back-scattering may, when combined with all the other particles, behave similarly to a highly reflecting surface, reducing receiver efficiency.

The Mie theory enables us to calculate both of these properties for a given particle size when we know the spectral complex refractive index (Bohren and Huffman 1983). We also need to assume that the particles are spherical, which is a good assumption particularly when there are numerous particles. An efficient program was used to calculate the ratio between the energy absorbed and the energy scattered by cobalt oxide particles with diameters in the range of 10^{-2} to 10 μm when exposed to the solar spectrum (Bohren and Huffman 1983). The complex refractive index data for cobalt oxide particles used in these calculations are from Tanaka (1979). The index of refraction for nitrate salt was obtained from $n = 1.462 - 1.4 \times 10^{-4}T$ (°C) calculated for a 60% sodium nitrate, 40% potassium nitrate salt (Bloom and Rhodes 1956).

The results are given in Figure 6-1, which shows that although the energy absorbed can be two orders of magnitude higher than that scattered for particles with diameters of 2×10^{-2} μm, particles with diameters ten times larger, 2×10^{-1} μm, absorb only as much as they scatter. This implies that the smaller the particle (below a threshold of approximately 2×10^{-1} μm), the better the absorption. Unfortunately, small cobalt oxide particles tend to agglomerate and, therefore, lose this advantage of small size. Research at SERI indicated that certain additives may inhibit this agglomeration, although compatibility with the salt remains an issue. Finally, note that the smaller the particle, the longer it will stay suspended in the salt, resulting in a more even and stable distribution of particles in the liquid.

The same Bohren and Huffman (1983) program mentioned earlier was used to calculate the phase function for three particle sizes: 0.1, 1, and 10 μm. The phase function specifies the value of scattered radiative flux as a function of direction. The calculation method assumes coherent scattering; i.e., it assumes that scattered radiation retains its frequency. Figure 6-2 is a graph of the results. As shown, a particle with a diameter of 0.1 μm exhibits considerable back-scattering, and particles with diameters of 1 μm and higher exhibit forward-scattering (in the direction of the incoming flux) almost totally. Note that each curve in Figure 6-2 is normalized. Even though small particles exhibit more back scatter relative to forward scatter than do larger particles, Figure 6-1 shows that absorption is much greater than scattering for the small particles.
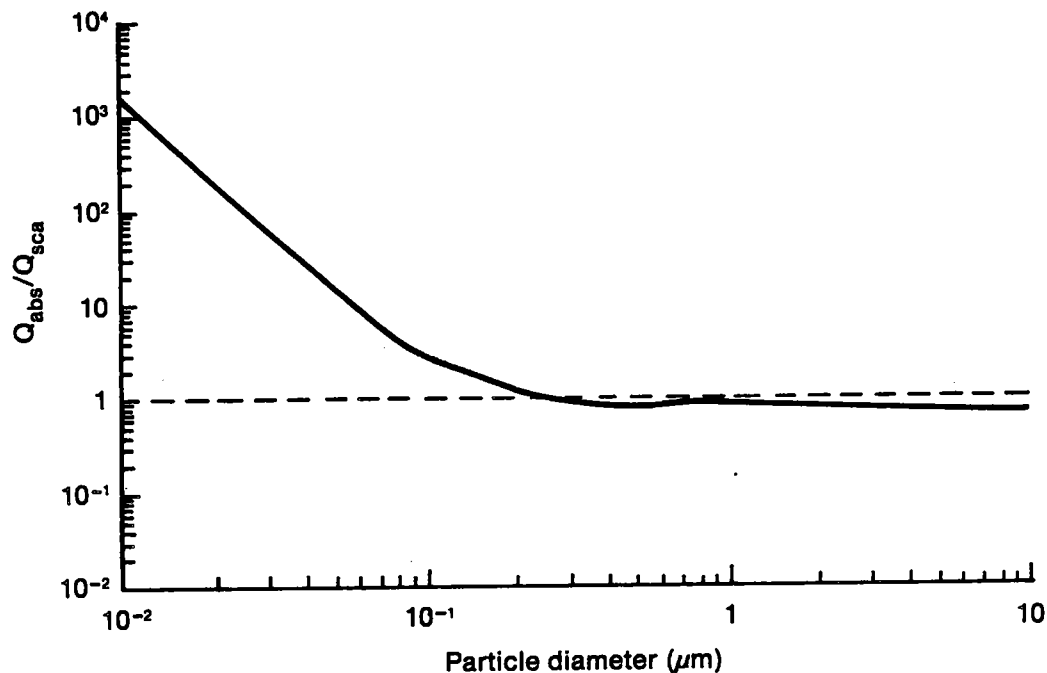
Figure 6-1. Ratio of energy absorbed to energy scattered by a cobalt oxide particle (solar-weighted at air mass 1)
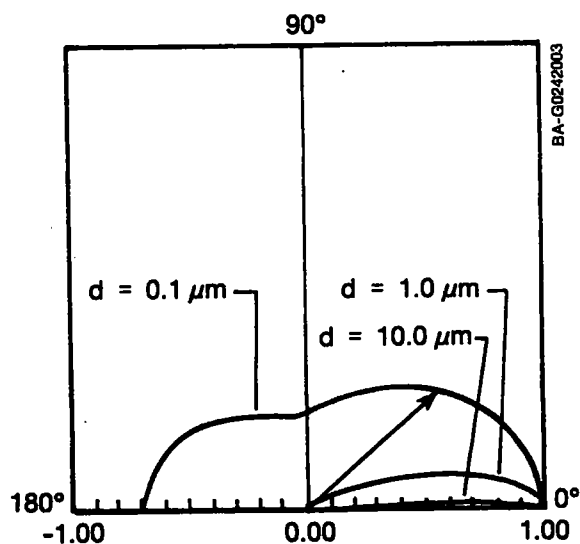
Figure 6-2. Phase function for cobalt oxide spheres (solar-spectrum-weighted scattering for air mass 1). Values are scattered flux in a given direction normalized to the flux scattered in the direction of the incoming flux (0°).

6.4 Transmittance Measurements for Two Salts with Cobalt Oxide Particle Suspensions

Transmittance measurements are useful for comparing different particle suspen-
sions for their ability to absorb the incoming solar radiative flux. Consid-
erable experimental work has been done previously on the transmittance of
solar radiation through a film of salt in which cobalt oxide particles were
suspended. For example, Drotning (1976) measured the transmittance for a
doped eutectic mixture of potassium nitrate, sodium nitrite, and sodium
nitrate. The measurements are of the normal-hemispherical transmission, where
the film is irradiated normally by a collimated beam and where a hemispherical
measurement of the transmitted flux is made on the other side of the film.
From these measurements, Drotning developed an equation to predict the
percentage of incident solar flux absorbed in the salt as a function of film
thickness and dopant concentration. Absorption for several film thicknesses
and dopant concentrations are given in Table 6-1.

More recent measurements using well-dispersed cobalt oxide particles in water
were made as part of the work reported here. Since water and nitrate salts
are both nearly transparent in the solar spectrum, measurements made with
water can be used to approximate the transmittance of the same volumetric con-
centrations of particles in nitrate salts. An equation to predict the solar-
weighted transmittance of a dispersion of cobalt oxide particles in any solar
transparent liquid using these measurements was developed based on these
measurements. Table 6-2 gives a sample of data points calculated using this
equation for comparison with the earlier data given in Table 6-1.

The results are remarkably similar, considering the differences in cobalt
oxide particle size distribution certain to exist between these two sets of
experiments, as well as the degree of dispersion of the particles, which is
difficult to account for in a quantitative way.

6.5 Formulation and Solution of the DAR Radiative Transfer Problem

The key results sought from analyzing the radiative transfer problem are an
estimate of the thermal efficiency of the DAR film and an ability to estimate
the temperature profile in the film and in the support surface.

**Table 6-1. Percentage of Incident Flux
Absorbed in Doped Salt**

Cobalt Oxide Concentration (wt %)	Film Thickness (mm)		
	2	3	4
0.014	34.0	44.3	52.8
0.027	52.3	64.9	73.5
0.054	73.2	83.6	89.4
0.082	83.5	91.1	94.7
0.109	89.2	94.7	97.2

Table 6-2. Solar-Weighted Percent
Absorption Predicted for a
3-mm Salt Film Doped with
Cobalt Oxide Particles

Cobalt Oxide Concentration (wt %)	Absorbed Sunlight[a]
0.014	45.4
0.027	68.0
0.054	87.4
0.082	93.1
0.109	94.7

[a]0.3-1.4 μm

Until recently, the complexity of the solution to the general radiative transfer problem for absorbing and scattering media forced researchers either to use very simple models, to use engineering approximations to estimate the values being sought, or to rely on experimental data for the same. An example of the first is to use the two-flux method of formulating the problem and a numerical method of solution (Wang and Copeland 1984). We obtained engineering approximations relatively easily with an overall energy balance on the film by identifying the assumed major radiative flux terms--reflection at the air/salt interface, transmission through the film, emission within the film, reflection at the solid surface, and reflection at the salt/air interface--and then estimating by analyzing or measuring each of these terms. This approach is sufficient for estimating the thermal efficiency. An estimate of these and the convective heat-transfer coefficient between the salt and the support surface has enabled fairly reliable estimates of the peak temperatures that might be expected in the support surface (see Figure 5-7).

Recently, a powerful but relatively easy method, as compared with other rigorous methods of solving the same problem, was introduced for solving the general equation of radiative transfer for absorbing and scattering media (Kumar, Majumdar, and Tien 1988). This method uses a discrete-ordinate technique to reduce the integrodifferential equation describing the general radiative transfer problem to a system of ordinary differential equations. Unlike conventional solution methods used in the past, the resulting set of coupled, first-order, ordinary differential equations is solved as a two-point boundary value problem using software routines commonly available. A brief history may help provide a context for the significance of the differential-discrete-ordinate method (DDOM) for solving the radiative transfer problem in absorbing, scattering, and emitting media.

Attention to scattering as a phenomenon of significance in radiative transfer is apparently the result of attempts to explain the blue color of the sky, going back to Leonardo da Vinci (Young 1982). However, it was Lord Rayleigh, around 1900, who explained that the blue color of the sky resulted from multiple scattering of sunlight caused by its interaction with oxygen and nitrogen molecules in the atmosphere. Understanding radiative transfer within a participating medium became a concern when industrial furnaces were developed.

This development drew attention in the 1920s to the absorptance and emittance of carbon dioxide and water molecules. In the late 1940s, radiative transfer in a molten glass furnace was used to explain the uniform temperature measured in that furnace.

Early in this century, astrophysicists considered the mathematical form of the equation of transfer and sought a means of solving it (Siegel and Howell 1981). Notable among these early attempts is the so-called two-flux method, otherwise attributable to A. Schuster and K. Schwartzchild who proposed it in 1905 and 1906, respectively (Schuster 1905). This is a one-dimensional approximation. It divides space into two hemispheres, one in the positive direction and one in the negative direction with the origin at the point of interest. It assumes that although the intensity may be different in each of these two directions, the intensity in each hemisphere is isotropic.

The DDOM, first proposed by S. Chandrasekhar (1960), can be seen as a significant extension of the two-flux method. The name "discrete-ordinate" derives from the central point of the method. Rather than the two directions available in the two-flux model, the DDOM can use any number of discrete directions (ordinates) where the intensity can take different values. The six-flux method was devised apparently as a compromise between the accuracy of the DDOM and the convenience of the two-flux model (Siegel and Howell 1981).

Many other approximations have been devised between these two significant contributions up to the present; these will not be reviewed here. The intent of this brief review is simply to trace the major contributions that led to the very recent development of the DDOM used here to predict the radiative transfer in a DAR.

The DAR radiative transfer problem was formulated and solved by C. Tien and S. Kumar, both at the time with the University of California in Berkeley. Details on the formulation of the problem using this method, including the equation of radiative transfer and the energy equation, and the numerical algorithms used in the solution method are described in Appendix E. We next proceed to discuss the application of the DDOM to a specific DAR configuration.

6.6 Application of the Differential-Discrete-Ordinate Method to the Direct Absorption Receiver

A significant result of solving the radiative transfer problem of the DAR is estimating the temperature distribution within the liquid film (and the temperature of the support surface). The temperature profile in the film can be used to study the severity of the thermocapillary effect, which under some circumstances (described in Section 4.0) can result in the salt film thinning and possibly drying out. Also of interest are the maximum expected temperatures in the liquid film, caused by the salt beginning to decompose from a nitrate to a nitrite in the 700°C range, and in the metal support plate, caused by possible corrosion at this and higher temperatures.

From observations of the liquid film flow pattern at Reynolds numbers similar to those expected in a commercial-scale DAR and measurements of the film and wave thickness described in Section 2.0, it is apparent that the worst case situation, where we expect the steepest temperature gradient and the highest

temperatures, is between successive waves when the liquid substrate is exposed to the incoming solar flux. The assumptions corresponding to the worst-case scenario used to calculate the temperature profile in the substrate are the following:

- Near the middle of the DAR support surface, measuring from the top, a wave (with a much higher velocity than the substrate) would just pass the observation point on the support surface

- The wake of the wave would leave behind a liquid film with an average thickness of 1 mm, e.g., the substrate, having a fully developed parabolic velocity profile, with a film Reynolds number of 5000

- Because of mixing in the wave, the fluid in the substrate would initially have a uniform temperature of 427°C (700 K)

- The average time before the next wave passed the same point would be 0.1 s, during which a total length of approximately 110 mm of substrate would be exposed to the solar flux.

A complete set of these data and properties used in the calculations is given in Appendix F.

The DDOM was applied to this case for three cobalt oxide weight fractions in the salt: 0.5%, 0.1%, and 0.05%. Particles were of 0.1 μm in diameter. Results are shown in Figure 6-3, where the temperature in the film is plotted against the dimensionless distance from the air/salt interface. The parameter that changes for the different curves shown is the distance from the wave that just passed (x = 0 is the point where the substrate begins to be exposed to the flux).

Several conclusions may be drawn from observing the temperature profiles given in Figure 6-3. First, as may be expected, the higher the weight fraction of cobalt oxide particles is, the more negative the temperature gradient is, indicating a higher absorption of the incoming flux near the salt/air interface, $y/L = 0$. Consequently, the case where $f_w = 0.5$% results in higher salt temperatures at the salt/air interface. Although this case also results in higher emission losses than the case where the weight fractions are lower and thus lower film efficiency, it tends to enhance stability with regards to Marangoni instabilities (Davis 1988). The case where the weight fraction is 0.1% gives a fairly even temperature profile across the film. This is desirable because it does not enhance thermocapillary film breakdown and keeps the salt and support surface at near isothermal conditions. Finally, the case where the weight concentration of cobalt oxide was reduced to 0.05 resulted in the film being optically thin and, consequently, causing a positive temperature gradient and a peak temperature to occur at the liquid/solid interface. Based on Davis (1988), this lightly doped (or undoped) salt/film is susceptible to Marangoni instabilities because the salt/air interface is cooler than the salt/support surface interface. This instability can lead to film breakdown. However, data presented in Section 4.0 are strong evidence that such instabilities are not important because these data were taken by strongly heating a liquid film at the liquid/support surface interface.
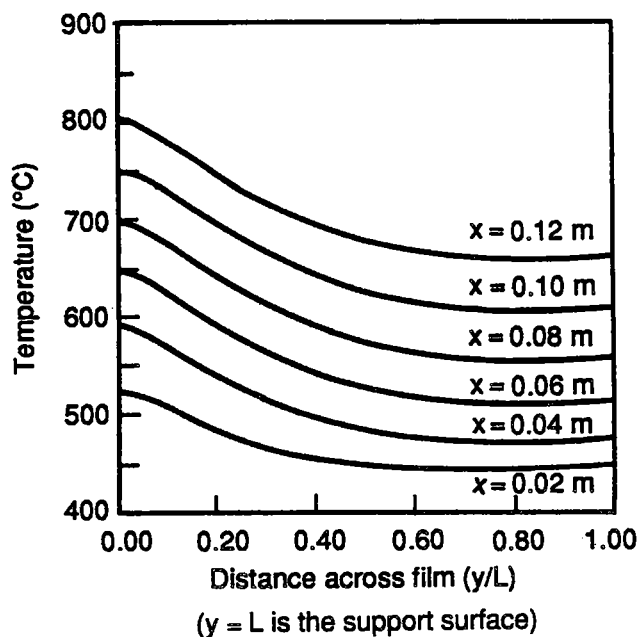
a. Cobalt oxide weight fraction f_w = 0.5%
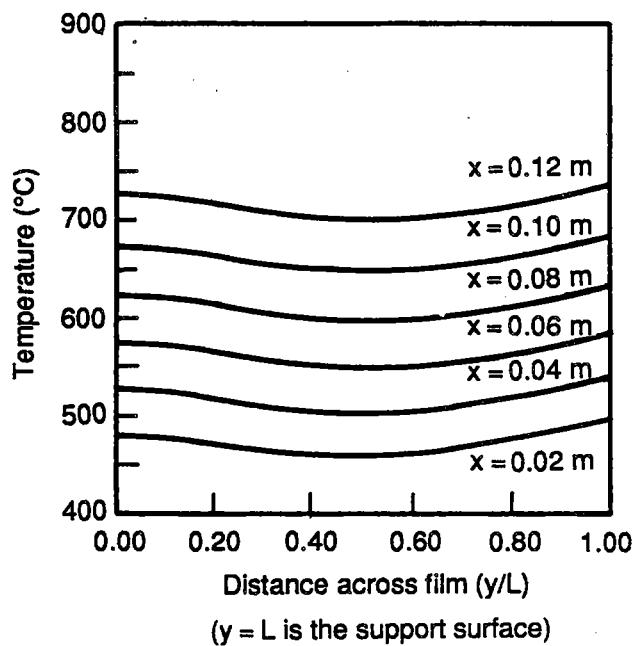
b. Cobalt oxide weight fraction f_w = 0.1%
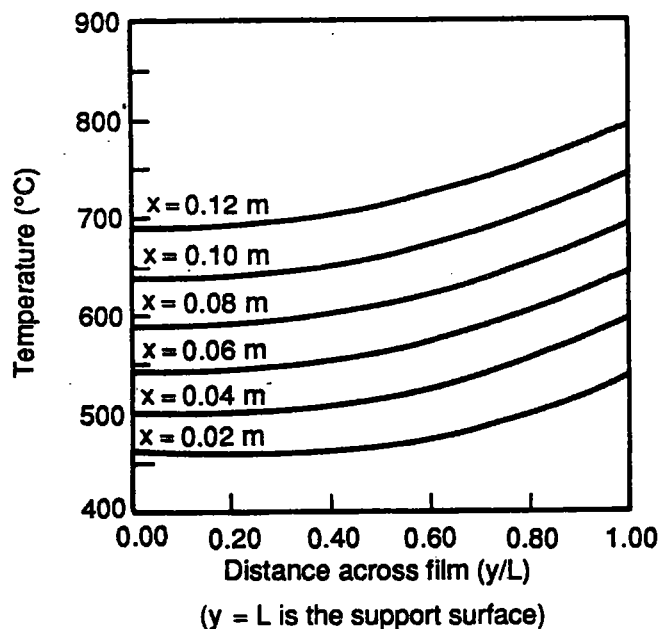
c. Cobalt oxide weight fraction f_w = 0.05%

Figure 6-3. Temperature profiles in the doped molten salt substrate (y/L is dimensionless distance from salt/air interface.)

6.7 Summary

The radiative transfer problem in a doped, nitrate salt DAR was formulated as a general radiative transfer problem in an absorbing, scattering and emitting medium using the DDOM. This problem was simplified considerably because the thin, liquid substrate, the subject of most interest because of its susceptibility to breakdown and overheating, enabled a one-dimensional simplification and solution. The solution indicates that a weight fraction of 0.1% of cobalt oxide particles will result in a nearly isothermal film with a peak temperature near 700°C. Based on these results, we conclude that the DDOM can be used, once it is verified with more detailed experimental data, and combined with the results of the convective heat-transfer data discussed in Section 5.0 for predicting the thermal behavior of the doped DAR film.

7.0 CONCLUSIONS AND RECOMMENDATIONS

This report discusses research accomplishments on several key technical issues associated with the phenomena that underline the DAR concept. It also points out some issues that must be resolved before the DAR concept can be considered a commercial technology. The issues include

- The behavior of wavy liquid films at high Reynolds numbers and long flow lengths

- Ejection of droplets from wavy liquid films

- Thermocapillary dryout of falling liquid films exposed to high flux

- Convective and radiative heat transfer to liquid films exposed to high flux.

In some cases, satisfactory resolution of the issue was reached; in other cases, further research and development is needed to reach the commercial stage. This section summarizes the conclusions of the research on each issue and indicates the need for future research and development on the DAR concept.

We developed experimental techniques that allowed us to measure accurately and reliably the characteristics of water and molten salt films at high Reynolds numbers and for flow lengths long enough to cause waves to develop. Several important characteristics of these wavy films were explored for a falling vertical water film for 6000 < Re < 18000 and for a 4.5-m flow length. These characteristics include wave velocity, mean film thickness, substrate thickness, substrate exposure time, wave peak height, and wave frequency.

We found that as the Reynolds number is increased, the substrate thickness increases substantially and the exposure time (to the high flux) of the substrate decreases substantially. These two findings indicate that the substrate becomes more robust with increasing Reynolds number, probably decreasing the likelihood of film breakdown resulting from exposure to high flux. Measurements of the film thickness in a falling molten salt film verified that the behavior of water films and salt films are quite similar. At a Reynolds number of about 20,000, the film needs to flow approximately 2.5 m before waves develop on the film surface and an additional 1 m before the waves become well developed. At a given flow length, the wave heights grow substantially as the Reynolds number is increased, indicating that wave breaking and droplet ejection is possible.

A way to predict the behavior of wavy falling films is needed. This includes being able to calculate the characteristics (such as the substrate thickness and exposure time) of films in the turbulent regime (as opposed to available laminar models) and wave height as discussed in Section 2.0, particularly for long flow lengths. It also includes being able to predict the development of three-dimensional wave behavior, liquid/gas shear, and other phenomena that lead to droplet ejection. Developing a turbulent wavy film model may require more data similar to that in Section 2.0 but for Reynolds numbers greater than 18,000.

The rate of salt ejection from a molten salt film was measured for flow lengths from 0.5 to 4.5 m and for Reynolds numbers in the range 15,000 to 30,000. Even near the liquid inlet, a significant quantity of salt is ejected

from the surface of the film in the form of very small diameter droplets, less than 0.1 mm in diameter. The data suggest that these droplets originate from the bursting of turbulent eddies on the liquid surface and persist along the entire length of the film.

Ejection of larger droplets begins near the 2.5-m flow length where the wave growth begins. Mass rate of ejection increases exponentially along the flow length from about 0.4 g/h m flow width at 2.5 m flow length to about 4 g/h m flow width at 4 m flow length. Observation of water films longer than 5 m suggests that these rates could increase as wave coalescence, overtaking, and three-dimensional effects (formation of V-shaped waves) become important. A correlation between salt and water droplet ejection rates is needed to allow further quantitative testing with water at longer flow lengths.

Droplet ejection, especially in the wavy regime, was found to be extremely sensitive to perturbations in the support surface, indicating that in a commercial receiver the support surface must be maintained as flat as possible.

High liquid flow rates from a weir-type distributor produce large longitudinal disturbances that eject very large droplets. The lack of test data for any type of salt distributor at high (commercial) flow rates suggests a need for full-scale testing of such distributors.

The droplet ejection problem is clearly a serious issue that must be addressed before the DAR can be recommended for commercial application. It would be desirable to attack the problem from a fundamental approach, which would determine phenomena responsible for droplet ejection and would provide solutions to the problem. However, given limited resources, the most practical approach at this time appears to be to investigate possible "cures" for the droplet ejection problem. First, the problem needs to be quantified; i.e., how much droplet ejection is tolerable from the standpoint of safety, environment, and economics. Once the tolerable amount of droplet ejection is determined, several possible approaches to reaching these limits should be considered, including: air curtains, inward panel curvature, panel treatments such as trips and roughness, intermediate manifolds, and cavity receiver configurations.

We measured the thermocapillary breakdown of vertical falling films of water and glycerol/water mixtures and compared it with a dimensionless scaling law. The scaling law was developed based on a relatively simple scaling between the mean downward flow in the substrate and the lateral flow induced by thermocapillary shear stress at the liquid/gas interface. This scaling law allows us to compare the thermocapillary breakdown of different fluids. Using this scaling law to compare measured breakdown of the two test fluids, which have significantly different physical properties, shows that a single dimensionless equation successfully correlates both data sets. This implies that the behavior of a molten salt film can be predicted with this dimensionless equation, and the sensitivity of a DAR to thermocapillary breakdown therefore can be determined. At this time the most likely method for dealing with the problem is to use air curtains and intermediate manifolds. Testing of such a concept is planned for the second quarter of FY 1990 at the Central Receiver Test Facility, Sandia National Laboratories, Albuquerque.

Because the experimental data were limited to a Reynolds number of about 7000 and a commercial receiver will operate at a Reynolds number of about 70,000, it was necessary to extrapolate the correlation equation about an order of magnitude beyond the available experimental data to predict the behavior of a commercial DAR. This procedure shows that the DAR film should not be susceptible to thermocapillary breakdown; however, additional data at a higher Reynolds number are needed before this statement can be made with confidence. Testing at higher Reynolds numbers (up to about 20,000) is planned for the second quarter of FY 1990 at SERI and near full-scale testing is planned during the third or fourth quarter of FY 1990 at Sandia.

Convection heat transfer was measured at the interface between a 61-cm-long falling salt film and its support surface. We tested both doped and undoped salt. In contrast to earlier tests with a more viscous carbonate salt in which a laminar film resulted, these new tests show that nitrate salt operates in the turbulent regime and produces very high convective heat-transfer coefficients. The experimental data agree very well with previously published correlations for heat transfer in turbulent falling films.

Adding a dopant (cobalt oxide particles) more than doubles the apparent heat-transfer coefficient, although the particles tested were very large compared with those that would be used in practice and are therefore much less effective in absorbing incident radiative flux. Calculations based on the convection heat transfer for an undoped turbulent nitrate salt film show that adding dopant to protect the support surface may not keep the support surface from overheating, but adding dopant will increase the receiver efficiency approximately 4.4% by reducing reflective losses. The benefit of this improvement must be traded off with the increased complexity and potential problems associated with using the dopant in the DAR system.

Films without a dopant need to be tested on a large scale with high solar flux to confirm that a dopant is not needed to protect the support surface under the extreme operating conditions expected in a commercial receiver. Systems studies are needed to quantify the tradeoff between the expected ~4% gain in receiver efficiency resulting from using a dopant and the increased system complexity. The latter requires that the same large-scale solar tests also be carried out with dopant to gain experience in its usage. Such large-scale tests are planned for the third or fourth quarter of FY 1990 at Sandia.

We obtained temperature profiles analytically for the doped molten-salt substrate when it is exposed to the concentrated incident solar flux. These were obtained using the differential-discrete-ordinate method for solving the equations of radiation transport. Results indicate that if a dopant is desired, a rather low weight fraction of cobalt oxide particles in the salt is sufficient to absorb the bulk of the incoming flux and therefore minimize losses.

8.0 REFERENCES

Abernathy, R. B., et al., 1980, Measurement Uncertainty Handbook, revised, Triangle Park, NC: Instrument Society of America.

Abrams, M., 1975, The Solar Absorptance of a Semi-Transparent Layer in an Opaque Substrate, SAND75-8041, Livermore, CA: Sandia National Laboratory.

Abrams, M., 1976, The Temperature Distribution Along an Absorbing-Emitting Fluid Layer Flowing over an Opaque Substrate, SAND76-8622, Livermore, CA: Sandia National Laboratory.

Anderson, J. V., W. Short, T. Wendelin, and N. Weaver, 1987, Direct Absorption Receiver (DAR) Systems Assessment, SERI/TR-253-3162, Golden, CO: Solar Energy Research Institute.

Bloom, H., and D. C. Rhodes, 1956, "Molten Salt Mixtures, Part 2: The Refractive Index of Molten Nitrate Salt Mixtures and the Molar Refractivities," Journal of Physical Chemistry, Vol. 60, pp. 791-793.

Bohn, M. S., 1987, "Experimental Investigation of the Direct Absorption Receiver Concept," Energy, Vol. 12, pp. 227-233.

Bohn, M. S., H. J. Green, G. Yeagle, J. Siebarth, O. D. Asbell, and C. T. Brown, 1986, Direct Absorption Receiver Experiments and Concept Feasibility, SERI/TR-252-2884, Golden, CO: Solar Energy Research Institute.

Bohren, C. F., and D. R. Huffman, 1983, Absorption and Scattering of Light by Small Particles, New York: John Wiley & Sons, pp. 83-180.

Brumleve, T. D., 1974, A High-Temperature Solar Energy System, SAND 74-8008, Albuquerque, NM: Sandia National Laboratories.

Brumleve, T. D., 1978, Status Report on the Direct Absorption Receiver, SAND 78-8702, Albuquerque, NM: Sandia National Laboratories.

Cartigny, J. D., U. Yamada, and C. L. Tien, 1986, "Radiative Transfer with Dependent Scattering by Particles, Parts 1 and 2," Journal of Heat Transfer, Vol. 108, August, pp. 608-618.

Chandrasekhar, S., 1960, Radiative Transfer, New York: Dover Press.

Chavez, J. M., C. E. Tyner, and W. A. Couch, 1988, "Direct Absorption Receiver Flow Experiments," Proceedings, Tenth Annual ASME Solar Energy Engineering Conference, Denver, CO.

Chavez, J. M., C. E. Tyner, and D. K. Johnson, 1989, Water Flow Testing of the Direct Absorption Receiver Concept, SAND-88-3390, Albuquerque, NM: Sandia National Laboratories.

Davis, S. H., 1987, "Thermocapillary Instabilities," Annual Review of Fluid Mechanics, Vol. 19, pp. 403-435.

Drotning, W. D., 1976, <u>Solar Absorption Properties of a High Temperature Direct-Absorbing Heat Transfer Fluid</u>, SAND-76-9104C, Albuquerque, NM: Sandia National Laboratories.

Ejima, T., Y. Sato, T. Yamamura, K. Tamai, M. Hasebe, M. Bohn, and G. Janz, 1987, "Viscosity of the Eutectic Li_2CO_3-Na_2CO_3-K_2CO_3 Melt," <u>Journal of Chemistry and Engineering Data</u>, Vol 32, pp. 180-182.

Ganchev, B., V. M. Kozlov, and V. M. Nikitin, 1975, "An Investigation of the Flow of a Liquid Along the Outer Surface of a Long Vertical Conduit." <u>Tr. Mosk. Vyssh. Tekhn</u>, Vol. 207, pp. 45-61.

National Bureau of Standards, 1979, <u>Physical Properties Data Compilations Relevant to Energy Storage, II. Molten Salts: Data on Single and Multi-Component Salt Systems</u>, NSRDS-NBS 61, Part II, Washington, DC: NBS.

Kumar, S., A. Majumdar, and C. L. Tien, 1988, "The Differential-Discrete-Ordinate Method for Solving the General Equation of Radiative Transfer," presented at the 25th National Heat Transfer Conference, July 24-27, Houston, TX.

Mar, R. W., R. W. Bradshaw, R. W. Carling, S. H. Goods, A. S. Nagelberg, and D. A. Nissen, 1982, <u>Progress Report: Molten Nitrate Salt Technology Development</u>, SAND82-8220, Livermore, CA: Sandia National Laboratories.

Maron, M. M., N. Brauner, and A. Dukler, 1985, "Interfacial Structure of Thin Falling Films: Piecewise Modeling of the Waves," <u>PhysicoChemical Hydrodynamics</u>, Vol. 6, pp. 87-113.

McAdams, W. H., T. B. Drew, and G. S. Bays, Jr., 1940, "Heat Transfer to Falling-Water Films," <u>Transactions of the ASME</u>, October.

Miner, C. S., and N. N. Dalton, eds., 1953, <u>Glycerol</u>, New York: Reinhold Publishing.

Newell, T. A., K. Y. Wang, and R. J. Copeland, 1986, <u>Falling Film Flow Characteristics of the Direct Absorption Receiver</u>, SERI/TR-252-2641, Golden, CO: Solar Energy Research Institute.

Schuster, A., 1905, "Radiation Through a Foggy Atmosphere," <u>Astrophysics Journal</u>, Vol. 21, pp. 1-22.

Seban, R., and A. Faghri, 1976, "Evaporation and Heating with Turbulent Falling Films," <u>Journal of Heat Transfer</u>, Vol. 98, pp. 315-318.

Siegel, Robert, and J. R. Howell, 1981, <u>Thermal Radiation Heat Transfer</u>, Second Ed., New York: Hemisphere Publishing Corp., pp. 431.

Stadtler Research Laboratories, Inc., 1965, "$NaNO_3$ Transmittance Sheet No. Y1475, KNO_3 Transmittance Sheet No. Y1175," <u>Index to Inorganic Spectra, Infrared Grating</u>, Vols. 1-5, Philadelphia, PA: Stadtler Research Laboratories, Inc.

Takahama, H., and S. Kato, 1980, "Longitudinal Flow Characteristics of Vertically Falling Liquid Films Without Concurrent Gas Flow," International Journal of Multiphase Flow, Vol. 6, pp. 203-215.

Tanaka, T., 1979, "Optical Constants of Polycrystalline 3D Transition Metal Oxides in the Wavelength Region 350 to 1200 nm," Japanese Journal of Applied Physics, Vol. 18 (No. 6), June, pp. 1043-1047.

Touloukian, Y. S., ed., 1970, Thermophysical Properties of Matter, Vol. 7, New York: IFI Plenum.

Wang, K. Y., and R. J. Copeland, 1984, "Heat Transfer in a Solar Radiation Absorbing Molten Salt Film Flowing over an Isolated Substrate," ASME paper 84-WA/Sol-22, ASME Winter Annual Meeting, December 9-14, New Orleans, LA.

Webb, B. W., and R. Viskanta, 1985, "Analysis of Heat Transfer and Solar Radiation Absorption in an Irradiated Thin Falling Molten Salt Film," ASME Journal of Solar Energy Engineering, Vol. 107 (No. 2), pp. 113-119.

Webb, John, 1988, Private communication based on tests performed at the Solar Energy Research Institute, Golden, CO.

Wilke, W., 1962, "Heat Transfer at Falling Liquid Films," V.D. I. Forschungsheft, No. 490.

Young, Andrew T., 1982, "Rayleigh Scattering," Physics Today, January, pp. 42-48.

Zabaras, George J., 1985, "Studies of Vertical Annular Gas-Liquid Flows," Ph.D Thesis, University of Houston.

SERI ☀

APPENDIX A

SCHEMATIC FOR CONDUCTIVITY
PROBE CIRCUIT
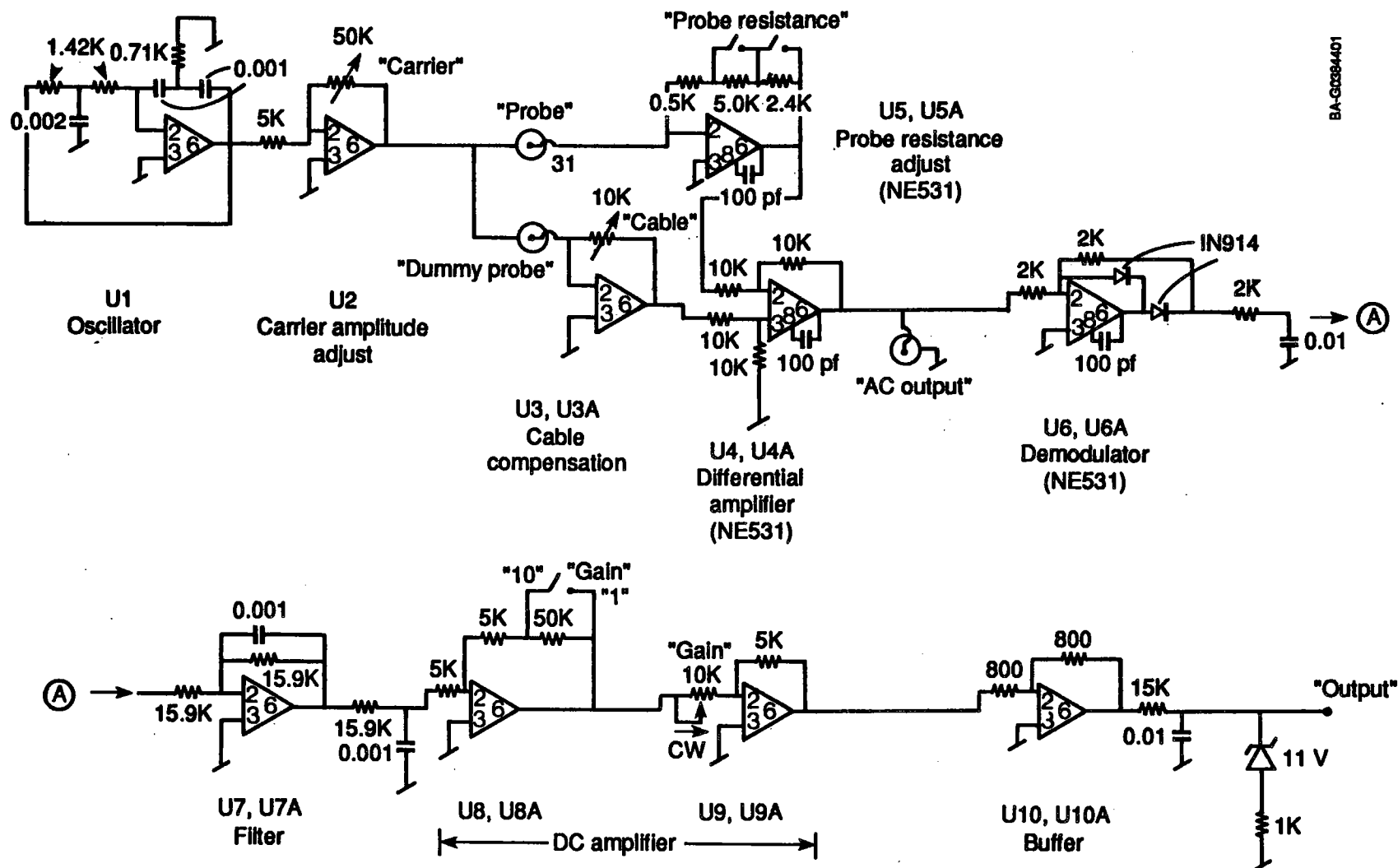
All amplifiers are 741 except NE531 as noted. Pin 4 is -15 V; pin 7 is +15 V.
Quotation marks indicate signals brought out to control panel.

APPENDIX B

COMPUTER PROGRAM USED TO
REDUCE FILM-THICKNESS DATA

Program FILMDATA;

(**;***************
This program plots and reduces data from the conductivity film
thickness probe. It is primarily intended to operate in a batch
mode, e g, it processes several files containing film thickness
data at a given flow condition sequentially.

The following reduced data result from running the program:

1. Wave velocity (mean value for all files)
2. Mean film thickness
3. Mean substrate thickness
4. Mean and standard deviation of the substrate exposure time
5. Mean and standard deviation of the wave peak height
6. Mean wave frequency
7. A plot of the first 1 second of data for each file
8. A histogram of the film thickness data for each file

For a description of the calculation methods, see SERI/TR/253-3438,
Section 2.2.1.

The following shows the format of the input files which contain the data.

For a run in which only probe 1 was sampled:

```
T water              =  23.2
Re (4 gam/mu)        = 17851
gain, offset, Vrefcal =   1.0180   -0.1870      1.00
flow length =  4.50 m.
Vref         =  1.00
probe 1 sampled alone at   1000 hz.
   7000 data points recorded
film thicknesses (mm):
1.19 1.37 1.41 1.58 1.29 1.17 1.04 1.21 1.27 1.12
0.96 0.88 0.87 0.84 1.23 1.22 1.22 1.06 0.98 1.03
1.17 1.22 1.17 1.25 1.12 0.96 1.00 0.98 0.89 0.82
.
.
.
```

and so on for 7000 data points.

For a run in which both probes were sampled:

```
T water              =  22.8
Re (4 gam/mu)        = 17707
gain, offset, Vrefcal =   1.0180   -0.1870      1.00
flow length =  4.50 m.
Vref         =  1.00
both probes sampled
   3500 pairs of data recorded
sampling frequency (probe 1 to probe 2) is   2000 hz.
 film thicknesses (mm):
```

66

```
1.19 1.96 0.91 1.86 1.15 1.55 1.64 1.85 1.43 1.97
1.17 1.71 0.96 1.64 0.98 1.73 1.09 1.54 1.16 1.51
.

.

.
```

and so on for 3500 pairs of data points.

Only data from probe 1 are used to get amplitude-type data.
Probe 2 data are only used to get wave velocity data. Thus, for
the best compromise between good amplitude data and good wave
velocity data, a mix of both single-probe data files and
dual-probe data files are needed.

The format of the file names is important if the batch
mode is to be used. The last two characters before the "."
in the file name should be numerical and should increase
sequentially for all files. For example, for data taken on
August 16, 1988 the first file could be 08168801.DAT, the
second would then be 08168802.DAT and so on. If "DAT" is
not used as the file name extension, it will be changed to
this by the program.

The program was written in Turbo Pascal 3.0 and requires the Turbo
Pascal Graphix Toolbox, also version 3.0. It will successfully
produce hard copies of the graphs only on an Epson printer.

msb 1/3/89

***)


```pascal
label PlotOnly;

const NpointsMax=7000;        {Maximum number of data points allowed
                               for single probe data files}
      NpairsMax=3500;         {Maximum number of data point pairs
                               allowed for dual probe data files}
      hmax=9.0;hmin=0.0;
      form_feed=#$0C;         {Epson form feed control character}
      Npoints_per_line=10;    {in the data files}
      Nbins=100;              {resolution of the histogram}
      wirespace=0.052;        {probe spacing, m}

var   f:real;
      data1,data2:array[1..NpairsMax] of real;
      i,nfiles,Npoints,code,choice,Vwcount:integer;
      printheader,singleprobe,batch,fileflag:boolean;
      Tdatamin,Tdatamax,V1,V2,dT,hmaxdata,gain,offset,Vrefcal,
            Vref,Re:real;
      infile:text;
      firstfile,filename:string[55];
      yn,ynprint:char;
```

67

```
        Resum,Re2sum,Resig,numer,Vwsum,Vw2sum,Vw,Vwsig,hmean,
              hsmax:real;
        bin:array[1..Nbins] of integer;
        hp,hp2,hpmean,hpsig:real;
        Ls,Ls2,Lsmean,Lssig:real;
        Np,Nsubstrate:integer;
        freqw,Runtime:real;


                     (The following are the Graphix Toolbox files needed)
{$I typedef.sys}
{$I graphix.sys}
{$I kernel.sys}
{$I windows.sys}
{$I axis.hgh}
(*
{$Idummy.inc}
*)
{*****************************************************************}
PROCEDURE OpenInFile;    (Opens the data file for processing.  Convert
                          the file name to all upper case letters, and
                          abort if the file does not exist)
var OK:boolean;
    tempname:string[55];
    i:integer;
begin
  repeat
    if not batch then
    begin
      writeln(' enter complete  \path\file name for input data file:');
      readln(filename);
    end; {not batch}
    tempname:='';
    for i:=1 to length(filename) do
      insert(upcase(copy(filename,i,1)),tempname,i);
    filename:=tempname;
    assign(infile,filename);
    {$I-}Reset(Infile){$I+};
    OK:=(IOresult=0);
    if not OK then writeln(' file does not exist');
    if not ok and batch then halt;
  until OK;
end;


{*****************************************************************}
PROCEDURE Calch(var V1,V2:real); (Converts voltage reading into film
                                  thickness, based on the characteristics
                                  of the electronics (gain, offset, etc.)
                                  read in from the data file)
var h1,h2:real;
begin
  h1:=(V1-offset)/(gain*Vref/Vrefcal);
  h2:=(V2-offset)/(gain*Vref/Vrefcal);
  V1:=h1;
  V2:=h2;
end;
```

```
{###############################################################}
PROCEDURE Plot;                  {Produces on the CRT a plot of the film
                                 thickness (or probe voltage) as a function
                                 of time for the data file currently being
                                 processed.  Any subrange of time within
                                 the data file can be specified.  For dual-
                                 probe data files, either or both probes
                                 can be plotted.  For an Epson printer, a
                                 hard copy of the plot can be produced.}


var graphlabel:string[55];
    hpmin,T1,T2:real;
    V1old,V2old,T1old,T2old,Tmin,Tmax,sf1,sf2:real;
    yn,yn1,ynch1,ynch2:char;
    printgraph:boolean;
    i,iend:integer;

begin
graphlabel:=filename+' film thickness, mm';
yn:='y';
while Upcase(yn)='Y' do
begin
  sf1:=1.0;sf2:=1.0;
  Tmax:=Tdatamax;Tmin:=Tdatamin;
    writeln(' select a sub-range of data to plot ?');read(kbd,yn1);writeln;
    if Upcase(yn1)='Y' then
    begin
      writeln(' range of data are from ',Tdatamin:7:4,' to ',Tdatamax:7:4,
            ' sec.');
      write(' input:   Tmin   Tmax ---->');readln(Tmin,Tmax);
      write(' plot ch 1 only ? ');read(kbd,ynch1);writeln;
      write(' plot ch 2 only ? ');read(kbd,ynch2);writeln;
      if upcase(ynch1)='Y' then sf2:=0.0 else sf2:=1.0;
      if upcase(ynch2)='Y' then sf1:=0.0 else sf1:=1.0;
    end;

  T1old:=tmin;T2old:=T1old+dT;
  printgraph:=false;
    write(' print graph ? ');read(kbd,yn1);writeln;
    if Upcase(yn1)='Y' then printgraph:=true;
    write(' press any key to plot data ');read(kbd,yn1);

  InitGraphic;
  ClearScreen;
  SetColorWhite;
  SetBackground(0);
  DefineHeader(1, graphlabel   );
  SetHeaderOn;
  DefineWorld(1,Tmin,hmin,Tmax,hmax);
  SelectWorld(1);
  SelectWindow(1);
  DrawBorder;
  DrawAxis(6,6,0,0,0,0,0,0,false);
  AxisWindow;
```

69

```
Vlold:=data1[1]*sf1;V2old:=data2[1]*sf2;if singleprobe then V2old:=0.0;
if not singleprobe then iend:=Npoints div 2 else iend:=Npoints;
for i:=2 to iend do
begin
  T1:=(i-1)*dT*2.0;T2:=T1+dT;
  if singleprobe then
  begin
    T1:=(i-1)*dT;
    T2:=T1;
    V2:=0.0;
    if i<=iend div 2 then V1:=data1[i] else V1:=data2[i-iend div 2];
  end; {singleprobe}
  if not singleprobe then begin V1:=data1[i];V2:=data2[i];end;
  V1:=V1*sf1;V2:=V2*sf2;
  if (T1>Tmin) and (T1<Tmax) and (T2>Tmin) and (T2<Tmax) then
  begin
    DrawLine(T1old,V1old,T1,V1);
    DrawLine(T2old,V2old,T2,V2);
  end;
    T1old:=T1;T2old:=T2;V1old:=V1;V2old:=V2;
  end;    {i loop}
  Drawline(Tmin,hpmin,Tmax,hpmin);
  if printgraph then hardcopy(false,0);
  repeat until keypressed;
  leavegraphic;
  write(' plot again ? ');read(kbd,yn);
 end; {of yn=Y loop}
end; {of Plot}


{#########################################################################}
PROCEDURE GetVW;        {Cross correlates the data from probe 1 and
                        probe 2 and calculates the wave velocity from
                        the peak in the cross correlation}


var idelaymax,j,k,idelay,delay,Npairs:integer;
    sum,maxsum:real;

begin
  Npairs:=Npoints div 2;
  idelaymax:=100;if Npairs<idelaymax then idelaymax:=Npairs-10;
  maxsum:=0.0;
  for idelay:=0 to idelaymax do
  begin
    sum:=0.0;
    for j:=1 to Npairs-idelaymax do
    begin
      k:=j+idelay;
      sum:=sum+data1[j]*data2[k];
    end; {j}
    if sum>maxsum then
    begin
      maxsum:=sum;
```

```
      delay:=idelay;
    end; (sum)maxsum)
  end; (idelay loop)
  Vw:=wirespace/((delay+0.5)*2/f);
  if delay=idelaymax then Vw:=0.0;
end; (GetVW)


(##################################################################)
PROCEDURE Gethp;          (Locate all peaks in the data file and accumulate
                           peak height, peak height square, and number of
                           peaks)


const mindelt=0.01;  (narrowest permissible wave peak, sec.)
var i,k,j,istart,iend,mindeli:integer;
    thin:boolean;
    hpeakstart,hpeakend:integer;
    dLs,hptemp,hpmin:real;
    substart,subend:integer;
    Wide_peak:boolean;


Function h1(i:integer):real;    (select data from probe 1 based on
                                 whether the data file was for single
                                 probe or for dual probe)
begin
  if not singleprobe then h1:=data1[i];
  if singleprobe then if i<=NpairsMax then h1:=data1[i] else h1:=data2[i-NpairsMax];
end; (h1)


Function IsPeakWide(kstart:integer):boolean;  (determines if an
                                               upcoming wave peak is wide enough)
var k,kmax:integer;
    temp:boolean;
    yn:char;
begin
  kmax:=kstart+mindeli;
  k:=kstart;  (begin at positive crossing of hpmin, scan forward to minimum
               acceptable peak width--if data remains above hpmin and end of
               file is not found, peak is wide enough)

  while (h1(k)>hpmin) and (k<=kmax) and (k<iend) do k:=succ(k);
  if (h1(k)>hpmin) and (k=kmax+1) then IsPeakWide:=true else IsPeakWide:=false;

  (*writeln(lst,'i,k,h1(k),hpmin,i+mindeli,iend:',i:4,k:4,h1(k):6:2,
             hpmin:6:2,kmax:6,iend:6);read(kbd,yn);*)
end; (IsPeakWide)


Procedure Find_SubStart(var k:integer);
var j:integer;
    yn:char;
begin
  j:=i;                        (begin at negative crossing of hpmin, scan forward
                               until cross below hsmax--if cross back up
                               through hpmin or hit end of file, no substrate
```

71

```
                              exists}

  while (h1(j))=hsmax) and (h1(j)<=hpmin) and (j<iend) do j:=succ(j);
  if  h1(j)<hsmax then k:=j else k:=0;
end;  {Find_Substart}


begin
  subend:=1;substart:=1;
  if singleprobe then iend:=Npoints else iend:=Npoints div 2;
  hptemp:=0.0;
  if singleprobe then mindeli:=trunc(mindelt*f) else mindeli:=trunc(mindelt*f/2);
  hpmin:=1.2*hmean;
                        {seek first negative crossing}
  thin:=true;
  i:=0;
  repeat
  begin
    i:=succ(i);
    if h1(i)>=hpmin then thin:=false;
  end; {repeat}
  until (not thin) and (h1(i)<hpmin);
  istart:=i;

  Wide_peak:=false;
  dLs:=0.0;

  for i:=istart to iend do
  begin
    if h1(i)<hpmin then
    begin
      if not thin and Wide_peak then     {just past the negative crossing}
      begin
        Find_SubStart(k);
        substart:=0;
        if k>0 then          {located a real substrate }
        begin
          substart:=k;
          Nsubstrate:=Nsubstrate+1;
        end; {k>0}

                        {previous peak was wide enough to count}
        hpeakend:=i;
        hp:=hp+hptemp;
        hp2:=hp2+hptemp*hptemp;
                    (*
        writeln(lst,' Peak # ',Np:6,' found between i = ',
                hpeakstart:6,' and ',hpeakend:6,' hpeak = ',hptemp:5:2);
                    *)

        hptemp:=0.0;
      end; {not thin}

      thin:=true;
    end;  {<hpmin}
```

72

```
    if h1(i)>=hpmin then
    begin
      if thin then         {just past the positive crossing}
      begin
        Wide_peak:=IsPeakWide(i);  {upcoming peak is wide enough to count}

        if (k>0) and (Wide_peak) then subend:=i-1 else subend:=substart;
                          {last substrate was a real one
                           and upcoming peak is a real one}
        dLs:=(subend-substart)/f;if not singleprobe then dLs:=dLs*2.0;
        Ls:=Ls+dLs;
        Ls2:=Ls2+sqr(dLs);
                    (*
          writeln(lst,'                     Substrate # ',
                Nsubstrate:8,' found between i=',
                substart:6,' and ',subend:6,'  Ls= ',dLs*1000:6:0,' ms.');
                    *)
        hpeakstart:=0;
        if Wide_peak then
        begin
          Np:=Np+1;
          hpeakstart:=i;
        end; {Wide_Peak}
      end; {thin}
      if Wide_Peak and (hptemp<h1(i)) then hptemp:=h1(i);
                          {seek highest point in non-substrate region}
      thin:=false;
    end;   {>hpmin}

  end;  {i loop}


              {check that last crossing is positive going
               if it is not and the previous peak was wide
               (meaning that the present substrate will be counted)
               must remove last contribution to Nsubstrate}

  if (data1[iend]<hpmin) and (k>0) then Nsubstrate:=Nsubstrate-1;

              {if last crossing is positive,
               and peak was wide delete last peak count}

  if (data1[iend]>=hpmin) and Wide_peak then Np:=Np-1;


(*writeln(lst,'data, Ls, Nsubstrate, Np, hp,hs,thin: ',data1[i]:6:3,Ls:6:0,Nsubstrate:6,Np:6,hp:8:3,hs:8:3,thin:8);*)


end; {Gethp}
{########################################################################}
FUNCTION Getk(h:real):integer;{based on a given film thickness, determine
                           in what histogram bin the film thickness falls.}
begin
```

```
      if h<hmax then Getk:=Round(h*Nbins/hmax) else Getk:=Nbins;
end;
{*********************************************************************}
FUNCTION Geth(k:integer):real;{based on a given histogram bin, determine the
                              corresponding film thickness.}
begin
  Geth:=k*hmax/Nbins;
end;
{*********************************************************************}
PROCEDURE Histo;        {From the film thickness histogram for the data
                        file being processed determine the probability
                        density function and integrate up to the peak in the
                        pdf curve to get the mean substrate thickness.  Also
                        reports the mean film thickness, the maximum film
                        thickness and saves the histogram to a file.}

   var
      i,k,kmax,kmin,kpeakmax,binmax,ithetamin:integer;
      h1,h2,binsum,hsbinsum:real;
      yn:char;
      outfile:text;
      newname:string[55];
      x0,y0,x1,y1,x2,y2:real;
      theta1,theta2,theta,thetamin:real;
      hsum,hpmin,hsmin,hpmean,hsmean:real;
begin
  for i:=1 to 3 do writeln(lst);
  kmax:=0;kmin:=0;binmax:=0;binsum:=0;hsum:=0.0;

{locate peak in pdf and get hmean}
 for k:=1 to Nbins do
 begin
(*   writeln(lst,'i,bin[i]:',k:3,bin[k]:6);*)
   hsum:=hsum+bin[k]*Geth(k);
   binsum:=binsum+bin[k];
   if (kmin=0) and (bin[k]>0) then kmin:=k;  {find first bin with data in it}
   if bin[k]>binmax then
   begin
     binmax:=bin[k];
     kmax:=k;
   end;

 end; {k loop}
 kmax:=2*kmax-kmin;  {revise kmax to include substrate points symetrically about pdf peak}
(* writeln(' kmin=',kmin,'  kmax=',kmax);*)

hmean:=hsum/binsum;
writeln(lst,'A total of ',binsum:8:0,' measurements from probe 1 were used to generate the probability density function');
writeln(lst,' mean film thickness = ',hmean:5:2,' mm.');

{find largest wave peak}
k:=Nbins;
while bin[k]=0 do k:=pred(k);
```

```pascal
hmaxdata:=Geth(k);
kpeakmax:=k;

{report min and max peak size}
hpmin:=1.2*hmean;
writeln(lst,' wave peaks range from ',hpmin:5:2,' mm. to ',hmaxdata:5:2,' mm.');

{find substrate thickness, mean}
hsbinsum:=0;hsum:=0.0;hsmin:=0.0;
for i:=1 to kmax do    {go from first bin to last bin with substrate data}
begin
  hsbinsum:=hsbinsum+bin[i];    {accumulate no. of data points}
  hsum:=hsum+bin[i]*Geth(i);    {accumulate weighted thickness }
 (* writeln(' i   hsbinsum   hsum :', i:3,hsbinsum:4,hsum:8:4);*)
end;
hsmin:=Geth(kmin);
hsmax:=Geth(kmax);
hsmean:=hsum/hsbinsum;
writeln(lst,' substrate thickness ranges from ',hsmin:5:2,' mm. to ',hsmax:5:2,
            ' with the mean = ',hsmean:5:2);

if not batch then
begin
  write(' write data to a file ? ');read(kbd,yn);writeln;
end {not batch}
else yn:='Y';

  if upcase(yn)='Y' then
  begin
    newname:=filename;
    delete(newname,pos('.',newname),4);
    newname:=newname+'.HIS';
    assign(outfile,newname);rewrite(outfile);
    for i:=1 to Nbins do
    begin
      h2:=Geth(i);
      writeln(outfile,h2,bin[i]/binsum/(hmax/Nbins));
    end;
    close(outfile);

    writeln(lst,' probability density for file ',filename,' saved to file ',newname);
    writeln(lst);
  end; { of upcase(yn)}
end;  {of Histo}
{*****************************************************************}
PROCEDURE ReadWriteHeader;   {Reads in the header info from the data file
                               and prints it out}
var i,j:integer;
    ok:boolean;
    garbage:string[42];
    longgarbage:string[70];
    trash:string[24];
    comma:string[1];
    fstring:string[6];
```

75

```
      volt1string,volt2string:string[6];
      Restring,Npointsstring:string[8];

begin
  clrscr;
  OpenInFile;
  writeln(lst);
  writeln(lst,'********* DATA FILE : ',filename);
  hmaxdata:=-1.0e-50;
  ok:=true;
        {read in header info and print from input file}
  singleprobe:=false;
  readln(infile,garbage);writeln(lst,garbage); {T water}

  read(infile,trash);readln(infile,Restring);
  for j:=1 to length(Restring) do delete(Restring,pos(' ',Restring),1);
  val(Restring,Re,code);if code<>0 then ok:=false;
  writeln(lst,trash,Re:8:0);

  for j:=3 to 5 do
  begin
    readln(infile,longgarbage);
    writeln(lst,longgarbage);
  end;

  read(infile,trash);
  if copy(trash,1,2)=' p' then     {only one probe sampled in this data file}
  begin
    singleprobe:=true;
    writeln(lst,' One probe sampled ');
    read(infile,comma,comma);  {skip two space}
    readln(infile,fstring);
    readln(infile,Npointsstring);
    readln(infile,garbage);
  end    {singleprobe}
  else
  begin
    readln(infile);
    writeln(lst,' both probes sampled');
    readln(infile,Npointsstring);
    read(infile,garbage,comma);
    readln(infile,fstring);
    readln(infile);
  end;  {not singleprobe}

  for i:=1 to length(NpointsString) do delete(NpointsString,pos(' ',NpointsString),1);
  for i:=1 to length(fstring) do delete(fstring,pos(' ',fstring),1);
  Val(NpointsString,Npoints,code);if code<>0 then ok:=false;
  Val(fstring,f,code);if code<>0 then ok:=false;
  if not ok then writeln(' header info not read correctly ');
  writeln(lst,' sampling frequency: ',f:8:0);
  dT:=1/f;
  if not singleprobe then Npoints:=Npoints*2;
  if Npoints>NpointsMax then
```

```
  begin
    write(lst,' data file truncated from ',Npoints:8,' to ');
    Npoints:=NpointsMax;
  end;
  writeln(lst,Npoints,' data points');
  fileflag:=true;
  Tdatamin:=0.0;Tdatamax:=(Npoints-1)/f;
end; {of ReadWriteHeader}

{##############################################################}
PROCEDURE ReadHeader;        {Reads in the header info from the data file}
var i,j:integer;
    ok:boolean;
    garbage:string[42];
    longgarbage:string[70];
    trash:string[24];
    comma:string[1];
    fstring:string[6];
    volt1string,volt2string:string[6];
    Restring,Npointsstring:string[8];

begin
  clrscr;
  OpenInFile;
  hmaxdata:=-1.0e-50;
  ok:=true;
        {read in header from input file}
  singleprobe:=false;
  readln(infile,garbage); {T water}

  read(infile,trash);readln(infile,Restring);
  for j:=1 to length(Restring) do delete(Restring,pos(' ',Restring),1);
  val(Restring,Re,code);if code<>0 then ok:=false;

  for j:=3 to 5 do
  begin
    readln(infile,longgarbage);
  end;

  read(infile,trash);
  if copy(trash,1,2)=' p' then      {only one probe sampled in this data file}
  begin
    singleprobe:=true;
    read(infile,comma,comma);  {skip two space}
    readln(infile,fstring);
    readln(infile,Npointsstring);
    readln(infile,garbage);
  end    {singleprobe}
  else
  begin
    readln(infile);
    readln(infile,Npointsstring);
    read(infile,garbage,comma);
    readln(infile,fstring);
    readln(infile);
```

77

```
   end; {not singleprobe}

   for i:=1 to length(NpointsString) do delete(NpointsString,pos(' ',NpointsString),1);
   for i:=1 to length(fstring) do delete(fstring,pos(' ',fstring),1);
   Val(NpointsString,Npoints,code);if code<>0 then ok:=false;
   Val(fstring,f,code);if code<>0 then ok:=false;
   if not ok then writeln(' header info not read correctly ');
   dT:=1/f;
   if not singleprobe then Npoints:=Npoints*2;{because if not singleprobe the number of data pairs is given}
   if Npoints>NpointsMax then
   begin
     Npoints:=NpointsMax;
   end;
   fileflag:=true;
end; {of ReadHeader}


{#########################################################################}
FUNCTION Readh:real;                {Reads the film thickness data from the
                                    data file as a string and converts it
                                    to a real number}

var hstring:string[5];
    i:integer;
    h:real;
begin
  read(infile,hstring);
  for i:=1 to length(hstring) do delete(hstring,pos(' ',hstring),1);
  val(hstring,h,code);
  if code<>0 then h:=0.0;
  Readh:=h;
end; {Readh}
{#########################################################################}
PROCEDURE Pass1;                   {Passes through the data file putting all
                                   film thicknesses into memory, determines the
                                   mean, and accumulates the histogram}
var h1,h2,hsum:real;
    i,k,count:integer;

begin
  if singleprobe then
  begin
    count:=0;hsum:=0.0;
    for i:=1 to Npoints do
    begin
      h1:=Readh;
      if i<=NpairsMax then data1[i]:=h1 else data2[i-NpairsMax]:=h1;
      hsum:=hsum+h1;
      k:=Getk(h1);
      bin[k]:=bin[k]+1;
      count:=count+1;
      if count=Npoints_per_line then
      begin
        count:=0;
        readln(infile);
```

```pascal
      end;  {count}
    end;  {i}
  hsum:=hsum/Npoints;
  if printheader then
    writeln(lst,' hmean = ',hsum:5:2,' mm.  (from sum(h1)/Npoints method)');
  end;  {singleprobe}


  if not singleprobe then
  begin
    count:=0;
    for i:=1 to Npoints div 2 do
    begin
      h1:=Readh;
      data1[i]:=h1;
      h2:=Readh;
      data2[i]:=h2;
      k:=Getk(h1);
      bin[k]:=bin[k]+1;
      count:=count+2;
      if count=Npoints_per_line then
      begin
        count:=0;
        readln(infile);
      end;  {count}
    end;  {i}
  end;  {not singleprobe}
  close(infile);
end;  {Pass1}
{**********************************************************************}
PROCEDURE GetNextFileName;      {for batch operation, increments the data
                                file name}
var namech:string[55];
    namechint,code:integer;
begin
    delete(filename,pos('.',filename),4);
    namech:=copy(filename,length(filename)-1,2);
    val(namech,namechint,code);
    if code<>0 then halt;
    namechint:=succ(namechint);
    str(namechint,namech);
    if namechint<10 then namech:='0'+namech;
    delete(filename,length(filename)-1,2);
    filename:=filename+namech+'.DAT';
  end;
{**********************************************************************}

BEGIN  {main program}
clrscr;
batch:=true;

Vwcount:=0;Vwsum:=0.0;Vw2sum:=0.0;Vwsig:=0.0;
Resum:=0.0;Re2sum:=0.0;Resig:=0.0;for i:=1 to Nbins do bin[i]:=0;

                {If only a plot of film thickness is needed, process only
                 one file and quit}
```

```pascal
write(' Plot only ? ');read(kbd,yn);if upcase(yn)='Y' then goto PlotOnly;

write(' Print header info for each file ? ');read(kbd,ynprint);writeln;
if upcase(ynprint)='Y' then printheader:=true else printheader:=false;

writeln(' enter complete input \path\file name for first file in the sequence;');
readln(filename);writeln;firstfile:=filename;
write(' enter number of files to be processed : ');readln(nfiles);

{First pass to get wave velocity, pdf, hmean, hsmin, hsmean, hsmax}
for i:=1 to nfiles do
begin
  if printheader then ReadWriteHeader else ReadHeader;
  writeln(' processing file # ',i:3,' of ',nfiles:3);
  Resum:=Resum+Re;
  Re2sum:=Re2sum+Re*Re;
  Pass1;
  if not singleprobe then
  begin
    GetVW;
    if (VW>0.0) and (VW<10.0) then     {be sure VW did not come back ridiculous}
    begin
      Vwsum:=Vwsum+VW;
      VW2sum:=VW2sum+VW*VW;
      VWcount:=succ(VWcount);
      if printheader then writeln(lst,filename,'   Vw=',Vw:6:3,' m/s.');
    end; {if VW}
    if ((VW<=0.0) or (VW>=10.0)) and printheader then writeln(lst,filename,' Vw calculation failed ');
  end;  {not singleprobe}
{ plot;}

  if i<Nfiles then GetNextFileName;
end; {i loop}
Histo;

  {determine mean and standard deviation of Re, VW for all the files}
numer:=Re2sum-Resum*Resum/Nfiles;
if (numer>0) and (Nfiles>1) then Resig:=sqrt(numer/(Nfiles-1));
Resig:=100.0*Resig/(Resum/Nfiles);
if VWcount >0 then numer:=VW2sum-VWsum*Vwsum/VWcount else numer:=0.0;
if (numer>0) and (VWcount>1) then VWsig:=sqrt(numer/(VWcount-1));
if (VWsum>0.0) and (VWcount>0.0) then VWsig:=100.0*VWsig/(VWsum/VWcount);

writeln(lst);
writeln(lst,' The above ',Nfiles:3,' files have an average Re = ',Resum/Nfiles:8:0,' with std. dev = ',Resig:5:2,' %');
if VWcount>0 then
  writeln(lst,' The above ',VWcount:3,' files have an average Vw = ',VWsum/VWcount:6:3,' with std. dev = ',VWsig:5:2,' %');

  {Second pass through files to get peak info, substrate lengths, and wave frequency}
printheader:=false;              {don't bother to print file info again}
```

```
hp:=0.0;Np:=0;hp2:=0.0;Ls2:=0.0;Nsubstrate:=0;Ls:=0.0;
Runtime:=0.0;
filename:=firstfile;
for i:=1 to Nfiles do
begin
  ReadHeader;
  Runtime:=Runtime+(Npoints-1)/f;
  Pass1;
  Gethp;
  writeln(lst,' After file ',filename,' runtime, hp, Np, Ls, Nsubstrate: ',
          runtime:8:4,hp:8:2,Np:5,Ls*1000:8:1,Nsubstrate:8);

GetNextFileName;
end;  {i loop}

      {determine wave frequency, and mean and standard deviation
       of substrate exposure time, wave peak height, based on data
       accumulated during second pass.}

freqw:=Np/Runtime;
if Nsubstrate>0 then Lsmean:=Ls/Nsubstrate else Lsmean:=0.0;
if Nsubstrate>0 then numer:=Ls2-Ls*Ls/Nsubstrate else numer:=0.0;
if numer>0.0 then Lssig:=100.0*sqrt(numer/(Nsubstrate-1))/Lsmean else Lssig:=0.0;
hpmean:=hp/Np;
numer:=hp2-hp*hp/Np;
if numer>0.0 then hpsig:=100.0*sqrt(numer/(Np-1))/hpmean else hpsig:=0.0;
writeln(lst);
writeln(lst,' Total run time = ',Runtime:8:4,' sec.');
writeln(lst,' mean and std. dev of substrate exposure time = ',Lsmean*1000:6:1,'ms.   ',Lssig:5:1,' %');
writeln(lst,' mean and std. dev of peak height             = ',hpmean:6:2,'mm.   ',hpsig:6:1,' %');
writeln(lst,' mean wave frequency      = ',freqw:6:2,' hz');
writeln(lst);writeln(lst);

halt;      {If in batch mode, quit}

PlotOnly:
write(' enter input \PATH\filename for plotting :');readln(filename);
Readwriteheader;
Pass1;
Plot;
end.
```

SΞRI ⬡

APPENDIX C

DEVELOPMENT OF THE INSTABILITIES
IN MOLTEN-SALT FILMS
EVOLUTION EQUATIONS

Final Report

INSTABILITIES IN MOLTEN-SALT FILMS

Part 3: EVOLUTION EQUATIONS

Subcontract No. HX-7-07131-1
under
Prime contract No. DE-AC02-83CH10093

from

SHD Associates, Inc.
2735 Simpson St.
Evanston, IL 60201

to

Solar Energy Research Institute
1617 Cole Blvd.
Golden, CO 80401

December 31, 1988

1. INTRODUCTION

The molten-salt film in a DAR receives large fluxes of heat from an array of heliostats. These fluxes may be non-uniform in space and lead to conditions that cause instabilities and dryout of the film. In particular, if the film is in the roll-wave regime as shown in Figure 1, there are thin substrates that are particularly susceptible.

In order to obtain some insight into the stability of the liquid film in the substrate region between roll waves, we extend our previous work and consider a substrate with mean flow on a plate that heats up due to incident flux and assume that the gas-liquid interface is a zero-flux boundary. We suppose that the incident flux is either linear in cross-stream coordinate or sinusoidal in simulation of ripples.

We derive a single partial differential equation for the unsteady interface shape h appropriate to distortions that have slow variations along the plate. We include the effects of viscosity, surface tension, thermocapillarity, gravity and the additional effects of van der Waals attractions.

2. FORMULATION

Consider the liquid layer shown in Figure 1. The plate at $z = 0$ has the (unknown) temperature T_W while the interface at $z = h(x,y,t)$ supports zero heat flux; T_W is determined by thermal conditions at the wall.

The thermal field satisfies the energy equation

$$\rho c_p (T_t + \underline{v} \cdot \nabla T) = k\nabla^2 T + \frac{d\hat{q}}{dz} \tag{2.1a}$$

with

$$T = T_W \quad , \quad z = 0 \tag{2.1b}$$

$$\nabla T \cdot \underline{n} = 0 \quad , \quad z = h \qquad (2.1c)$$

where the unit normal vector

$$\underline{n} = (-h_x, -h_y, 1)(1 + h_x^2 + h_y^2)^{-1/2} \qquad (2.1d)$$

and the incident radiative flux q satisfies

$$q = q_0[1 + q_s(y)]e^{\sigma(z-h)} \quad . \qquad (2.2)$$

Here ρ, c_p and k are the liquid's density, specific heat and thermal conductivity, respectively. The vector $\underline{v} = (u,v,w)$ is the liquid's velocity and t is time. The incident flux has amplitude q_0, modulation $q_s(y)$ and extinction coefficient σ.

The velocity field satisfies the Navier-Stokes and continuity equations,

$$\rho(\underline{v}_t + \underline{v} \cdot \nabla \underline{v}) = -\nabla p + \mu \nabla^2 \underline{v} - \nabla \phi + \rho g \ (\sin \beta, 0, -\cos \beta) \qquad (2.3a)$$

$$\nabla \cdot \underline{v} = 0 \qquad (2.3b)$$

where μ is the viscosity of the liquid, p is the pressure, g is the acceleration of gravity, and we have included long-range London-van der Waals attractions through potential ϕ,

$$\phi = \phi_B + \frac{A'}{6\pi h^3} \quad . \qquad (2.4)$$

The Hamaker constant A' is positive for the "negative disjoining pressures" that might cause film rupture.

There is no penetration or slip on the plate,

$$\underline{v} = \underline{0} \quad , \quad z = 0 \quad . \qquad (2.5)$$

The wall is allowed to heat up. Bohn (1988, private communication) shows that

$$\alpha T_{W_t} = q_0(1 + q_s)(1 - \rho_0)e^{-\sigma h} + k_T T_z \big|_{z=0} \quad , \qquad (2.6a)$$

$$T_W = T_{W_0} \quad , \quad t = 0 \qquad (2.6b)$$

88

where ρ_0 is the reflection coefficient and α is the product of the wall density, thickness and heat capacity.

On the interface

$$\underline{T} \cdot \underline{n} \cdot \underline{t}^{(\alpha)} = \frac{d\hat{\sigma}}{ds^{(\alpha)}} = \frac{d\hat{\sigma}}{dT} \frac{dT}{ds^{(\alpha)}} \quad , \quad z = h \quad \text{for} \quad \alpha = 1,2 \qquad (2.7a)$$

where $\underline{T}$ is the stress tensor of the liquid and the equation of state for the surface tension $\hat{\sigma}$ is

$$\hat{\sigma} = \sigma_0 - \sigma_1(T) \qquad (2.7b)$$

such that

$$\frac{d\sigma_1}{dT} > 0 \quad . \qquad (2.7c)$$

In addition

$$\underline{T} \cdot \underline{n} \cdot \underline{n} = 2H\hat{\sigma} \quad , \quad z = h \quad , \qquad (2.7d)$$

$$w = h_t + uh_x + vh_y \quad , \quad z = h \quad , \qquad (2.7e)$$

and

$$\nabla T \cdot n = 0 \quad , \quad z = h \quad . \qquad (2.7f)$$

Condition (2.7a) balances the surface shear stress and the surface-tension gradient, the thermocapillary balance. Here $t^{(1)}$ and $t^{(2)}$ are mutually-orthogonal unit tangent vectors. Condition (2.7d) balances surface normal stresses with surface tension times curvature,

$$2H = \left[h_{xx}(1 + h_y^2) - 2h_x h_y h_{xy} + h_{yy}(1 + h_x^2) \right] (1 + h_x^2 + h_y^2)^{-3/2} \quad . \qquad (2.7g)$$

Form (2.7e) is the kinematic condition, and form (2.7f) defines the interface as a zero-heat-flux boundary.

89

Let us now assume that $\left|\frac{\partial}{\partial x}\right|$ $\left|\frac{\partial}{\partial y}\right| \ll 1$. In order to preserve continuity, $|w| \ll 1$ also. A formal perturbation analysis gives the leading-order system corresponding to equations (2.1)-(2.7) appropriate to slowly-varying solutions to the coupled hydrodynamic-thermal responses. These are as follows:

$$kT_{zz} + \frac{dq}{dz} = 0 \tag{2.8a}$$

$$\mu u_{zz} - (p + \phi)_x + \rho g \sin \beta = 0 \tag{2.8b}$$

$$\mu v_{zz} - (p + \phi)_y \qquad\qquad = 0 \tag{2.8c}$$

$$\qquad - (p + \phi)_z - \rho g \cos \beta = 0 \tag{2.8d}$$

$$u_x + v_y + w_z = 0 \tag{2.8e}$$

where

$$q = q_0[1 + q_s(y)]e^{\sigma(z-h)} \quad , \tag{2.8f}$$

$$\phi = \phi_B + \frac{A'}{6\pi h^3} \tag{2.8g}$$

with

$$T = T_W \quad , \quad z = 0 \tag{2.8h}$$

$$\alpha T_{W_t} = q_0(1 + q_s)(1 - \rho_0)e^{-\sigma h} + k_T T_z \Big|_{z=0} \tag{2.8i}$$

$$T_W = T_{W_0} \quad , \quad t = 0 \tag{2.8j}$$

$$\underline{v} = \underline{0} \quad , \quad z = 0 \tag{2.8k}$$

$$\mu u_z + \sigma_1' \frac{dT}{dx} = 0 \quad , \quad z = h \tag{2.8\ell}$$

$$\mu v_z + \sigma_1' \frac{dT}{dy} = 0 \quad , \quad z = h \tag{2.8m}$$

$$-p = [\sigma_0 - \sigma_1](h_{xx} + h_{yy}) \quad , \quad z = h \tag{2.8n}$$

$$w = h_t + uh_x + vh_y \quad , \quad z = h \tag{2.8o}$$

$$kT_z = 0 \quad , \quad z = h \tag{2.8p}$$

where

$$\frac{dT}{dx} = T_x + h_x T_z \tag{2.9a}$$

$$\frac{dT}{dy} = T_y + h_y T_z \quad . \tag{2.9b}$$

Note that if $\beta = \rho c_p h_0/\alpha \ll 1$, which is ordinarily so, then the full time-dependent form of the wall balance, eqns. (2.8i,j), is retained. The result is a wall temperature T_W that varies slowly in t, x and y.

3. DERIVATION OF THE EVOLUTION EQUATION

We first solve for the temperature field. We integrate (2.8a) and use (2.8p) to obtain

$$kT_z + q_0[1 + q_s(y)][e^{\sigma(z-h)} - 1] = 0 \quad . \tag{3.1a}$$

We integrate (3.1a) and use (2.8h) to obtain

$$k(T-T_W) + q_0[1 + q_s(y)]\{\frac{1}{\sigma}[e^{\sigma(z-h)}-e^{-\sigma h}] - z\} = 0 \quad . \tag{3.1b}$$

We now use relations (2.8i,j) to find that

$$T_W = T_{W_0} + \frac{q_0(1+q_s)}{\alpha}\left\{t - \rho_0\int_0^t e^{-\sigma h(x,y,\tau)}d\tau\right\} \quad . \tag{3.1c}$$

Before we proceed further, let us analyze the temperature distribution T. For small σ,

$$T \sim T_W + \frac{\sigma q_0}{k}[1 + q_s(y)](hz - \frac{1}{2}z^2) \quad , \quad \sigma \to 0 \quad , \tag{3.2a}$$

where

91

$$T_W \sim T_{W_0} + \frac{q_0(1+q_s)}{\alpha} \left\{ (1-\rho_0)t + \rho_0\sigma\int_0^t h \, d\tau \right\} \quad . \tag{3.2b}$$

The temperature is small and increases montonically toward the interface. As time increases, the whole temperature level increases. For general σ, T increases monotonically from the plate to the interface and thus the layer is "heated from above". In fact the temperature difference ΔT,

$$\Delta T - T\big|_{z=h} - T\big|_{z=0}$$

$$= -\frac{q_0}{k} \left\{ \frac{1}{\sigma} [1 - e^{-\sigma h}] - h \right\} \tag{3.2c}$$

varies from $\Delta T = 0$ at $\sigma = 0$ to $\Delta T = \frac{q_0 h}{k} (1 + q_s)$ as $\sigma \to \infty$.

We now turn to the solution of the velocity field. We integrate (2.8d) and use (2.8n) to obtain

$$p = \rho g(h-z)\cos \beta - [\sigma_0 - \sigma_1(T\big|_{z=h})](h_{xx} + h_{yy}) \tag{3.3a}$$

since ϕ is independent of z. Integrate (2.8b) and use (2.8ℓ) to obtain

$$\mu u_z = [p + \phi - \rho gx \sin \beta]_x(z-h) - \left[\sigma_1'(T) \frac{dT}{dx}\right]_{z=h} \quad . \tag{3.3b}$$

Now we integrate (3.3b) and use (2.8k) to obtain

$$\mu u = [p + \phi - \rho gx \sin \beta]_x(\tfrac{1}{2} z^2 - hz) - \left[\sigma_1'(T) \frac{dT}{dx}\right]_{z=h} z \quad . \tag{3.3c}$$

By analogous procedures, we obtain

$$\mu v = [p + \phi]_y(\tfrac{1}{2} z^2 - hz) - \left[\sigma_1'(T) \frac{dT}{dy}\right]_{z=h} z \quad . \tag{3.3d}$$

We now reformulate the continuity equation (2.8e). We integrate on z from z = 0 to z = h, use the kinematic condition (2.8o) and find that

$$h_t + \frac{\partial}{\partial x} \int_0^h u \, dz + \frac{\partial}{\partial y} \int_0^h v \, dz = 0 \quad . \tag{3.4}$$

We substitute into eqn. (3.4) for u and v from eqns. (3.3c,d) to obtain

$$\mu h_t - \frac{1}{3} \nabla_1 \cdot [h^3 \nabla_1 (p + \phi - \rho g x \sin \beta)] - \frac{1}{2} \left\{ h^2 \left[\sigma_1'(T) \frac{dT}{dx} \right]_{z=h} \right\}_x$$

$$- \frac{1}{2} \left\{ h^2 \left[\sigma_1'(T) \frac{dT}{dy} \right]_{z=h} \right\}_y = 0 \qquad (3.5)$$

where

$$\nabla_1 = \left[\frac{\partial}{\partial x}, \frac{\partial}{\partial y}, 0 \right] \quad . \qquad (3.6)$$

But, from eqn. (3.3a), eqn. (3.5) becomes

$$\mu h_t - \frac{1}{3} \rho g \cos \beta \nabla_1 \cdot \left[h^3 \nabla_1 h \right] + \frac{A'}{6\pi} \nabla_1 \cdot \left[h^{-1} \nabla_1 h \right] + \rho g \sin \beta \, h^2 h_x$$

$$+ \frac{1}{3} \nabla_1 \cdot \left\{ h^3 \nabla_1 [\sigma_0 - \sigma_1(T|_{z=h})] \nabla_1^2 h \right\}$$

$$- \frac{1}{2} \left\{ h^2 \left[\sigma_1'(T) \frac{dT}{dx} \right]_{z=h} \right\}_x - \frac{1}{2} \left\{ h^2 \left[\sigma_1'(T) \frac{dT}{dy} \right]_{z=h} \right\}_y = 0 \qquad (3.7)$$

where we have used form (2.4). Now from (3.1b) we define the surface temperature T_s,

$$T_s = T \big|_{z=h} = T_W(x,y,t) - \frac{q_0}{\sigma k} [1 + q_s(y)] \{1 - \sigma h - e^{-\sigma h}\} \qquad (3.8)$$

and from (2.9) and (3.1b),

$$\frac{dT}{dy} \bigg|_{z=h} = \frac{q_0}{k} \left\{ [1+q_s(y)](1-e^{-\sigma h})h_y - \frac{1}{\sigma} q_s'(y)[1-\sigma h-e^{-\sigma h}] \right\} + T_{W_y} \qquad (3.9a)$$

and

$$\frac{dT}{dx} \bigg|_{z=h} = \frac{q_0}{k} [1 + q_s(y)](1-e^{-\sigma h})h_x + T_{W_x} \quad . \qquad (3.9b)$$

Hence,

$$\left\{ h^2 \left[\sigma_1'(T) \frac{dT}{dx} \right]_{z=h} \right\}_x + \left\{ h^2 \left[\sigma_1'(T) \frac{dT}{dy} \right]_{z=h} \right\}_y$$

$$= \nabla_1 \cdot \{ h^2 \sigma_1'(T_s) \nabla_1 T_s \} . \qquad (3.9c)$$

Finally, we use (3.9) and convert (3.7) into final form:

$$\mu h_t - \frac{1}{3} \rho g \cos \beta \, \nabla_1 \cdot [h^3 \nabla_1 h] + \frac{A'}{6\pi} \nabla_1 \cdot [h^{-1} \nabla_1 h] + \rho g \sin \beta \, h^2 h_x$$

$$+ \frac{1}{3} \nabla_1 \cdot \{h^3 \nabla_1 [\sigma_0 - \sigma_1 (T_s)] \nabla_1^2 h\}$$

$$- \frac{1}{2} \nabla_1 \cdot \{h^2 \sigma_1'(T_s) \nabla_1 T_s\} = 0 \quad . \qquad (3.10)$$

This equation governs the three-dimensional instability of the layer against long-wave disturbances. It includes as a special case the steady, dimpled interface produced by spatially varying incident fluxes as modeled by $q_s(y)$.

4. DISCUSSION

The interface between the liquid and the gas is determined by eqn. (3.10), with T_s given by eqn. (3.8) and T_W given by (3.1c).

This system was derived subject to the approximation that $\frac{\partial}{\partial x}$ and $\frac{\partial}{\partial y}$ were small, say $O(\epsilon)$, compared with variations $\frac{\partial}{\partial z}$, given that all other parameters are of unit order. In particular, we have assumed that $\epsilon \ll \sigma$, even when the extinction coefficient σ is fairly small. Thus, the convective and advective effects, which are $O(\epsilon)$, are all smaller than $O(\sigma)$. If σ were, indeed, zero, then we would have to substantially modify the analysis, given that convective and/or advective effects would be important at leading order.

This system has been derived for the case of the heating-up wall. Clearly, one can formally extract the constant wall-temperature limit by allowing $\alpha \to \infty$, which from eqn. (3.1c) gives $T_W = T_{W_0}$.

The system applies to isothermal falling films if we take the limit $q_0 \to 0$. In this case eqn. (3.10) reduces that of Atherton and Homsy (1976) if one adds to the left-hand side the term

$$\frac{2}{15} \frac{\rho^3 g^2 \sin^2 \beta}{\mu^2} (h^6 h_x)_x \quad . \tag{4.1}$$

This term is responsible for the surface-wave instability of the falling film and is absent from eqn. (3.10) since it arises at the next order in powers of ϵ.

Finally, one can drastically simplify eqn. (3.10) and attempt to examine the tendency of a falling film to thin and possibly rupture through the joint effects of longitudinal flow, transverse surface deflections and thermocapillarity. The effect that Simon and Hsu (1970) find is dependent on the layer being "heated from below" and results in layers that thin in the downstream direction. Here we have a layer "heated from above" and the corresponding balances would make the layer tend to thicken in the flow direction.

REFERENCES

Ahterton, R. W. and Homsy, G. M.   1976   Chem. Eng. Comm. 2, 57-77.

Simon, F. F. and Hsu, Y.-Y.   1970   NASA TN D-5624 report, 1-34.
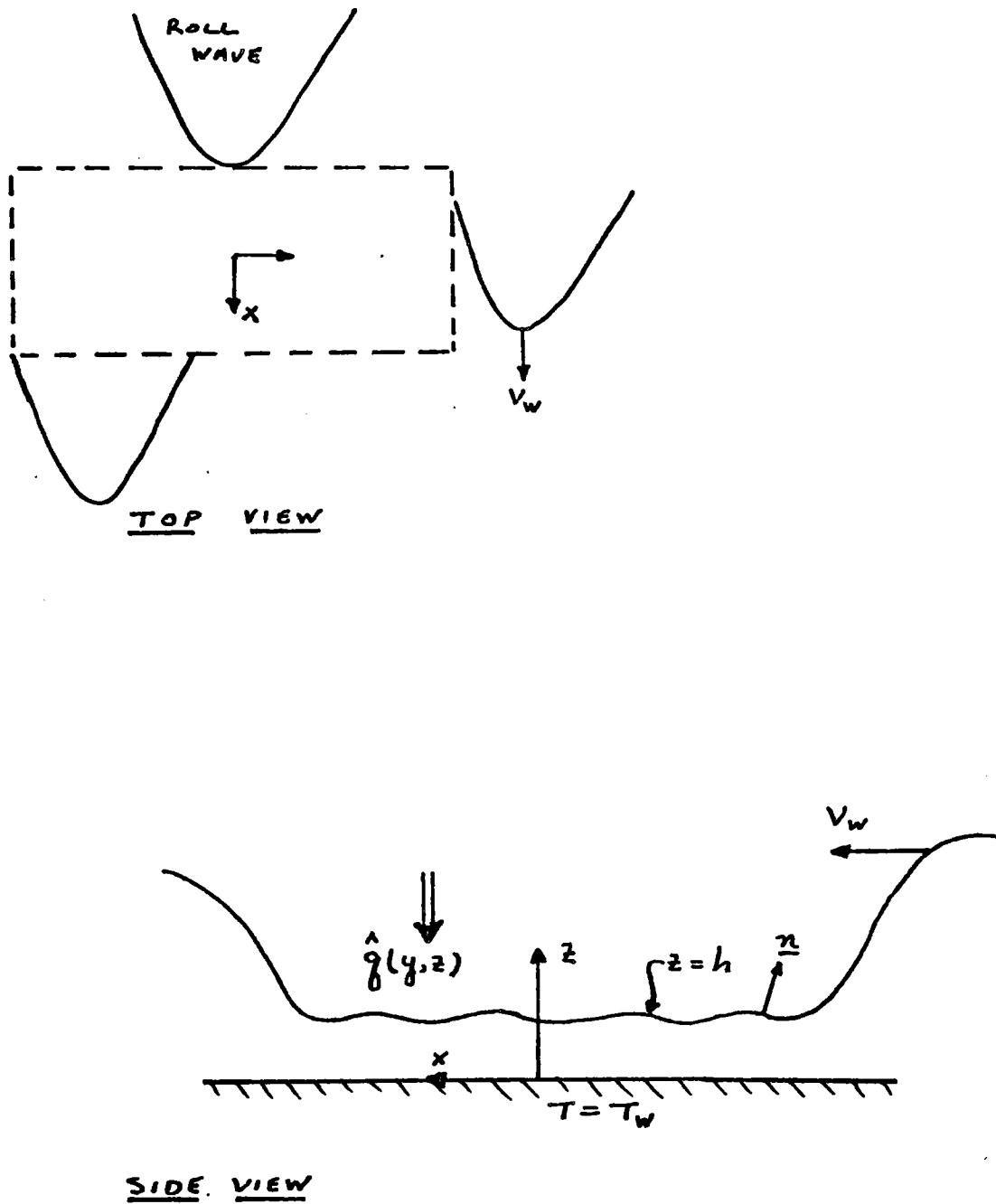
Figure 1: Configuration of the film.

APPENDIX D

DEVELOPMENT OF A SCALING LAW FOR THERMOCAPILLARY BREAKDOWN OF A WAVY, VERTICAL FALLING FILM EXPOSED TO HEAT FLUX

Consider a coordinate system with x in the downward direction, y horizontal across the flow, and z normal to the flow (see Figure D-1). A lateral temperature gradient $\partial T/\partial y$ will create a lateral surface shear if the surface tension varies with temperature (typical of most liquids):

$$\mu \frac{\partial v}{\partial z} = \gamma \frac{\partial T}{\partial y} \quad , \tag{D-1}$$

where

$$\gamma = \left| \frac{d\sigma}{dT} \right| , \text{ a fluid property .}$$

Now let V_m be a typical lateral velocity, h_o be the mean substrate thickness at local conditions, and ΔT be the lateral temperature difference that exists over the initial disturbance in a substrate of lateral extent W_o. Equation D-1 then becomes in terms of these scaling values

$$\frac{\mu V_m}{h_o} = \gamma \frac{\Delta T}{W_o} \quad . \tag{D-2}$$

If this typical lateral velocity is much greater than the mean downward velocity in the substrate, then the substrate is likely to thin sufficiently to cause dryout.
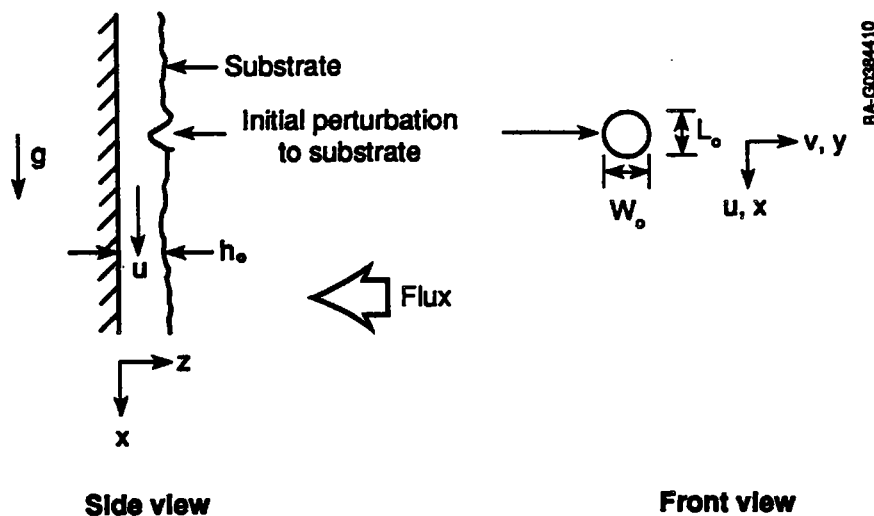
Figure D-1.   Coordinate system

In the downward direction, the balance between viscous shear and gravity is

$$\frac{\mu U_o}{h_o^2} = \rho g \quad . \tag{D-3}$$

When V_o is the mean downward substrate velocity, the energy equation is

$$\rho c u \frac{\partial T}{\partial x} = k \frac{\partial^2 T}{\partial z^2} \quad ,$$

which scaled over the initial disturbance becomes

$$\rho c \frac{U_o \Delta T}{L_o} = k \frac{\partial^2 T}{\partial z^2} \tag{D-4}$$

because the same ΔT exists laterally as in the flow direction. The right side of Eq. D-4 can be written q_w/h_o, where q_w is the heat flux. This gives

$$\Delta T = \frac{q_w L_o}{U_o \rho c h_o} \quad . \tag{D-5}$$

Eliminating ΔT from Eqs. D-2 and D-5, we find a relationship between the lateral velocity and the mean downward velocity of

$$\frac{V_m}{U_o} \geq \frac{\gamma}{\mu} \frac{q_w}{\rho c} \frac{L_o}{W_o} \frac{1}{U_o^2} \equiv n \quad .$$

This ratio n must be determined experimentally. It determines how large V_m must be relative to U_o before dryout occurs. Expressing U_o as the mean substrate thickness from Eq. D-3 and rearranging it, we find

$$q_B \frac{\gamma \mu}{\rho^3 c g^2} \left(\frac{g}{\nu^2}\right)^{4/3} \geq n \frac{W_o}{L_o} \left(\frac{h_o^3 g}{\nu^2}\right)^{4/3} \quad . \tag{D-6}$$

The term $h_o^3 g/\nu^2$ in Eq. D-6 is the dimensionless mean substrate thickness, which depends only on the effective Reynolds number of the substrate that, in turn, only depends on the overall film Reynolds number. The initial disturbance aspect ratio W_o/L_o is typically unity based on our observations of the substrate. So we can rewrite Eq. D-6 as

$$\tilde{q}_B = q_B \frac{\gamma}{c} \left(\mu^5 \rho g^2\right)^{-1/3} = f(Re) \quad , \tag{D-7}$$

where q_B is the flux required to cause dryout.

APPENDIX E

EQUATIONS AND ALGORITHMS USED TO
PREDICT RADIATIVE TRANSFER IN A DAR

E.1   The Equation of Radiative Transfer

The DAR molten salt film, laden with cobalt oxide particles and falling down a nearly vertical metallic plane, is modeled* locally as a one-dimensional problem of length L.   The corresponding coordinate system is sketched in Figure E-1.   This one-dimensional assumption is valid for thin films because the transport of radiation across the film is much greater than along it.   The curvature of the falling film is also neglected because the thickness of the film is much less than the radius of curvature.

With this consideration, the spectral equation of transfer within the film is written as

$$\mu \frac{\partial I_\lambda(x,y,\mu,\phi)}{\partial y} = \sigma_{a\lambda} I_{b\lambda} T(x,y) - \sigma_{e\lambda} I_\lambda(x,y,\mu,\phi)$$

$$+ \frac{\sigma_{s\lambda}}{4\pi} \int_{\mu'=-1}^{1} \int_{\phi'=0}^{2\pi} I_\lambda(x,y,\mu',\phi') \; \Phi(\mu',\phi\mu,\phi) \; d\mu' d\phi' \; , \qquad \text{(E-1)}$$
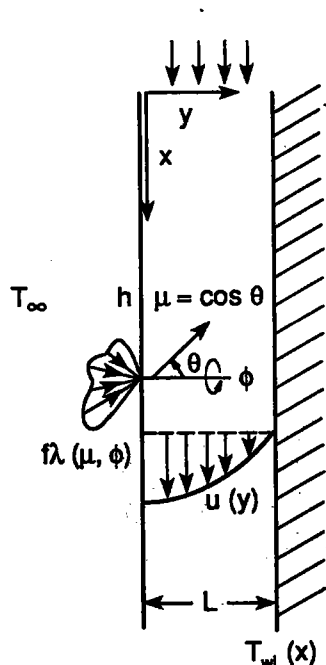
where

I = the intensity (energy per unit projected area per unit steradian centered around (μ,ϕ) per unit wavelength interval $d\lambda$ around λ)

ϕ = the azimuthal angle $\mu = \cos\theta$

θ = the polar angle measured from the y-direction

T = the temperature

σ = the radiative transfer coefficients

a,e,s = absorption, extinction, and scattering, respectively, where extinction is the sum of absorption and scattering

b = blackbody

λ = spectral value.

Figure E-1. Coordinate system for modeled molten salt film

$$I_{b\lambda}(T) = \frac{n_{film}^2 2C_1}{\lambda^5 [\exp(C_2/\lambda T) - 1]} \; . \qquad \text{(E-2)}$$

Here n_{film} is the index of refraction of the medium (film) in which the black-body emission is being evaluated. In Eq. E-2, $I_{b\lambda}$ is the intensity per unit wavelength interval in vacuum and air, not in the medium. This is because we want to keep track of the radiative energy in terms of the incident wave-lengths measured outside the film (i.e., in air). The constants C_1 and C_2 are equal to 0.59544×10^{-16} W.m^2 and $14,388$ µm.K, respectively. Assuming the particles in the film are spherical, the scattering phase function in the transfer equation is expressed as

$$\Phi(\mu',\phi' \to \mu,\phi) = \sum_{n=0}^{N} \sum_{m=0}^{\infty} (2 - \delta_{0m})a_n^m P_n^m(\mu)P_n^m(\mu') \cos m(\phi-\phi') \ . \qquad (E-3)$$

Here N is the degree of anisotropy of scattering, P_n^m are the Legendre functions, and δ is the Kronecker delta function. The radiative coefficients are related to the individual particle properties using the following relations

$$\sigma_i = \frac{3f_v Q_i(\alpha,m)}{2D} \ , \quad i = a,e,s \ , \qquad (E-4)$$

where

  D = the diameter of the monodispersed particles

  $\alpha = \pi D/\lambda_{film}$, the size parameter, $\lambda_{film} = n_{film}$, and λ = the wavelength in the film

  m = n + ik, the normalized refractive index of the particles $(= m_{particle}/n_{film})$, n = the index of refraction, and k = the index of absorption

  f_v = solid volume fraction

  Q = corresponding radiative efficiency of the particle as computed by the Mie theory (Bohren and Huffman 1983; Dave 1968; Kerker 1961).

The general radiative boundary conditions for a one-dimensional medium are given by

$$I_\lambda(x,0, + \mu,\phi) = f_\lambda(\mu,\phi) + \varepsilon_{0\lambda} I_{b\lambda} T_{w0}(x) + \rho_{0\lambda}^s I_\lambda(x,0, - \mu,\phi)$$

$$+ \frac{\rho_{0\lambda}^d}{\pi} \int_{\mu'=0}^{1} \int_{\phi'=0}^{2\pi} I_\lambda(x,0,-\mu',\phi')\mu' \, d\mu'd\phi' \quad \mu > 0 \ , \qquad (E-5a)$$

$$I_\lambda(x,L, - \mu,\phi) = \varepsilon_{L\lambda} I_{b\lambda} T_{wL}(x) + \rho_{L\lambda}^s I_\lambda(x,L,+\mu,\phi)$$

$$+ \frac{\rho_{L\lambda}^d}{\pi} \int_{\mu'=0}^{1} \int_{\phi'=0}^{2\pi} I_\lambda(x,L,+\mu',\phi')\mu' \, d\mu'd\phi' \quad \mu > 0 \ , \qquad (E-5b)$$

where

ε,ρ = emissivity and reflectivities of the boundaries, respectively,

f_λ = function specifying the form of the incident radiation after it has penetrated the film

0,L = values at y = 0 and y = L, respectively,

w = boundary or wall

s,d = specular and diffuse, respectively.

For simplicity, the critical-angle reflection effects were ignored in this formulation. The blackbody intensities $I_{b\lambda}$ are evaluated from Eq. E-2.

For the particular physical system at hand, the liquid DAR, the y = 0 surface is exposed to incoming solar flux, and the y = L surface is an opaque wall. This simplifies the boundary conditions to

$$I_\lambda(x,0,+\mu,\phi) = f_\lambda(\mu,\phi) + \frac{\rho_{0\lambda}^d}{\pi} \int_{\mu'=0}^{1} \int_{\phi'=0}^{2\pi} I_\lambda(x,0,-\mu',\phi')\mu' \, d\mu' d\phi' \quad \mu > 0 \quad , \text{(E-6a)}$$

$$I_\lambda(x,L,-\mu,\phi) = \varepsilon_{L\lambda} I_{b\lambda} T_{wL}(x)$$

$$+ \frac{\rho_{L\lambda}^d}{\pi} \int_{\mu'=0}^{1} \int_{\phi'=0}^{2\pi} I_\lambda(x,L,+\mu',\phi')\mu' \, d\mu' d\phi' \quad \mu > 0 \quad . \quad \text{(E-6b)}$$

Because the back surface is an oxidized metal, the specular components of reflection are neglected.

The azimuth angle ϕ does not appear explicitly in the equation of transfer, Eq. E-1, and the ϕ dependence of I is introduced via the boundary conditions, Eqs. E-5 and E-6. The level of complexity of the transfer equation and the boundary conditions is higher because of the additional integration over ϕ that has to be performed. To simplify these equations, Kumar and Felske (1986) proposed that the intensity expand as a Fourier series in ϕ. This requires evaluating a corresponding Fourier series for the boundary function $f_\lambda(\mu,\phi)$, which is usually complicated. Because the goal of the analysis is to predict the heat fluxes and temperatures in the film and the individual intensities are not of interest, an "integrated intensity" J is defined as

$$J_\lambda(x,y,\mu) = \int_{\phi=0}^{2\pi} I_\lambda(x,y,\mu,\phi) \, d\phi \quad , \quad \text{(E-7)}$$

which modifies the transfer equation to

$$\mu \frac{\partial J_\lambda(x,y,\mu)}{\partial y} = 2\pi\sigma_{a\lambda} I_{b\lambda} T(x,y) - \sigma_{e\lambda} J_\lambda(x,y,\mu)$$

$$+ \frac{\sigma_{s\lambda}}{2} \int_{\mu'=-1}^{1} J_\lambda(x,y,\mu')\zeta(\mu' \to \mu) \, d\mu' \quad , \quad \text{(E-8)}$$

where ζ is obtained by integrating Eq. E-3 over all ϕ:

$$\zeta(\mu' \to \mu) = \sum_{n=0}^{N} a_n P_n(\mu) P_n(\mu') , \quad a_0 = 1 . \tag{E-9}$$

The corresponding boundary conditions on J are

$$J_\lambda(x,0,+\mu) = g_\lambda(\mu) + \frac{\rho_{0\lambda}^d}{\pi} \int_{\mu'=0}^{1} J_\lambda(x,0,-\mu')\mu' \, d\mu' \quad \mu > 0 , \tag{E-10a}$$

$$J_\lambda(x,L,-\mu) = 2\pi\varepsilon_{L\lambda}I_{b\lambda}T_{wL}(x) + \frac{\rho_{L\lambda}^d}{\pi} \int_{\mu'=0}^{1} J_\lambda(x,L,+\mu')\mu' \, d\mu' \quad \mu > 0 , \tag{E-10b}$$

where

$$g_\lambda(\mu) = \int_{\phi=0}^{2\pi} f_\lambda(\mu,\phi) \, d\phi . \tag{E-11}$$

Introducing J simplified the equations considerably by eliminating the integrals involving ϕ in the transfer equation and boundary conditions. Even though the individual intensities cannot be found, the radiative heat flux and its divergence are easily computed as

$$q_r(x,y) = \int_\lambda \int_{\phi=0}^{2\pi} \int_{\mu=-1}^{1} I_\lambda(x,y,\mu,\phi)\mu \, d\mu d\phi d\lambda ,$$

$$= \int_\lambda \int_{\mu=-1}^{1} J_\lambda(x,y,\mu)\mu \, d\mu d\lambda , \tag{E-12}$$

$$\frac{\partial q_r(x,y)}{\partial y} = 4\pi \int_\lambda \sigma_{a\lambda} I_{b\lambda} T(x,y) \, d\lambda - \int_\lambda \sigma_{a\lambda} \int_{\mu=-1}^{1} J_\lambda(x,y,\mu)\mu \, d\mu d\lambda . \tag{E-13}$$

E.2 The Energy Equation

The radiative energy in the falling film is in equilibrium with the other modes of energy transport. The boundary conditions and the temperature term strongly link the transfer equation to the energy equation. The energy equation is

$$\rho C_\rho u(y) \frac{\partial T(x,y)}{\partial x} = k \frac{\partial^2 T(x,y)}{\partial y^2} - \frac{\partial q_r(x,y)}{\partial y} , \tag{E-14}$$

where

ρ = film density

C_p = specific heat

k = coefficient of thermal conductivity

u = velocity in the x-direction, down.

A fully developed velocity profile is assumed in the film that for laminar flows is given by

$$u(y) = \frac{3\hat{m}}{2\rho L}\left[1 - \frac{y^2}{L^2}\right] = \frac{3}{2} U\left[1 - \frac{y^2}{L^2}\right] ,$$ (E-15)

where $\hat{m}$ is the mass flow rate per unit length in the z-direction and U is the bulk-mean velocity.

The boundary conditions for the temperature field are given by

$$x = 0, \; 0 < y < L \qquad T(0,y) = T_{in} ,$$

$$y = 0, \; x > 0 \qquad h(T_\infty - T(x,0)) = -k\frac{\partial T(x,y)}{\partial y}\Big|_{y=0} ,$$

$$y = L, \; x > 0 \qquad q_r - k\frac{\partial T(x,y)}{\partial y}\Big|_{y=L} = 0 ,$$ (E-16)

where h is the convective heat-transfer coefficient at the film surface ($y = 0$) and T_∞ is the ambient temperature. The $y = L$ surface is insulated, and the convective and radiative energies are balanced. The free surface of the film is exposed to the ambient and loses heat by convection.

E.3 Numerical Algorithms

The transfer equation, Eq. E-8, along with its corresponding boundary conditions, Eq. E-10, are solved by using the DDOM (Kumar, Majumdar, and Tien 1988). The first step is to replace the integral over μ' by a quadrature. If the μ_i's are the quadrature points between -1 and $+1$ corresponding to a 2M-order quadrature, and w_i's are the corresponding weights, the equation of transfer is reduced to the following system of ordinary differential equations after assuming that $\partial J/\partial x \approx 0$ locally:

$$\mu_i\frac{dJ_i(x,y)}{dy} = 2\pi\sigma_a I_b T(x,y) - \sigma_e J_i(x,y) + \frac{\sigma_s}{2}\sum_{\substack{j=-M \\ j\neq 0}}^{M} w_j J_j(x,y)\zeta(\mu_j\to\mu_i) ,$$

$$i = -M, \ldots, M , \; i \neq 0 ,$$ (E-17)

where $J_i(x,y) = J(x,y,\mu_i)$. Here the subscript λ was suppressed from J, σ, and I_b for clarity. The order 2M of the quadrature contains an even number of points to avoid the value $\mu = 0$, which has no distinct boundary condition at the two edges of the vertical plane. For the sake of simplicity, $i = -M, \ldots, -1$ corresponds to the negative μ and $I = 1, \ldots, M$ to the positive. Also the μ's are so ordered that $-\mu_j = \mu_{-j}$ and $w_{-j} = w_j$. Equation E-17 constitutes a $2M^{th}$-order system of ordinary differential equations at each x-location. It is a two-point boundary-value problem where 2M boundary conditions are specified by the following:

$$J_{+i}(x,0) = g_i + \frac{\rho_0^d}{\pi}\sum_{j=1}^{M} w_j J_{-j}(x,0)\mu_j , \; i = 1, \ldots, M ,$$ (E-18a)

$$J_{-i}(x,L) = 2\pi\varepsilon_L I_b T_{wL}(x) + \frac{\rho_L^d}{\pi} \sum_{j=1}^{M} w_j J_{+j}(x,L)\mu_j \quad , \quad i = 1, \ldots, M \quad . \quad (E\text{-}18b)$$

Here, too, the subscript λ was omitted from the variables J, ε, I_b, and ρ for clarity. The divergence of the radiative flux in the medium is expressed by the quadrature as

$$\frac{\partial q_r(x,y)}{\partial y} \quad \int_\lambda \sigma_{a\lambda} \left[4\pi I_{b\lambda} T(x,y) - \sum_{\substack{j=-M \\ j\neq 0}}^{M} w_j J_{j\lambda}(x,y)\mu_j \right] d\lambda \quad , \quad (E\text{-}19)$$

and the radiative flux at the $y = L$ boundary as

$$q_r(x,L) = \int_\lambda \left\{ -\pi\varepsilon_{L\lambda} I_{b\lambda} T_{wL}(x) + \left[1 - \frac{\rho_{L\lambda}^d}{2\pi} \right] \sum_{j=1}^{M} w_j J_{j\lambda}(x,L)\mu_j \right\} d\lambda \quad . \quad (E\text{-}20)$$

The energy equation is solved by the method of finite differences. The divergence of the radiative flux is treated as a volumetric heating source. After incorporating the boundary conditions, the corresponding equations take the following form (see also Figure E-2 for further clarification):

$$\left[\rho C_\rho u(y_j) + \frac{\Delta x}{\Delta y^2} k \right] T(x_{i+1}, y_j) - \frac{\Delta x}{\Delta y^2} k \left[T(x_{i+1}, y_{j+1}) + T(x_{i+1}, y_{j-1}) \right]$$

$$= \rho C_\rho u(y_j) T(x_i, y_j) - \Delta x \frac{\partial q_r(x_{i+1}, y_j)}{\partial y} \qquad 0 < y_j < L \quad , \qquad (E\text{-}21a)$$

$$\left[\frac{1}{2} \rho C_\rho u(y_0) + \frac{\Delta x}{\Delta y^2} k + \frac{\Delta x}{\Delta y} h \right] T(x_{i+1}, y_0) - \frac{\Delta x}{\Delta y^2} k T(x_{i+1}, y_1)$$

$$= \frac{1}{2} \rho C_\rho u(y_0) T(x_i, y_0) + \frac{\Delta x}{\Delta y} h T_\infty - \frac{\Delta x}{2} \frac{\partial q_r(x_{i+1}, y_0)}{\partial y} \qquad y_0 = 0 \quad , \quad (E\text{-}21b)$$

$$\frac{-k}{\Delta y} \left[T(x_{i+1}, y_L) - T(x_{i+1}, y_{L-1}) \right] + q_r(x_{i+1}, y_L) = 0 \qquad y_L = L \quad . \qquad (E\text{-}21c)$$

The expressions for the divergence of the radiative flux and the radiative flux at the boundaries are obtained from Eqs. E-19 and E-20. Equation E-21a,b,c can be used to compute the temperature field by marching forward in the x-direction. Because the radiative flux and its divergence at x_{i+1} are not known before the temperatures at this x-location are computed, Eq. E-21 cannot be directly used. Approximate forms of the Eq. 5.21a,b,c are then used, which are presented as

$$\left[\rho C_\rho u(y_j) + \frac{\Delta x}{\Delta y^2} k \right] T(x_{i+1}, y_j) - \frac{\Delta x}{\Delta y^2} k \left[T(x_{i+1}, y_{j+1}) + T(x_{i+1}, y_{j-1}) \right]$$

$$= \rho C_\rho u(y_j) T(x_i, y_j) - \Delta x \frac{\partial q_r(x_i, y_j)}{\partial y} \qquad 0 < y_j < L \quad , \qquad (E\text{-}22a)$$

$$\rho C_p u(y_j) T(x_i, y_j) \Delta y$$

$$-k \frac{[T(x_{i+1}, y_j) - T(x_{i+1}, y_{j-1})]}{\Delta y} \Delta x \qquad -k \frac{[T(x_{i+1}, y_{j+1}) - T(x_{i+1}, y_j)]}{\Delta y} \Delta x$$

$$\Delta y$$

$$\Delta x \quad (x_{i+1}, y_j)$$

$$\frac{\partial q_r(x_{i+1}, y_j)}{\partial y} \Delta x \Delta y \qquad \rho C_p u(y_j) T(x_{i+1}, y_j) \Delta y$$

$$\rho C_p u(y_0) T(x_i, y_0) \frac{\Delta y}{2}$$

$$h[T_\infty - T(x_{i+1}, y_0)] \Delta x \quad \Delta x \qquad -k \frac{[T(x_{i+1}, y_1) - T(x_{i+1}, y_0)]}{\Delta y} \Delta x$$

$$\frac{\Delta y}{2}$$

$$(x_{i+1}, y_0)$$

$$\frac{\partial q_r(x_{i+1}, y_0)}{\partial y} \Delta x \frac{\Delta y}{2} \qquad \rho C_p u(y_0) T(x_{i+1}, y_0) \frac{\Delta y}{2}$$

$$-k \frac{[T(x_{i+1}, y_L) - T(x_{x+1}, y_{L-1})]}{\Delta y} \Delta x \qquad \Delta x$$
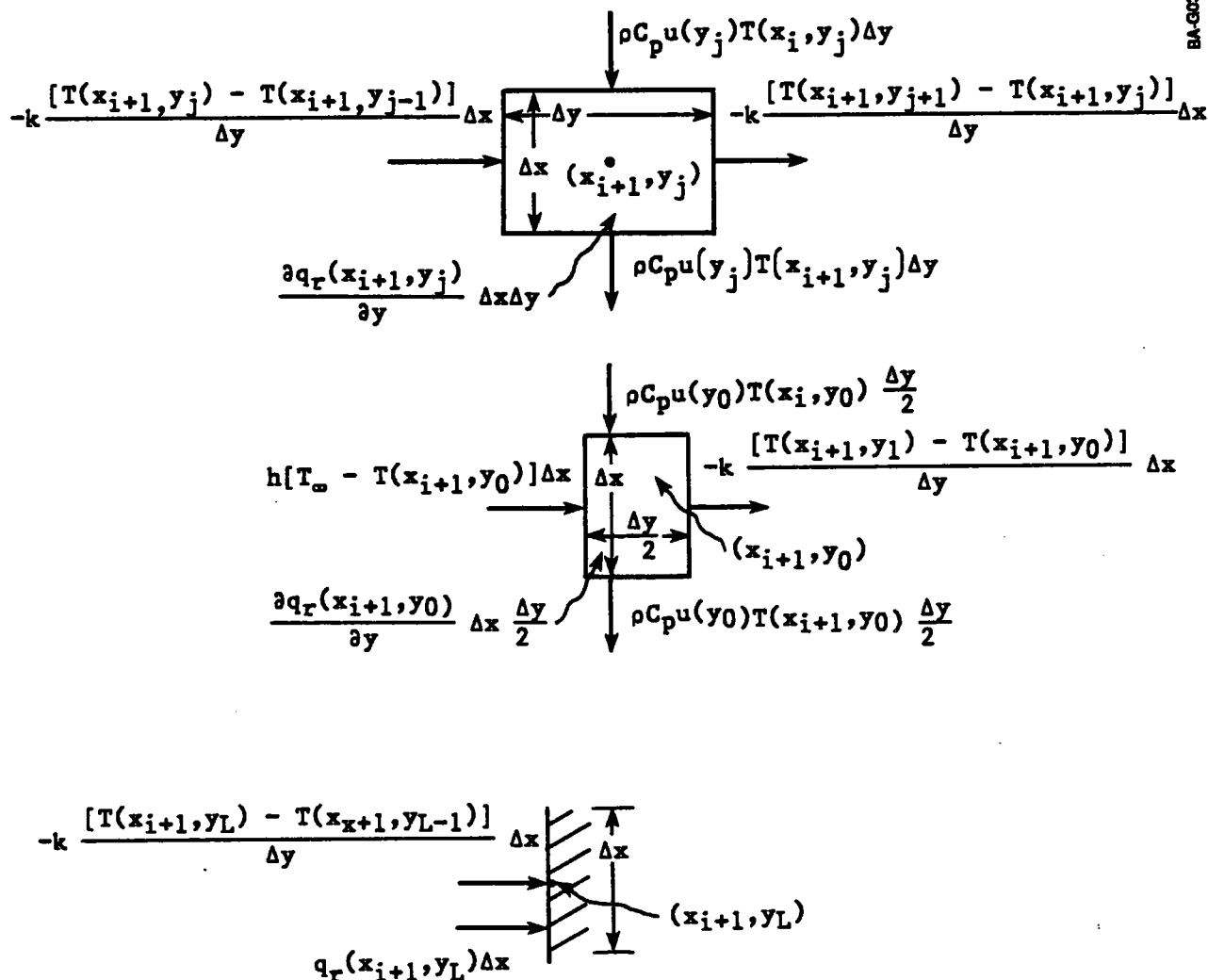
$$(x_{i+1}, y_L)$$

$$q_r(x_{i+1}, y_L) \Delta x$$

Figure E-2. Equations corresponding to the energy equation

$$\left[\frac{1}{2} \rho C_\rho u(y_0) + \frac{\Delta x}{\Delta y^2} k + \frac{\Delta x}{\Delta y} h\right] T(x_{i+1}, y_0) - \frac{\Delta x}{\Delta y^2} k T(x_{i+1}, y_1)$$

$$= \frac{1}{2} \rho C_\rho u(y_0) T(x_i, y_0) + \frac{\Delta x}{\Delta y} h T_\infty - \frac{\Delta x}{2} \frac{\partial q_r(x_i, y_0)}{\partial y} \qquad y_0 = 0 \ ,$$

$$\text{(E-22b)}$$

$$\frac{-k}{\Delta y} \left[T(x_{i+1}, y_L) - T(x_{i+1}, y_{L-1})\right] = -q_r(x_i, y_L) \qquad y_L = L \ . \qquad \text{(E-22c)}$$

These form a tridiagonal linear algebraic system of equations. Equations E-21 and E-22 can be used together in an iterative scheme, such as that outlined in Section E.4.

E.4 The Solution Algorithm

The solution algorithm is summarized in Figure E-3 where flow diagrams are presented. The radiative transfer coefficients σ_a, σ_e, and σ_s and the coefficients of the scattering phase function ζ are obtained from the Mie theory via Eqs. E-4 and E-9 (Dave 1968). The $2M^{th}$-order system of ordinary differential equations specified by selecting a Gaussian quadrature for Eqs. E-17 and E-18 are solved by using the subroutine DVCPR of the commercially available IMSL* software library. Equations E-21 and E-22, used for evaluating the temperatures at subsequent x-locations, are solved using the linear equation solver subroutine LEQT1B in the same software library.
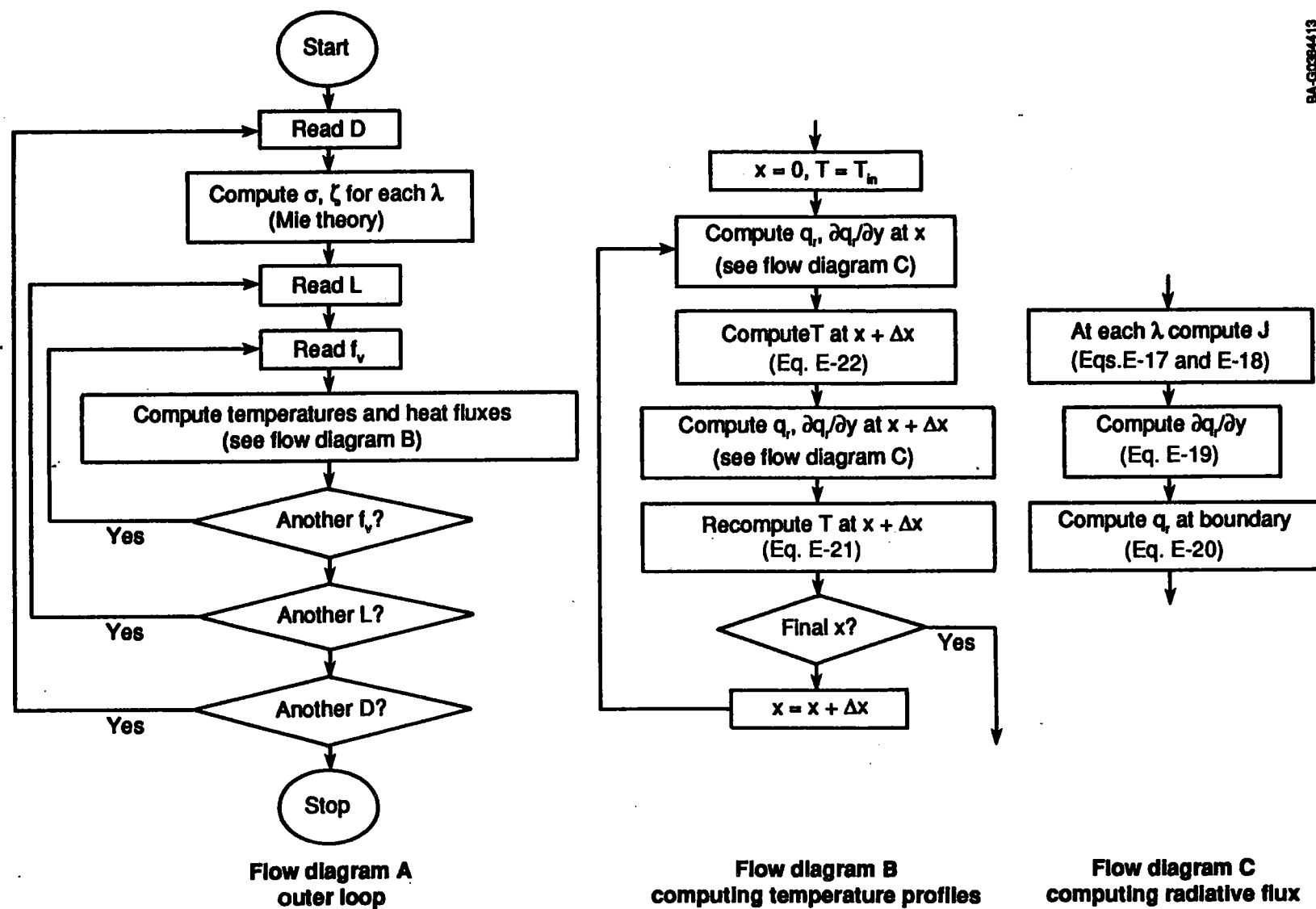
Figure E-3. The solution algorithm

E.5 References

Bohren, C. F., and D. R. Huffman, 1983, <u>Absorption and Scattering of Light by Small Particles</u>, New York: John Wiley & Sons, pp. 83-180.

Dave, J. V., 1968, <u>Subroutines for Computing the Parameters of the Electromagnetic Radiation Scattered by a Sphere</u>, Report 320-3237, Palo Alto, CA: IBM Scientific Center.

Kerker, M., 1961, <u>The Scattering of Light and Other Electromagnetic Radiation</u>, New York: Academic Press.

Kumar, S., and J. D. Felske, 1986, "Radiative Transport in a Planar Medium Exposed to Azimuthally Unsymmetric Incident Radiation," <u>Journal of Quantitative Spectroscopy and Radiative Transfer</u>, Vol. 35, pp. 187-212.

Kumar, S., A. Majumdar, and C. L. Tien, 1988, "The Differential-Discrete-Ordinate Method for Solving the General Equation of Radiative Transfer," presented at the 25th National Heat Transfer Conference, Houston, TX, July 24-27.

APPENDIX F

DAR RADIATIVE TRANSFER PROBLEM DEVELOPMENT

F.1 Properties

Film

Nitrate salt with optical constants is given by the following:

$$n_{film} = 1.4740 - 16.1 \times 10^{-5}T, \text{ where T is temperature in } °C, \; k_{film} = 0.$$

Here n and k are the indices of refraction and absorption, respectively.

Particles

Cobalt oxide (Co_3O_4); optical constants are presented in Table F-1.

Metallic supporting surface

Oxidized stainless steel, $\alpha_L = \varepsilon_L = 0.9 \neq f(\lambda) \neq f(T)$, where α and ε denote the absorptivity and surface emissivity of the metal.

F.2 Operating Conditions

Incoming radiation

Solar spectrum radiation, isotropic within a cone whose axis of symmetry forms a 40-deg angle with the normal to the film and has a 37-deg half angle. The flux on a plane perpendicular to the cone axis is 1380 kW/m^2.

Table F-1. Cobalt Oxide Complex Refractive Index (4)

$\lambda(\mu m)$	n	k
1.2	2.6	0.15
1.15	2.7	0.15
1.1	2.75	0.2
1.05	2.85	0.15
1.0	2.9	0.1
0.95	3.0	0.2
0.9	3.1	0.35
0.85	3.2	0.4
0.8	3.2	0.73
0.75	3.0	0.93
0.725	2.9	0.9
0.7	2.8	0.8
0.65	2.7	0.7
0.6	2.7	0.8
0.55	2.7	0.9
0.5	2.6	0.97
0.45	2.4	1.02
0.4	2.2	1.05
0.35	2.1	1.05

Film

Parabolic velocity profile is assumed with a thickness Reynolds number $\rho UL/\mu = 4\Gamma/\mu = 5000$.

Other boundary conditions

Metallic substrate is insulated on the side not in contact with the salt film, as specified by Eq. E-16.

$$x = 0, \quad 0 < y < L \qquad T(0,y) = T_{in} \; ,$$

$$y = 0, \quad x > 0 \qquad h(T_\infty - T(x,0)) = -k\partial T(x,y)/\partial y\big|_{y=0} \; ,$$

$$y = L, \quad x > 0 \qquad q_r - k\partial T(x,y)/\partial y\big|_{y=L} = 0 \; . \qquad (F-1)$$

The independence of the surface emissivity from wavelength and temperature simplifies the boundary condition at $y = L$ considerably, yielding

$$q_r(x,L) = -\pi\varepsilon_L I_b T_{wL}^4(x) + \left[1 - \frac{\rho_L^d}{2\pi}\right] \int_\lambda \sum_{j=1}^M w_j J_{j\lambda}(x,L)\mu_j \, d\lambda \; , \qquad (F-2)$$

where $\varepsilon_L = 0.9$, $\rho_L^d = 1 - \alpha_L = 0.1$, and

$$I_b(T) = \int_\lambda I_{b\lambda}(T) \, d\lambda = \frac{n_{film}^2 \sigma T^4}{\pi} \; . \qquad (F-3)$$

The value of σ is 5.6696×10^{-8} W/m^2 K^4. Before computing $f_\lambda(\mu,\phi)$, it is necessary to evaluate the reflectivity from the film surface. Assuming the diffuse reflectivity is approximately equal to the normal reflectivity, we obtain the following relation:

$$\rho_0^d = \frac{(n_{film} - 1)^2 + k_{film}^2}{(n_{film} + 1)^2 + k_{film}^2} \; . \qquad (F-4)$$

Since n_{film} and k_{film} are spectrally independent, Eq. F-4 is also independent of wavelength. The numerical value of ρ_0^d is approximately 0.0367 at all temperatures. This implies that the flux penetrating the film is $(1 - \rho_0^d) \times 1380 = 1329.3$ kW/m^2. The solar radiative flux is incident isotropically in a cone at 37-deg half angle and inclined at 40 deg from the film normal. The intensity outside the film is proportional to $I_{b\lambda}$ for 3 deg $\leq \theta \leq$ 77 deg and $-\phi_c \leq \phi \leq \phi_c$, where $I_{b\lambda}$ is the intensity in vacuum and air (Eq. E-1 without the n term), corresponding to the temperature T_{sun} of the sun $_+$5780K), and (see Figure F-1)

$$\phi_c(\theta) = \cos^{-1}\left[\frac{\cos 37 \text{ deg} - \cos \theta \cos 40 \text{ deg}}{\sin 40 \text{ deg} (1 - \cos^2\theta)^{1/2}}\right] \; . \qquad (F-5)$$
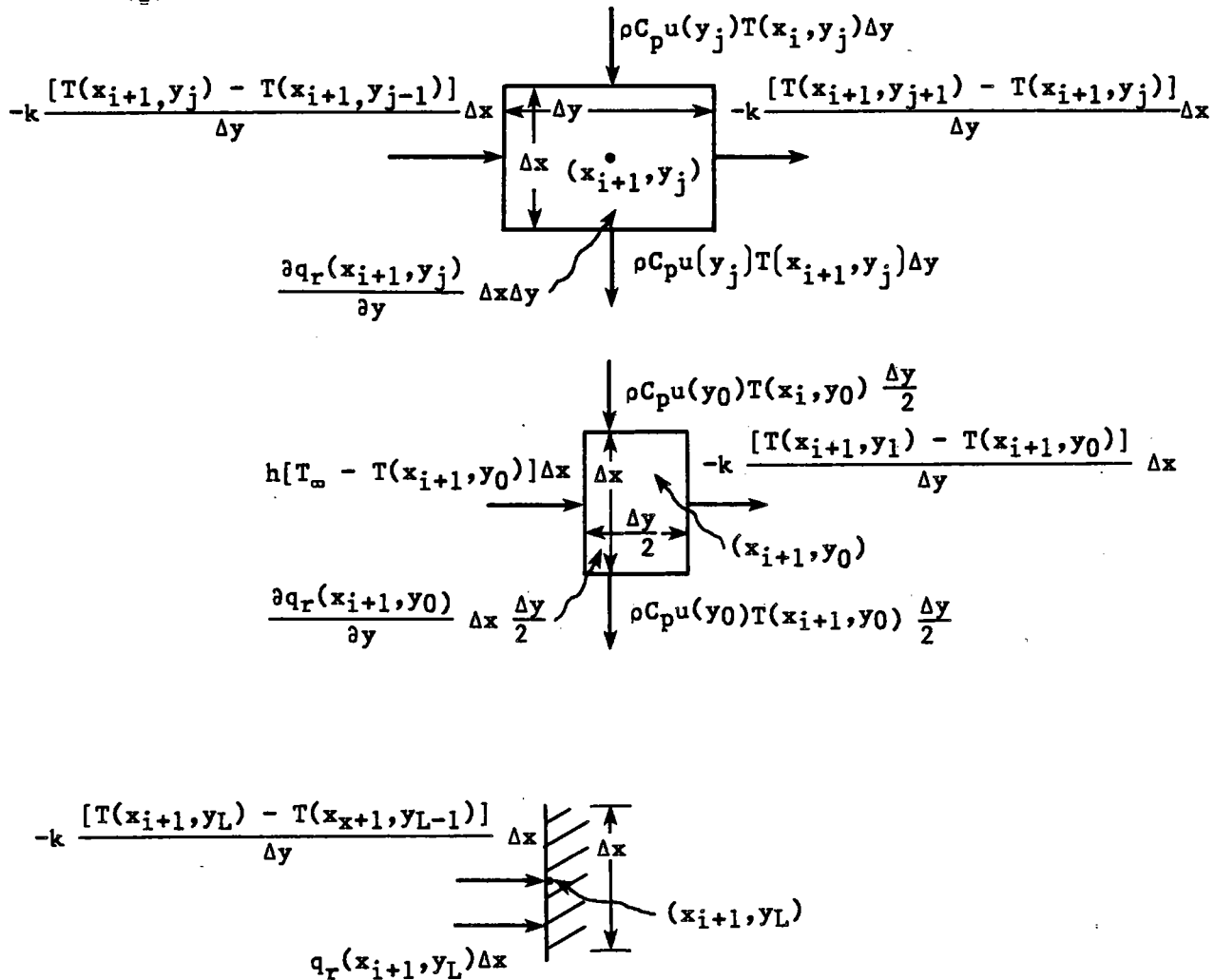
SERI ✺

$$-k \frac{[T(x_{i+1},y_j) - T(x_{i+1},y_{j-1})]}{\Delta y} \Delta x$$

$$\rho C_p u(y_j) T(x_i, y_j) \Delta y$$

$$-k \frac{[T(x_{i+1},y_{j+1}) - T(x_{i+1},y_j)]}{\Delta y} \Delta x$$

$$\Delta y$$

$$\Delta x \quad (\overset{\bullet}{x}_{i+1}, y_j)$$

$$\frac{\partial q_r(x_{i+1},y_j)}{\partial y} \Delta x \Delta y$$

$$\rho C_p u(y_j) T(x_{i+1}, y_j) \Delta y$$

$$\rho C_p u(y_0) T(x_i, y_0) \frac{\Delta y}{2}$$

$$h[T_\infty - T(x_{i+1},y_0)] \Delta x \quad \Delta x$$

$$-k \frac{[T(x_{i+1},y_1) - T(x_{i+1},y_0)]}{\Delta y} \Delta x$$

$$\frac{\Delta y}{2}$$

$$(x_{i+1}, y_0)$$

$$\frac{\partial q_r(x_{i+1},y_0)}{\partial y} \Delta x \frac{\Delta y}{2}$$

$$\rho C_p u(y_0) T(x_{i+1}, y_0) \frac{\Delta y}{2}$$

$$-k \frac{[T(x_{i+1},y_L) - T(x_{x+1},y_{L-1})]}{\Delta y} \Delta x$$

$$\Delta x$$

$$(x_{i+1}, y_L)$$

$$q_r(x_{i+1},y_L) \Delta x$$

Figure F-1. Finite difference equations

With this consideration, the functional form of f_λ in the film, after accounting for the refraction and external reflection effects, is given by

$$f_\lambda(\mu,\phi) = CI_{b\lambda}(T_{sun}) \ , \ 3 \ \text{deg} \leq \theta_0 \leq 77 \ \text{deg} \qquad -\phi_c(\theta_0) \leq \phi \leq +\phi_c(\theta_0) \ ,$$

$$\theta_0 = \sin^{-1} \left[n_{film} \ (1 - \mu^2)^{1/2} \right] \ ,$$

$$C = \frac{\pi}{\sigma T_{sun}^4} \ 1329.3 \times 10^3 \ \frac{1}{1 - \cos^2 37 \ \text{deg}} \ I_{b\lambda}(T_{sun}) \ . \qquad \text{(F-6)}$$

The expressions for $I_{b\lambda}$ are available from Eq. E-2. The polar angle θ_0 outside the film corresponds to $\theta \ (= \cos^{-1} \mu)$ in the film and is linked via the refraction relationship $\sin \theta_0 = n_{film} \sin \theta$. The azimuthal angles ϕ inside and outside the film are the same. The integrated value g_λ is obtained as

$$g_\lambda(\mu) = 2\phi_c(\theta_0) CI_{b\lambda}(T_{sun}) \ . \qquad \text{(F-7)}$$

Document Control Page	1. SERI Report No. SERI/TR-253-3438	2. NTIS Accession No.	3. Recipient's Accession No.

4. Title and Subtitle		5. Publication Date
Direct Absorption Receiver Final Technical Report		December 1989
		6.

7. Author(s)	8. Performing Organization Rept. No.
Mark S. Bohn, Meir Carasso	

9. Performing Organization Name and Address	10. Project/Task/Work Unit No.
Solar Energy Research Institute A Division of Midwest Research Institute 1617 Cole Boulevard Golden, Colorado 80401-3393	ST812331
	11. Contract (C) or Grant (G) No. (C) (G)

12. Sponsoring Organization Name and Address	13. Type of Report & Period Covered
	Technical Report
	14.

15. Supplementary Notes

16. Abstract (Limit: 200 words)

This report describes research on several technical issues associated with the molten-salt direct absorption receiver concept. In particular, we consider the hydrodynamic stability of a long, liquid film, the ejection of droplets from the film, the convective and radiative heat-transfer mechanisms within the film and between the film and the support surface, and the stability of the liquid film with respect to thermocapillary breakdown in the presence of high flux and temperature gradients. The research showed that very small droplets originate from the bursting of turbulent eddies on the liquid surface and larger droplets begin to be ejected where the wave growth begins. The rate of droplet ejection increases exponentially along the flow length. Measuring the convective heat transfer between the nitrate salt film and the support surface showed that very high convective heat-transfer coefficients result, indicating that adding a dopant to darken the salt film may not be needed. These coefficients can be predicted reliably with existing heat-transfer correlations. Using a dimensionless scaling law, we found that the film should not be susceptible to thermocapillary breakdown; however, additional data at high Reynold numbers are needed to verify this.

17. Document Analysis

a. Descriptors   Heat Transfer; Molten Salts; Solar Flux; Central Receivers; Thermal Efficiency; Central Receiver Test Facility

b. Identifiers/Open-Ended Terms

c. UC Categories   235

18. Availability Statement	19. No. of Pages
National Technical Information Service U.S. Department of Commerce 5285 Port Royal Road Springfield, Virginia 22161	125
	20. Price
	A06

Form No. 0069 (3-25-82)